AD______________

Award Number: W81XWH-11-1-0335

TITLE: Investigation of Energy Transfer Dynamics Between Target Contrast Agents and Prostate Cancer Cells Using Ultrafast Spectroscopy

PRINCIPAL INVESTIGATOR: Mr. Yang Pu

CONTRACTING ORGANIZATION: Research Foundation of the City University of New York
New York, NY 10036

REPORT DATE: May 2012

TYPE OF REPORT: Annual Summary

PREPARED FOR: U.S. Army Medical Research and Materiel Command
Fort Detrick, Maryland 21702-5012

DISTRIBUTION STATEMENT: Approved for Public Release;
Distribution Unlimited

REPORT DOCUMENTATION PAGE

Form Approved
OMB No. 0704-0188

1. REPORT DATE *(DD-MM-YYYY)*
01-05-2012

2. REPORT TYPE
Annual Summary

3. DATES COVERED *(From - To)*
15 APR 2011 - 14 APR 2012

4. TITLE AND SUBTITLE
Investigation of Energy Transfer Dynamics
Between Target Contrast Agents and Prostate Cancer Cells Using Ultrafast Spectroscopy

5a. CONTRACT NUMBER

5b. GRANT NUMBER
W81XWH-11-1-0335

5c. PROGRAM ELEMENT NUMBER

6. AUTHOR(S)
Mr. Yang Pu

E-Mail: puyang@sci.ccny.cuny.edu

5d. PROJECT NUMBER

5e. TASK NUMBER

5f. WORK UNIT NUMBER

7. PERFORMING ORGANIZATION NAME(S) AND ADDRESS(ES)
Research Foundation of the City University of New York
New York, NY 10036

8. PERFORMING ORGANIZATION REPORT NUMBER

9. SPONSORING / MONITORING AGENCY NAME(S) AND ADDRESS(ES)
U.S. Army Medical Research and Materiel Command
Fort Detrick, Maryland 21702-5012

10. SPONSOR/MONITOR'S ACRONYM(S)

11. SPONSOR/MONITOR'S REPORT NUMBER(S)

12. DISTRIBUTION / AVAILABILITY STATEMENT Approved for Public Release;
Distribution Unlimited

13. SUPPLEMENTARY NOTES

14. ABSTRACT
Abstract on next page.

15. SUBJECT TERMS

Subject terms on next page.

16. SECURITY CLASSIFICATION OF:			**17. LIMITATION OF ABSTRACT**	**18. NUMBER OF PAGES**	**19a. NAME OF RESPONSIBLE PERSON**
a. REPORT	**b. ABSTRACT**	**c. THIS PAGE**		76	USAMRMC
U	U	U	UU		**19b. TELEPHONE NUMBER** *(include area code)*

Standard Form 298 (Rev. 8-98)
Prescribed by ANSI Std. Z39.18

14. ABSTRACT

Purpose: The objective of this USAMRMC training and researching project is: (1) to train the PI in the optics, biology and biochemistry fields towards a multi-disciplinary prostate cancer researcher; and (2) to understand and investigate the receptor target contrast agents and energy transfer from contrast agents to prostate cancer cells using ultrafast time-resolved spectroscopy.

Specific tasks for the report year (04/15/2011 – 04/14/2012): (1) Training on biological knowledge and technique for cell culture and tissue studies in Memorial Sloan-Kettering Cancer Center (Mons.1-6); (2) Training on time-resolved polarization and steady-state spectroscopic measurements for contrast agents using streak camera and the femtosecond Ti:Sapphir laser system (Mons.7-12); and (3) Following the training, applying PI's optical knowledge into the training program to generate researching outcomes (Mons.1-12).

Major accomplishments and findings: (1) PI has been trained on biological knowledge and technique, and applied for IRB approval for prostate cells and tissues measurements; (2) PI has been trained on time-resolved polarization and steady-state spectroscopic measurements for contrast agents using streak camera and a femtosecond Ti:Sapphir laser system to explore time-resolved dynamics of fluorescein dye-labeled polymer chains with different molecular volume; (3) Followed the training program, PI has applied his optical knowledge to the following research: (3a) use a prostate cancer receptor-targeting contrast agent, namely Cytate, to improve the detection depth of the cancerous prostate areas using optical scanning imaging technology study to improve the detection depth of the cancerous areas; (3b) study the fractal dimension parameters, absorption and scattering coefficients for cancerous and normal prostate tissues systematically; and (3c) evaluate the chemotherapeutic effects on malignant cells using their nature fluorescence.

15. SUBJECT TERMS

Prostate cancer, cell culture, steady-state and time-resolved spectroscopy. NIR scanning polarization imaging, independent component analysis, absorption and emission of cancerous and normal prostate tissues, and contrast agents.

Table of Contents

Annual Report
For Army Grant W81XWH-11-1-0335
(CUNY RF 47204-00-01)
Period covered 04/15/11 – 04/14/12

Introduction

The objective of this Army Medical Research and Materiel Command research project (# W81XWH-11-1-0335) is to train the PI in the optics, biology and biochemistry fields towards a multi-disciplinary prostate cancer researcher. The proposed training plan will also establish a prostate cancer research program at City College of New York (CCNY) through close collaboration with Memorial Sloan-Kettering Cancer Center (MSKCC) and Washington University School of Medicine at St Louis (WUSM). The focus of the training component of the project is to familiarize the PI to the biological aspects of cancer research through attending relevant courses, and cancer research practicum through laboratory rotations. The objectives of the research component of the project are to develop optical approaches to (1) validate the potential over-expressed receptors on prostate cancer cells; and (2) study the energy transfer from the QD-based contrast agents to the cancer cells. While the emphasis of the program is on the training component during the first year, significant progress has been made in both training and research during the *first* reporting period (April 15, 2011 – April 14, 2012) covered by this report.

The tasks for the first year (04/15/2011 – 04/14/2012) were: "Task 1, Training of biological knowledge and technique, and apply for IRB approval for prostate cells and tissues measurements (Months 1-6)"; and "Task 2, Training of biochemistry knowledge and techniques (Months 6-12)."

The tasks for the first year were performed successfully and significant progress was achieved as:

1. Accomplishment of the planned training program on biological knowledge and technique through laboratory rotations and attending group meetings and seminars at MSKCC [1];
2. Accomplishment of the planned training program on time-resolved polarization and steady-state spectroscopic techniques through - hands-on laboratory training at Institute for the Ultrafast Spectroscopy and Lasers (IUSL) in CCNY, and development of research on time-resolved polarization spectroscopic model to explore ultrafast dynamics of fluorescein dye-labeled polymer chains with different molecular volume in both experiment and theory [2];
3. Starting of the planned training program on synthesis of receptor-targeting contrast agents through laboratory rotations and hands-on laboratory training at WUSM;
4. Development of research on non- or less- invasive optical near infrared scanning optical imaging approach for prostate cancer detection using receptor-targeting contrast agents [3];
5. Development of research on systematic studies of fractal dimension parameters, and absorption and scattering coefficients for cancerous and normal prostate tissues [4]; and
6. Development of research on spectroscopic approaches to evaluate the chemotherapeutic effects on malignant cells [5].

Report Body

Since this grant is training-concentrated and budget of this training grant is limited, the training program is also jointly supported by other related grants numbered W81XWH-08-1-0717 (for which, Mentor: Professor Alfano is Co-PI) and W81XWH-07-1-0454 (for which, Co-mentor: Prof. J. Koutcher is PI), in training facilities such as equipments, instruments, biological and biochemical materials and supplies (cells, dyes, cultural medium etc.). During the training, the PI, as a trainee, gains the experiences and knowledge in biology, biochemistry and biomedical optics. Furthermore, the PI, as a postdoctoral research fellow, develops programs to achieve researching purposes under the supports of these three grants. The following highlights our major accomplishments during the first year:

(1) Laboratory cell culture training and animal handling training

The activities reported in this section fulfilled Task 1 described in the proposed S.O.W for training program on biological knowledge and technique.

During the first year, the PI (trainee) has attended the following biological research training and small animal training sessions (*Training Task 1*), held by Research Animal Resource Center (RARC) at MSKCC:

- *RARC Orientation* training session (Certificate as attachment 1);

- *RARC Basic Mouse* training session that included handling and restraint; injectable anesthetics and anesthetic monitoring; parenteral administration; and euthanasia (Certificate as attachment 2);

- *RARC Rodent Survival Surgery* training session that involved surgical equipment and instruments, disinfection and sterilization, animal preparation, surgeon preparation, suture materials and wound closure, and post-operative care (Certificate as attachment 3).

The trainee rotated through the following laboratories and received training on cell culture, flow cytometry, fluorescence microscopic imaging techniques, bioluminescence assay application, cells viability monitoring, and other key techniques used in cancer research.

Laboratory PI: *Prof. Jason Koutcher* (role: Co-mentor)

Key person in Laboratory training: *Dr. Ellen Ackerstaff* (role: the trainer), and *Ms. Natalia Kruchevsky* (role: the trainer, Laboratory technician)

Laboratory background: One focused goal of the current research in Prof. Kouthcer's lab is on distinguishing metastatic from non-metastatic clinical breast cancer using non-invasive techniques.

Training Topic: *Cell culture, flow cytometry, fluorescence microscopic imaging techniques, bioluminescence assay application, and cells viability*

- *Cell culture*: The trainee learned the basic cell culture techniques. The trainee had the responsibility to maintain one metastatic prostate cancer cell line: PC3 in training program and some other kinds of cancer cell lines: 4T1 [1], HTB22 and HTB126 [5]. Routine maintenance, such as subculture and cell counting, was performed.

- *Flow cytometry technique, fluorescence microscopic imaging technique, and bioluminescence assay application*: The trainee learned to use bioluminescence assay, flow cytometry technique, and use fluorescence and conventional microscopic imaging techniques to monitor and analyze cell life cycle.

- *Cells viability*: The trainee learned how cell metabolically adapts to the dynamic microenvironmental changes, such as major nutrient supply vs. deprivation (glucose and glutamine) and oxygen availablilty vs. hypoxia [1].

In this research and training program, 4T1 (metastatic cell) and 67NR (non-metastatic cell) cancer cell lines were studied in an NMR-compatible cell perfusion system and investigated their difference in dynamic metabolic response to: (1) oxygen availability vs. hypoxia; and (2) glutamine (Gln) supply vs. Gln deprivation.

In this study, 4T1 and 67NR cells were cultured and studied to determine the response of cell growth to modified cultural media composition (DME, supplemented with 1% P/S and 10% FBS: DME$_{compl}$): (1) DME$_{compl}$ contains 25 nM glucose (Glc) and 6 mM Gln; (2) DME with 2 mM Gln; (3) DME without Gln; and (4) DME with Glc. Cells were incubated for 48 hours in each medium, harvest, and counted (ViaCount Assay, Guava Technologies). Three independent experiments, with duplicate samples per experiment, were performed for each cell line.

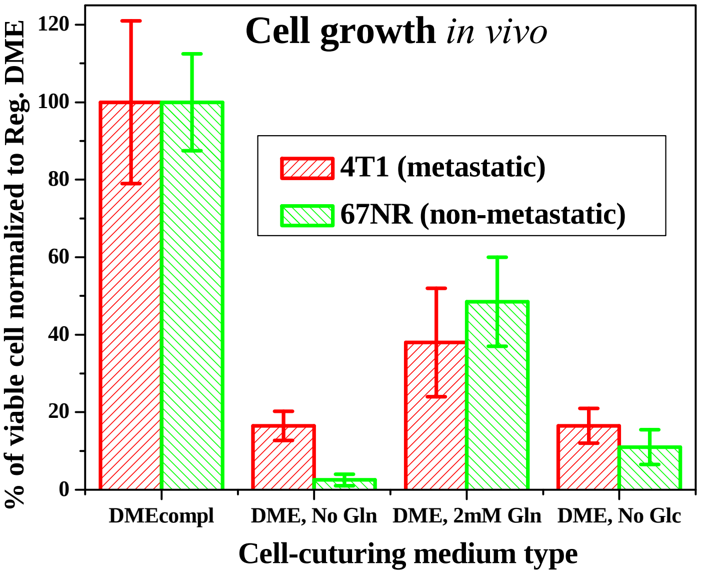

Fig. 1 Cell growth stress condition of 4T1 and 67NR lines

As shown in Fig. 1, the in vitro cell growth is dependent on the availability of both Glc and Gln, in 4T1 and 67NR lines: cell growth drop by 85-89% in the absence of either Gln and Glc, and remains at 35% - 45% when Gln alone is decreased by 2/3; no significant difference were observed in growth between the two cell lines in response to each nutrient deprivation.

Although no significant difference in cell growth were observed in vitro between 4T1 and 67NR cells, when exposed to the defined metabolic stress conditions, each cell line adopts different metabolic strategies to cope with said changes depending on the level of oxygen availability. Mostly, non-metastatic 67NR cells reveal higher glycolytic activity than metastatic 4T1 cells.

(2) Laboratory training of time-resolved polarization spectroscopy of contrast agents

The activities reported in this section fulfilled Task 3 described in the proposed S.O.W for training program on time-resolved polarization and steady-state spectroscopic study of contrast agents.

During the first year, the PI (trainee) has accomplished hands-on laboratory training of the ultrafast spectroscopy and lasers techniques to investigate the rotational motion of fluorescent molecules in solution. In this study, time-resolved fluorescence spectroscopy of Indocyanine Green (ICG) and fluorescein dye-labeled polymer chains with molecular volume ranged from ~410 angstrom^3 to ~5000 angstrom^3 at parallel and perpendicular polarization directions. A theoretical fluorescence depolarization model developed by G. Weber [6] was extended from micro-second to picosecond regimes to investigate and demonstrate the origin of the different decay rate of the two fluorescence components. Experimental tests of this theory were verified by using streak camera optical multi-channel detections for the time-resolved parallel and perpendicular components of the fluorescence emission [2].

We assume dye molecules placed at the center and along the *x*-axis of the co-ordinates excited by light pulse of an arbitrary linear polarization propagating at the *YO* direction at time t_0. G. Weber has pioneered the theory of the fluorescence polarization from an isotropic molecular system due to molecular rotation in nanosecond range [6]. By extending this theory from nanosecond to picoseconds [7], the total, parallel and perpendicular intensity of the fluorescence excited by a linear polarized light is obtained as:

$$I(t) = I_0 \exp(-\frac{t}{\tau_F}) \qquad I_{\|}(t) = \frac{I_0}{3}\exp(-\frac{t}{\tau_F})\left(1 + 2r_0 \exp(-\frac{t}{\tau_{rot}})\right) \qquad I_{\perp}(t) = \frac{I_0}{3}\exp(-\frac{t}{\tau_F})\left(1 - r_0 \exp(-\frac{t}{\tau_{rot}})\right) \tag{1}$$

The average decay time of the polarized components $\langle t\rangle_{\|}$ and $\langle t\rangle_{\perp}$ are:

$$\langle t\rangle_{\perp} = \tau_F \frac{1 - r_0\left[\tau_{rot}/(\tau_{rot} + \tau_F)\right]^2}{1 - r_0\left[\tau_{rot}/(\tau_{rot} + \tau_F)\right]} \qquad \langle t\rangle_{\|} = \tau_F \frac{1 + 2r_0\left[\tau_{rot}/(\tau_{rot} + \tau_F)\right]^2}{1 + 2r_0\left[\tau_{rot}/(\tau_{rot} + \tau_F)\right]} \tag{2}$$

where τ_F is fluorescence lifetime of the molecule, τ_{rot} is rotation time of the molecule, and r_0 is initial fluorescence anisotropy at time t_0. The time dependent fluorescence anisotropy is usually used to describe fluorescence depolarization property using the equation of [8, 9]:

$$r(t) = \frac{I_{\|}(t) - I_{\perp}(t)}{I_{\|}(t) + 2I_{\perp}(t)} = r_0 \exp(-\frac{t}{\tau_{rot}}) \tag{3}$$

where the initial anisotropy indicates the initial orientation distribution of the fluorescent dipoles and is reported to be 0.4 theoretically [6-9] and the rotation time τ_{rot} can be expressed in terms of the diffusion coefficient (D), or the solvent viscosity (η) and the molecular radius (a) by:

$$\tau_{\mathrm{rot}} = (6\mathrm{D})^{-1} = \frac{4\pi\eta \mathrm{a}^3}{3\mathrm{kT}} \tag{4}$$

where k is the Boltzmann constant and T is the absolute temperature [6-9].

In the time-resolved fluorescence experiments for ICG, optical pulses of 130 fs at 800 nm (at 400 nm for fluorescein derivatives measurements) with a repetition rate of 82 MHz from a Coherent Mira 900 Mode-locked Ti:Sapphire laser were used to pump the samples of ICG and fluorescein dye-labeled polymer chains [2, 7]. The temporal profiles of the fluorescence emitted from ICG solution for two polarization directions, parallel and perpendicular to the polarization of the excitation at 800 nm were measured and shown in Fig. 2(a). There is a distinct difference between the decay slopes of the two components, as shown by the dashed and thin-solid line in Fig. 2(a), respectively. In order to see clearly, the peaks of the perpendicular and the parallel components were normalized to the total intensity (which was obtained by using equation $I(t)=I_{\perp}(t)+2I_{\|}(t)$ shown as the thin-dot line in Fig. 2(a)). The thin line in Fig. 2(b) displays the time evolution of polarization anisotropy r(t). The obvious phenomenon is the observation of depolarization as mentioned by the previous researchers [8, 9]. Here we try to explore the understanding in first time based on rotation, initial orientation and lifetime of the excited molecules.

The fluorescence lifetime τ_F is acquired from fitting the total temporal fluorescence intensity data shown in Fig. 2(b) using equation (1). The polarization anisotropy peak value r_0 and the rotation time τ_{rot} of ICG molecule in solution can be obtained by fitting the experimental data of r(t) in Fig. 2 using equation (2).

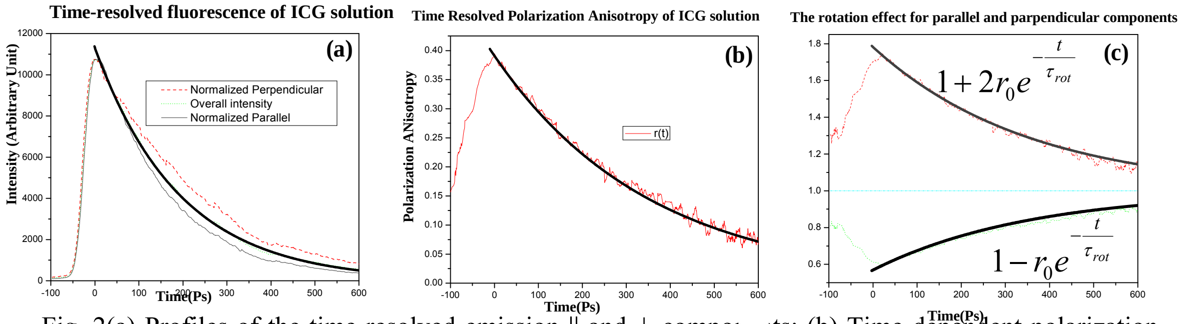

Fig. 2(a) Profiles of the time-resolved emission || and ⊥ components; (b) Time-dependent polarization anisotropy; (c) The schematic temporal contribution of rotation to || and ⊥ component. All experimental data are shown as thin line, but calculation as thick-line.

The dimensions of ICG molecules were estimated as oblate with semi-axes as 13Å and 2Å from bond length and van der Waals radii. The theoretically rotation time of ICG is calculated using equation (4) and these values of $\eta=1.003\times10^{-3}$ Pa·s (viscosity of water), T=293 (20°C - the room temperature), and the Boltzmann constant $k\approx1.380\times10^{-23}$. Using equation (2), the theoretical decay times of $I_\perp(t)$, I(t) and $I_{||}(t)$ can be quantified. The experimental data and calculated results are concluded in Table I.

Table I: Comparison of the experimental and theoretical data of ICG

Type of Data	r_0	τ_{rot}	$\langle t\rangle_{||}$	τ_F	$\langle t\rangle_\perp$
Experimental	0.391±0.0238	353.37±10.55	169.35±4.58	192.46±5.28	239.15±6.48
Theoretical	0.4	351.02	163.79	----	244.91

To illustrate the temporal contribution of the molecular rotation to || and ⊥ components schematically, Fig. 2(c) is generated by using $3I_{||}(t)/I(t)$ and $3I_\perp(t)/I(t)$ with equation (1) showing the influence of the rotational component for the change of $I_\perp(t)$ and $I_{||}(t)$. The trend of the influence of the rotation to $I_\perp(t)$ evidently rises up while that to $I_{||}(t)$ drops. Even $I_\perp(t)$ and $I_{||}(t)$ emitted from same type of molecules with same lifetime, the influence of the molecules' Brownian rotation causes decay of parallel component faster than the total decay and the perpendicular component when the lifetime and the rotation time of the molecule are on same order of magnitude. Our study extends Web's theory to picoseconds range.

The time-resolved fluorescence polarization studies were also performed for fluorescein dye, and the fluorescein dye-labeled dextrans with different Molecular Volume (MV) from 400 to 5,000 angstrom^3. The dimensions of fluorescein were estimated as an oblate ellipsoid with semi-axes of 7 and 2 angstroms, respectively [10]. As an example, Figs. 3 (a) and 3 (b) show the measured temporal profiles of parallel and perpendicular components of the emission from the conjugated dye-polymer with different MV of ~707 and ~3,200 angstrom^3, respectively. The solid line profiles show the parallel component, and the dot lines show the perpendicular one. Fig. 3 (a) and 3 (b) show that $I_{||}(t)$ is greater than $I_{\perp}(t)$ at all of the decay times indicating that this dye-polymer keeps property of the polarization preservation. The time-resolved polarization anisotropy r(t) can be obtained by substituting the data of $I_{||}(t)$ and $I_{\perp}(t)$ shown in Figs. 3 (a) and 3 (b) into the time dependent equation (3). The calculated results are shown in Figs. 3 (c) and 3 (d) displaying the temporal profiles of polarization anisotropy for Fluorescein-polymer with different MV of ~707 and ~3,200 angstrom^3, respectively.

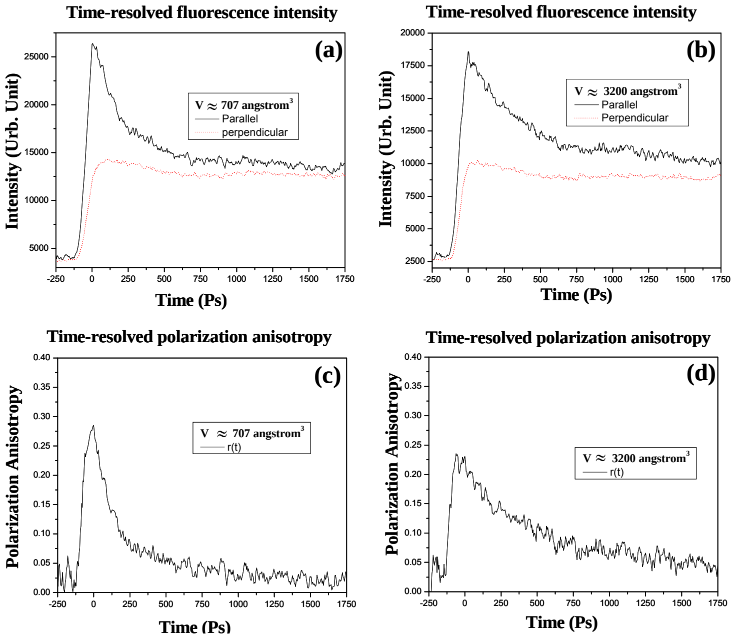

Fig. 3. The time dependent fluorescence intensity profiles of parallel (solid line) and perpendicular (dot line) components of emission from conjugated fluorescein-polymer of MV at (a) ~707 and (b) ~3,200 angstrom^3. The temporal profiles of the polarization anisotropy of conjugated fluorescein-polymer of MV at (c) ~707 and (d) ~3,200 angstrom^3.

The salient features are: (1) the temporal polarization anisotropy shown in Fig. 3(c) exhibits a faster decay than the profile shown in Fig. 3 (d), indicating that a smaller molecular volume gives faster Brownian rotation as described by Equation (4); (2) The initial anisotropy r_0 shown in Fig. 3 (c) is greater than that shown in Fig. 3 (d).

The rotation times can be obtained by fitting the experimental data of r(t) with Equation (3) and the results for a set of Fluorescein-polymer conjugates with attached chain having the volume varying from ~400 to 5,000 angstrom^3 are displayed as solid lines in Fig. 4. The theoretical values of the rotation times with different attached polymer length were calculated using Equation (4) and are shown as the dot-line profile in Fig. 4 in comparison with the experimental values. Since the fluorescein dye appears as approximated oblate symmetric rotors [10], the volume was calculated to be ~ 410 angstrom^3 as an oblate ellipsoid with semi-axes of 7 and 2 angstroms, respectively while no polymer attached.

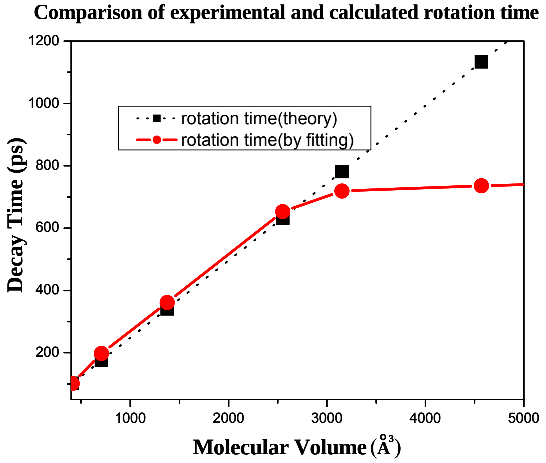

Fig. 4. (a) The rotation time obtained by theoretical calculation (dot line) and by fitting the experimental data (solid line) of the fluorescein dye-polymer conjugate as a function of molecular volume.

The salient features of Fig. 4 are: (1) the rotation times raise with the volume of the attached polymer chain, which are in good agreement with experimental values when the volume of conjugated Fluorescein-polymers is less than 3,200 angstrom^3; (2) The rotation time becomes flat when the volume of the dye-polymer increases beyond ~3,200 angstrom^3. This indicates that for large size molecules, where the volume exceeds a critical value, the rotation time changes very slow with volume of the fluorescent molecules. The incorrect prediction of Equation (2) may be because the Fluorescein-polymer can no longer be estimated as a simple dimension as a sphere or an oblate since it is difficult to control the polymer chain extending direction. The irregular shapes of molecules result in the different rotation rate of D_{ij} [6, 8, 9], and therefore the depolarization will not show simple exponential decay as described by time-resolved polarization anisotropy r(t) in Equation (3). In addition, the rapid internal motions originated by flexible structure of the conjugated fluorescein-polymers cause the “extra” depolarization other than rotation of the molecule [8].

(3) Three dimensional location of cancerous prostate tissue marked with a receptor-targeted contrast agent (Cytate) using near infrared scanning imaging

The activities reported in this section partially fulfilled Task 2 described in the proposed S.O.W for training program on biochemistry knowledge and techniques of receptor-targeted contrast agents.

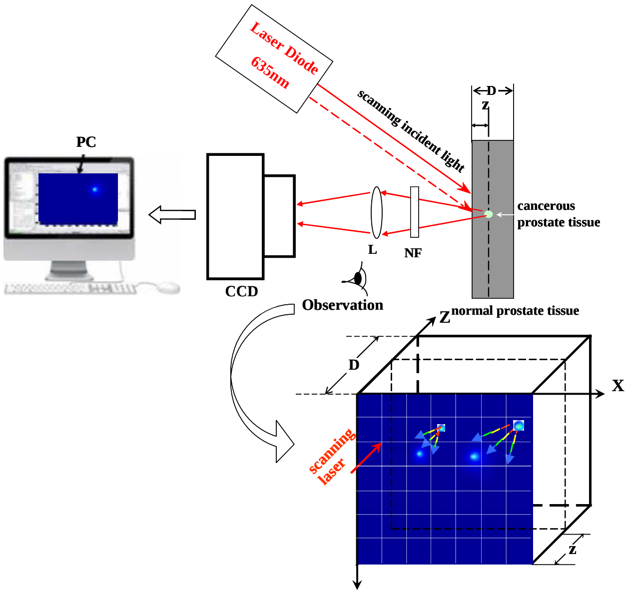

Fig. 5. A schematic diagram of the experimental arrangement used for imaging a pair of Cytate-stained cancerous and normal prostate tissues embedded in large pieces of host normal prostate tissues. L; lense, NF: 830 nm narrow band filter.

Cypate-Octreote Peptide Analogue Conjugate (Cytate), a small ICG-derivative dye-peptide, could be used for effective targeting somatostatin receptor-rich tumor cells in the animal model [11] and over-expressed somatostatin receptors on prostate cells [12] in human prostate tissue [13] studied using optical imaging techniques. To enhance the imaging quality, a fast algorithm, namely OPTICA (optical imaging using independent component analysis), was used to characterize the intensity spatial distribution of Cytate-stained cancerous and normal prostate tissues embedded in un-stained normal prostate tissue [3]. OPTICA extracts the spatial distribution of light "emitted" from each individual target by treating them as independent virtue sources and unmixes them based on their independence. OPTICA hence highlights the difference of the optical properties between different targets embedded inside the turbid medium. OPTICA can be used to determine the existence and 3D-location of inhomogeneities hidden in the homogeneous host medium [3].

Fig. 5 shows a schematic diagram of the experimental setup. The sample is illuminated by a collimated laser diode with λ=635nm in the direction close to the normal to the surface. Two galvanometric mirrors are used to scan the illuminating beam along the x- and y-directions on the front surface of the sample. A narrow band-pass filter at 830 nm was placed in front of a CCD camera to record emission images based on the emission peak of Cytate at ~837nm [13]. When using OPTICA, the leading eigenvalues provide the number and strength of the targets. In the sample preparation, a - pair of small pieces of cancerous and normal prostate tissues were soaked in the same ~3.2 μM concentration Cytate solution for ~15 minutes, and then put into sodium phosphate buffer to wash off the unbound Cytate [13]. Finally, they were covered by a large piece of normal prostate tissue at the depth of ~3.6 mm for scanning imaging.

The OPTICA-generated independent components using data of the scanning fluorescent images of Cytate-stained cancerous and normal prostate tissues embedded in large normal prostate tissue are shown in Figs. 6(a) to 6(f). Figs. 6 (a) and 6 (b) show the first leading IC standing for Cytate-stained cancerous tissue location; 6 (c) and 6 (d) show the second IC indicating Cytate-stained normal tissue location; 6 (e) and 6 (f) show residual - noise. The 3D locations of the Cytate-stained cancerous prostate tissues were obtained by numerical matching the target to the surface of the medium until matching the retrieved IC [3].

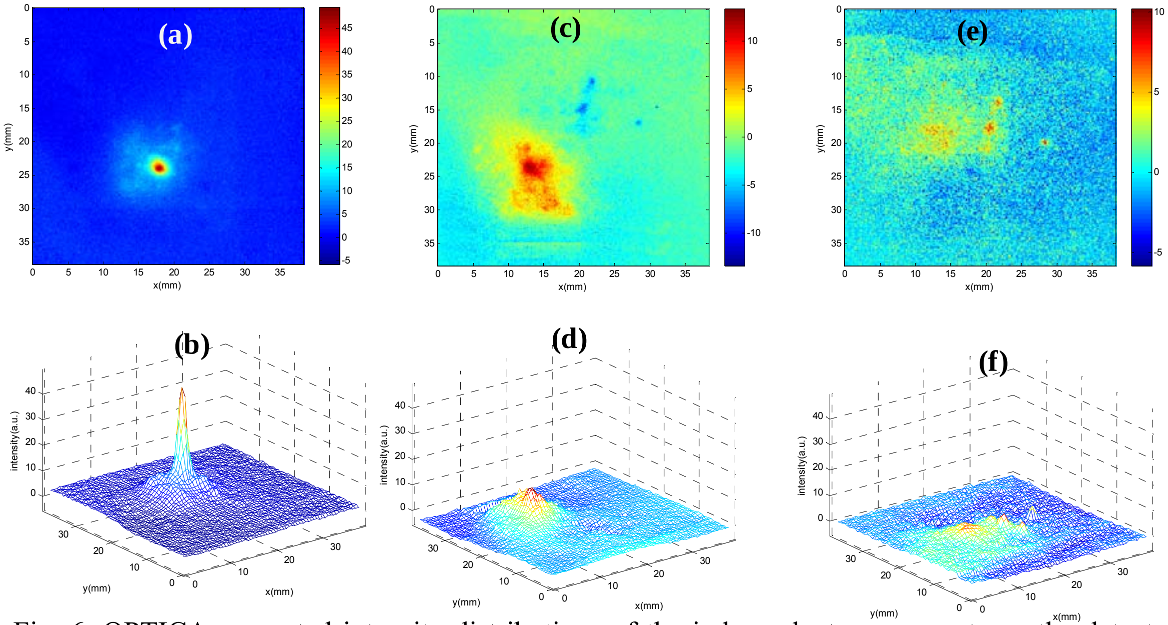

Fig. 6. OPTICA-generated intensity distributions of the independent components on the detector plane for the sample consisting of the Cytate-stained cancerous and normal prostate tissues embedded in un-stained normal prostate tissue. (a) and (b) show the first leading IC indicating for Cytate-stained cancerous prostate tissue; (c) and (d) show the second leading IC standing for Cytate-stained normal prostate tissue; and (e) and (f) show the residual (noise) component.

OPTICA-generated results are summarized in Table II under different conditions using backscattering polarized imaging and OPTICA, which lists the OPTICA-determined positions of the different objects in comparison with their known 3D locations and the contrast enhancement between cancerous and normal tissues.

Table II: Comparison of the known and OPTICA determined positions of embedded objects and the contrast enhancement between cancerous and normal tissues.

object	**covered tissue**	**known (*x, y, z*) position (mm)**	**OPTICA-generated (*x, y, z*) position (mm)**	**I_c/I_n**
stained cancerous tissue	**normal prostate**	**(17.8, 14.6, 2.5)**	**(17.9, 14.4, 2.3)**	**~ 3.9**
stained cancerous tissue	**normal prostate**	**(18, 24, 3.5)**	**(17.6, 23.8, 3.6)**	**~ 2.3**

(4) Systematic studies of fractal dimension parameters, and absorption and scattering coefficients for cancerous and normal prostate tissues

A systematic investigation of the absorption coefficient (μ_a), the scattering coefficient (μ_s), the reduced scattering coefficient (μ_s'), and the anisotropy factor (g) of tissue is necessary for accurate modeling of light transport in tissues. The differences in the values of μ_a, μ_s, μ_s' and g between normal and cancerous tissues may provide a basis for biomedical imaging and potential diagnostics using optical techniques [4]. In this study, we studied μ_a, μ_s, μ_s' and g of cancerous and normal prostate tissues in the 750 – 860 nm spectral range using extinction measurements on thin samples and diffuse reflection measurements on thick samples. Light extinction by a thin specimen (thickness ⟨⟨ mean scattering length, l_s) within the spectral range investigated here is dominated by light scattering. Light transport through a thick tissue slice is usually modeled as a diffusion process, and diffuse reflectance measurements provide information for assessment of μ_a, and $\mu_s' = \mu_s(1-g)$, where g is the anisotropy factor [4].

Since μ_a ⟨⟨ μ_s in the 750 - 860 nm spectral range for prostate tissue, the extinction coefficient, $\mu_t = \mu_s + \mu_a \simeq \mu_s$, and the optical density (O.D.) spectrum of a thin prostate tissue sample is dominated by scattering. The scattering coefficient (μ_s) is given by:

$$\mu_s \cong \mu_t = 2.303\frac{O.D.}{L} \tag{5}$$

where L is the light path length in the tissue.

The backscattered diffuse intensity at position (x, y, 0) on the surface of the thick sample modeled by diffusion approximation is given by [14]:

$$I(x,y) = \frac{l_t\cos\beta}{4\pi\rho_1^3}(1+\mu_{eff}\rho_1)\exp(-\mu_{eff}\rho_1) + \frac{l_t\cos\beta + 2z_e}{4\pi\rho_2^3}(1+\mu_{eff}\rho_2)\exp(-\mu_{eff}\rho_2) \tag{6}$$

where $\rho_1 = \sqrt{(x-l_t\sin\beta)^2 + y^2 + l_t^2\cos^2\beta}$, $\rho_2 = \sqrt{(x-l_t\sin\beta)^2 + y^2 + (2z_e + l_t\cos\beta)^2}$ and $\mu_{eff} = \sqrt{3\mu_a/l_t}$; $l_t = (\mu_s')^{-1}$ is the transport mean free path; z_e is the extrapolation length that depends on the mismatch of the index of refraction at the interface [15]. The extrapolation length is computed to be z_e=1.69l_t. Equation (6) is used to fit the measured diffuse reflectance along a line in the x direction on the tissue surface to obtain μ_a and l_t, which is $1/\mu_s'$. The anisotropy factor g is then obtained using $g = 1-(\mu_s'/\mu_s)$.

As many biological tissues have fractal-like organization and are statistically self-similar, various tissue light scattering models based on fractal geometry have been proposed. The distribution of the number density of particles of diameter d_i is given by [16, 17]:

$$n(d_i) = \frac{\eta_0 d_i^{3-D_f}}{\pi d_i^3/6} = \frac{6\eta_0}{\pi} d_i^{-D_f} \tag{7}$$

where D_f is the fractal volume dimension, η_0 is a scale-dependent constant, and $n(d_i)\Delta d$ gives the number density of the particles with diameters between d_i and $d_i+\Delta d$. The value of η_0 can be determined from the total volume fraction of all particles, T_v, using equations $T_v = \eta_0 \int_{d_{min}}^{d_{max}} d_i^{3-D_f} dd_i \Rightarrow \eta_0 = T_v / \int_{d_{min}}^{d_{max}} d_i^{3-D_f} dd_i$ [16], where d_{min} and d_{max}, are diameters of the smallest and largest scattering particles, respectively.

In such a fractal soft tissue model, the correlation function $R(r)$ of the random fluctuation of the refractive index is a weighted average of fluctuations over a range of correlation length l, that depends on the fractal dimension D_f and the cutoff length or the maximum correlation length, d_{max} [17]. Light scattering property of the tissue is fully determined by the power spectrum (the Fourier transform) of $R(r)$. This model has been shown to be in good agreement with NIR light scattering experimental results in biological tissues and cell suspensions [17].

The amplitude scattering function $S(\theta)$ at the scattering angle θ is given [17]:

$$|S(\theta)|^2 = \int_{kd_{\min}}^{kd_{\max}} \frac{\varepsilon^2 \eta_0 k^{Df-1} x^{6-D_f}}{2\pi[1+2(1-\cos\theta)x^2]^2} dx \tag{8}$$

where $\varepsilon^2=4n_0^4\delta m^2$, $k\equiv 2\pi n_0/\lambda$, n_0 is the index of refraction of the surrounding medium, and δm is the amplitude of the relative refractive index fluctuation. The anisotropy factor (g), the mean cosine of the scattering angle, was then found as [17]:

$$g = \int d\Omega \frac{(1+\cos^2\theta)\cos\theta |S(\theta)|^2}{2k^2} \Bigg/ \int d\Omega \frac{(1+\cos^2\theta)|S(\theta)|^2}{2k^2} \tag{9}$$

where Ω is the solid angle and $d\Omega=2\pi\sin\theta d\theta$ for a scattering angle θ [17]. The reduced scattering coefficient in the fractal soft tissue model follows a power law:

$$\mu_s' \propto \lambda^{3-D_f} \tag{10}$$

This provides a simple procedure to estimate the fractal dimension D_f from the wavelength dependence of μ_s' [17].

Using equations (8) and (9), and the known value of d_{min}, the variation of g as a function of d_{max} can be plotted in a $g \sim d_{max}$ curve. Using the $g \sim d_{max}$ curve, the maximum correlation length d_{max} can be obtained from the determined anisotropy factor g.

The wavelength dependence of μ_s, μ_a, μ_s' and g in the 750-860 nm spectral range is shown in Fig. 7(a), Fig. 7(b), Fig. 7(c), and Fig. 7(d), respectively. Over the entire wavelength range the value of μ_s for normal prostate tissue is larger than that for cancerous prostate tissue, indicating that normal tissue scatters light more strongly than cancerous tissue. The gradual decrease in the value of μ_s with wavelength is consistent with Mie theory prediction.

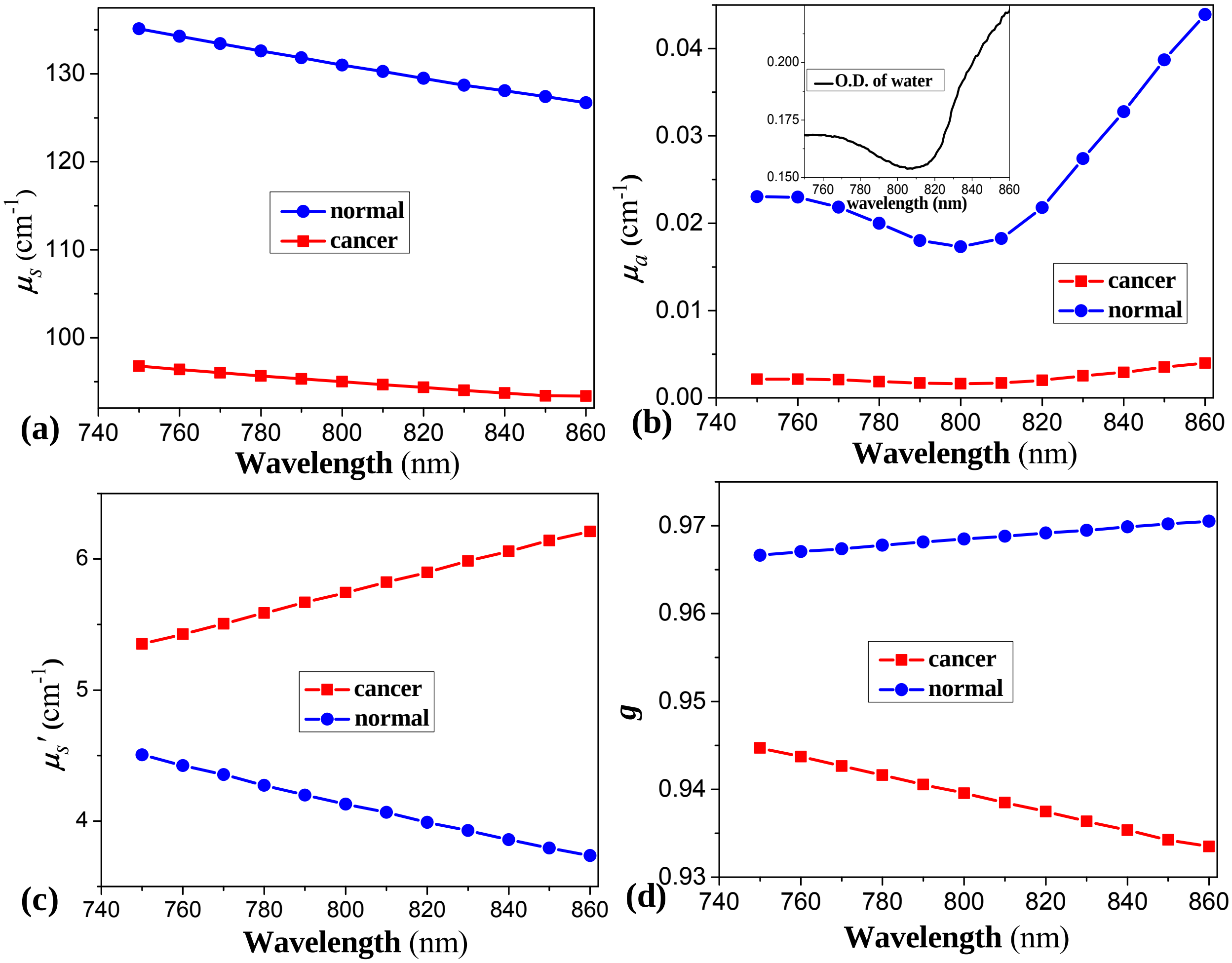

Fig. 7 The wavelength dependence of (a) the scattering coefficient (μ_s) of cancerous (solid square) and normal (solid circle) prostate tissues extracted from the measured optical density (O.D) data in the spectral range of 750 nm to 860 nm using equation (5) in the text; (b) the absorption coefficient (μ_a) of cancerous (solid square) and normal (solid circle) prostate tissues. The absorption spectrum of water with 2 cm thickness in the spectral range of 750nm – 860nm is shown at upper left location as a reference; (c) the reduced scattering coefficients (μ_s') of cancerous (solid square) and normal (solid circle) prostate tissues; and (d) the scattering anisotropy factor g of cancerous (solid square) and normal (solid circle) prostate tissues in the spectral range of 750nm - 860nm.

Fig. 7(b) shows that the absorption coefficient of normal prostate tissue is higher than that of the cancerous tissue in the 750 – 860 nm spectral range. Comparison with the absorption spectrum of water in the inset shows that the absorption spectra of the tissues follow that of water closely, and the behavior is more prominent for the absorption spectrum of the normal tissue. This result indicates that water is the dominant absorptive tissue constituent in this spectral range.

Reduced scattering coefficient (Fig. 7(c)) of normal prostate tissue decreases and that of cancerous prostate tissue increases monotonically in the 750-860 nm range, while the behavior is reversed for anisotropy factor *g*. The overall magnitude of μ_s' is significantly higher for cancerous prostate tissue than for normal prostate tissue. The observed lower values of *g* for cancerous tissue than that for normal tissue (Fig 7 (d)) follow readily from the behavior of μ_s' because of the simple algebraic relation between the two parameters.

To study how the absorption and scattering spectra reflect micro-structural properties of cancerous and normal prostate tissues, we analyzed the scattering data of these two types of tissues using the fractal soft tissue model [17]. The following parameters were used in our simulation: the total volume fraction of all scatterers T_V= 0.2 [16], the diameter of smallest particle d_{min} = 50 nm [16], the index of refraction of the cytoplasm of prostate tissue (host medium) n_0 = 1.35 [18], and the index of refraction of prostate cellular nuclei (scattering particles) n_1 = 1.46 [16, 18].

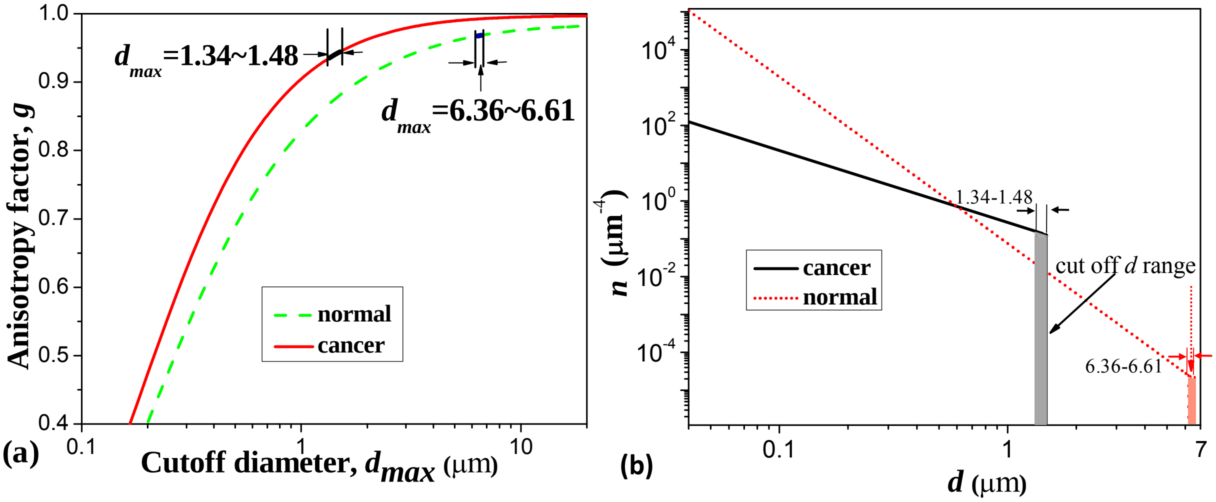

Fig. 8 (a) The anisotropy factor *g* of the cancerous and normal prostate tissues as a function of cutoff diameter d_{max} at 800 nm, and (b) distribution of the number density of scatterers with different diameters, evaluated by fractal tissue model using equation (3). The curves representing the behavior of cancerous and normal prostate tissues are displayed by solid and dash lines, respectively. The cancerous prostate tissue (solid line) has lower weight of smaller particles and higher weight of larger particles than the normal prostate tissue (dash line).

The values of fractal dimension, D_f , were obtained by fitting the data shown in Fig. 7 (c) using Equation (10), and the results show that D_f=1.9±0.04 and 4.4±0.06 for the cancerous and normal prostate tissues, respectively.

The *g* values of the cancerous and normal prostate tissues at 800 nm as a function of cutoff diameter d_{max} were obtained using equations (8) and (9), and the results are displayed as solid and dash lines, respectively, in Fig. 8 (a). Using the previously determined values of *g* shown in Fig. 7(d), the cutoff diameters of the cancerous and normal prostate tissues were found to be 1.42 ± 0.06 μm for the cancerous tissue, and 6.48 ± 0.08 μm for the normal tissue.

The distribution of the number density as a function of the diameter d of scattering particles (scatterers) in cancerous and normal prostate tissues was then calculated using Equation (7), and the results are shown as Fig. 8(b). The salient feature of Fig. 8(b) is that the normal tissue has much more of smaller scatterers than the cancerous tissue in the d ⟨ ~0.6 μm range while the cancerous tissue has much more of larger scatterers than the normal tissue in the d ⟩ ~0.6 μm range.

The fractal parameters for the normal and cancerous prostate tissues are summarized in Table III.

Table III: D_f and d_{max} for cancerous and normal prostate tissues

Tissue type	D_f	d_{max} (μm)	nucleolar diameter	nuclei diameter
Cancer	1.9±0.04	1.42 ± 0.06	1.38 - 1.96 μm [19]	8.4 - 10.31 μm [19]
Normal	4.4±0.06	6.48 ± 0.08	1.10 - 1.24 μm [19]	6.3 - 6.72 μm [19]

As described above, the fractal soft tissue model was used to extract the values of fractal dimension (D_f) from the wavelength dependence of μ_s' and were found to be 1.9 and 4.4 for the cancerous and normal prostate tissues, respectively. The values are markedly different. Similar remarkable difference was observed in the values for cutoff diameter, d_{max}: 1.42 ± 0.06 μm for the cancerous tissue, and 6.48 ± 0.08 μm for the normal tissue. Since the cutoff diameter may be considered to be an upper limit on the size of scatterers in tissue specimens this result may be quite significant. Further probing revealed that the observed value of the cutoff diameter of the cancerous tissue (1.42 ± 0.06 μm) falls within the range of (1.38 - 1.96 μm) for the nucleolar diameter of cancerous prostate cell [19], and the cutoff diameter for normal tissue (6.48 ± 0.08 μm) closely matches the nuclear diameter of normal prostate cell (6.3 - 6.72 μm) [19]. These close agreements point to the intriguing implication that in normal prostate cell the largest scatterers are the nuclei, while in cancerous prostate cells nucleoli are the largest scatterers. -

(5) Chemotherapeutic effects on malignant cells evaluated by native fluorescence spectra

The activities reported in this section are related to Task 1 of the proposed training program on biological knowledge and technique.

The aim of this present research is to determine if the native fluorescence spectroscopy is effective enough to detect changes of tissue compositions (fluorophores) related to the treatment of chemotherapy for malignant cell lines using Nonnegative Matrix Factorization (NMF) analysis.

The human breast cells were purchased from American Type of Culture Collection (ATCC), Rockville, MD. The cell lines used in the study were: malignant human breast cell lines: ATCC HTB22 (Adenocarinoma Pleural Effusion) and ATCC HTB126 (Dutal Carcinoma). The cells were cultured with 90% modified Dulbeco's minimal essential medium (Eagle) (GIBO) and 10% of the fetal bovine serum (GIBCO) in a humidified atmosphere of 4% CO_2 at 37^oC. Half of the cells were treated with ~10^{-6} M retinoic acid (RA) and the remainder served as controls while the cell lines are cultured. The measured cell concentration was estimated as ~105 - 110 × 10^6 cells/ml [5].

The fluorescence emission spectra of cells were measured. The excitation wavelengths of 300nm and 340 nm were selected based on our previous spectral study of the main fluorophores in breast cells [20]. Combined with NMF, the native fluorescence measurements were used to distinguish the RA-treated breast cancer cells from the untreated cell. The main advantage of NMF is that the NMF-recovered spectral data and concentrations of constituents are positive values. This makes the calculated results represent more physically and/or biologically meaning because the spectra and contents of the fluorophores should have non-negative values.

Fourteen pairs of the RA-treated and untreated breast cancer cell samples were investigated using fluorescence spectroscopy with excitation wavelength of 300 nm. The average fluorescence spectral profiles with standard deviation error bars at key wavelengths for the RA-untreated and treated cancerous breast cells are shown in Figs. 9(a) and 9(b), respectively. Each spectral profile was normalized to unit value of 1 (i.e., the sum of squares of the elements in each emission spectra data was set as 1) before taking average and calculation.

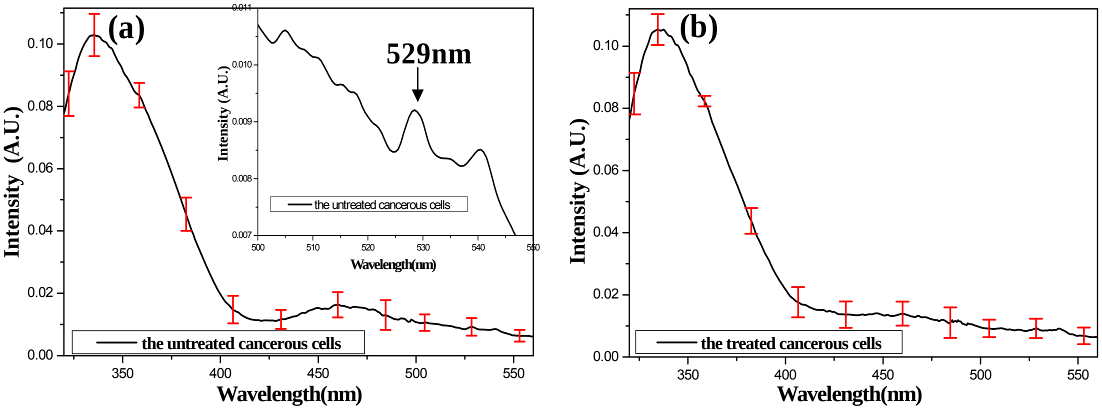

Fig. 9 Average fluorescence spectra of (a) untreated and (b) Retinoic Acid (RA)-treated cancerous breast cells obtained with the excitation of 300 nm.

The main emission peaks of both untreated and treated cancerous breast cells were found at 337nm. The major difference of the fluorescence profiles between the untreated and treated cells is that there exists a much lower local peak at ~ 460nm for the untreated cells while no such a peak for the treated cells. A tiny local peak at 529 nm may be observed in the emission of the untreated cells, which can be more clearly seen by enlarging the fluorescence profile at the spectral range of 700 nm to 900 nm as shown in insert of Fig. 9 (a).

To investigate the relative content changes of Principal Components (PCs) and compare with their corresponding fluorophores, NMF was used to extract spectra of PCs (fluorophores) of the 1st component (tryptophan), the 2nd (NADH) and the 3rd (flavin) for the cells, which are shown as dash, dot and dash-dot lines in Fig. 10(a), respectively. The measured spectra of individual tryptophan, NADH and flavin in solutions are plotted as thicker, thick and thin solid lines, respectively, as references. The two groups of spectra (the extracted and the measured) for each fluorophore show reasonable agreement, which demonstrates that NMF model accounts for the major spectroscopic feature observed, and indicates that the measurements are reasonable.

To investigate the relative content changes of PCs, the contents of tryptophan, NADH and flavin in two types of cells were extracted from the measured total fluorescence spectra using the NMF analysis. Fig. 10 (b) shows the relative content of the 1st PC (tryptophan) vs. the 2nd PC (NADH); 10 (c) displays the 3rd PC (flavin) vs. the 1st PC (tryptophan) and 10 (d) exhibits the 3rd PC (flavin) vs. the 2nd PC (NADH) of the untreated (solid circles) and treated (solid squares) cancerous breast cells. The most salient feature of Fig. 10 (b) is that all data points for the untreated cells are located on the upper side over the data points for the treated cells, indicating that the relative contribution of tryptophan is higher in the untreated cancerous cells in comparison with the treated. Fig. 10 (c) shows again that the relative fluorescence contribution of tryptophan is higher in the untreated cancerous cells in comparison with the treated. Fig. 10 (d) shows that most data points for the untreated cells are located in the up-right side in comparison with the data points for the treated cells, indicating that the relative contents of NADH and flavin are higher in the untreated cancerous cells in comparison with the treated.

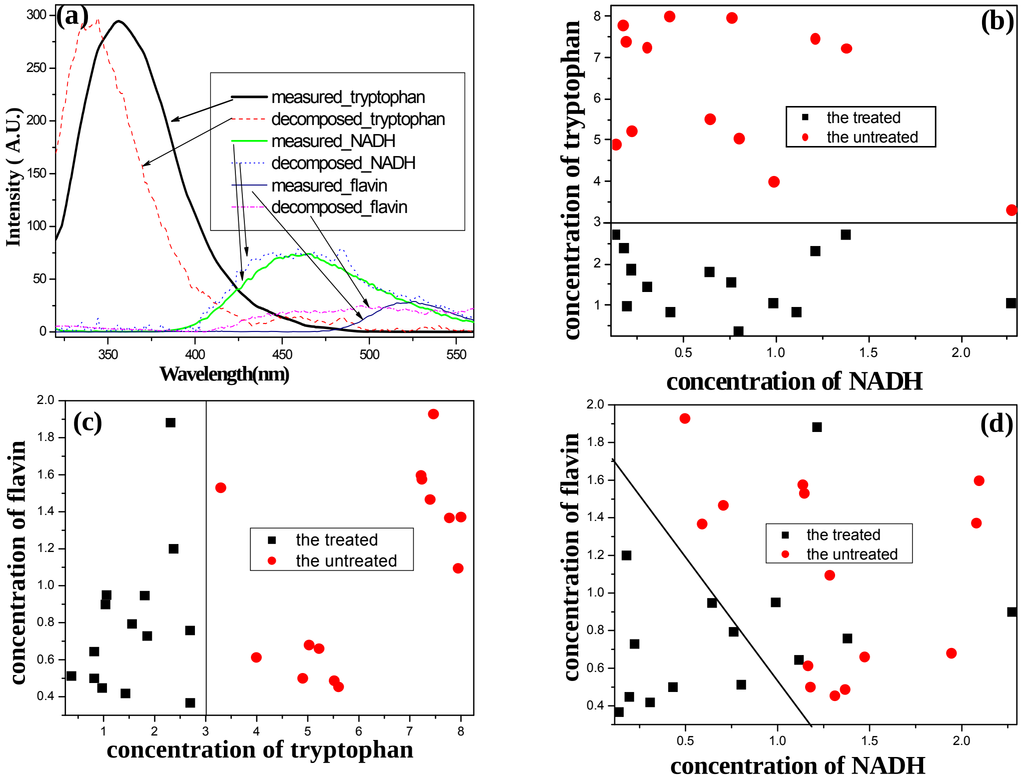

Fig. 10 (a) Comparison of the extracted spectra of the three PCs: the 1st PC – tryptophan (dash line), 2nd PC – NADH (dot line) and 3rd PC – flavin (dash-dot line) for the untreated and treated breast cancerous cells, and the measured spectra of individual tryptophan (thicker line), NADH (thick line) and flavin (thin line) in solution; (b) Fractional content of the 1st PC - tryptophan vs. that of the 2nd PC - NADH; (c) Fractional content of the 3rd PC - flavin vs. that of the 1st PC - tryptophan; (d) Fractional content of the 3rd PC - flavin vs. that of the 2nd PC - NADH by analyzing emission spectra obtained with the excitation of - 300 nm using NMF method. The data for the untreated and treated cells are displayed with the solid circles and solid squares in 10 (b) – 10 (d), respectively.

The following biomedical studies may help to understand these changes. Brown *et al* studied chemotherapy effects for breast cancer [21]. After chemotherapy, the decreased plasma amounts of tryptophan in plasma were observed [21] since increased tryptophan levels are somehow related to increased tumor cell proliferation [21]. NADH is one of the most important coenzyme for the production of Adenosine-Tri-Phosphate (ATP) [22]. The results of decrease of NADH in the RA-treated cancerous cells may reflect a reduction in the production of ATP in these treated cells. Since the decrease of tryptophan and NADH somehow reflect the less activity of cells [21, 22], it can be hypothesized that the RA-treatment results in cancerous cell death or reduction of the activity of cancer cells.

Emission spectra of nine pairs of the RA-treated and untreated breast cancer cell samples were measured with an alternate excitation of 340 nm. The average fluorescence spectral profiles of the untreated (solid line) and treated (dash line) cells are displayed in Figs. 11(a), which shows that the emission profiles of the untreated and treated cells were mainly contributed from NADH corresponding to a peak at ~ 459nm, and flavin corresponding to a peak of ~ 530nm. The major difference of the profiles between the untreated and treated cells is that the shoulder peak at ~ 530 nm for the treated cells is little stronger than that for the untreated cells. Fig. 11 (b) displays the relative content of the flavin vs. NADH of the untreated (solid circle) and treated (solid square) cancerous breast cells analyzed using the NMF analysis. The obvious feature of Fig. 11(b) is that the relative contribution of NADH is higher in the untreated cancerous cells in comparison with the treated, which also reflects the decrease of the relative content of NADH in the treated cancerous breast cells in comparison with the untreated cells.

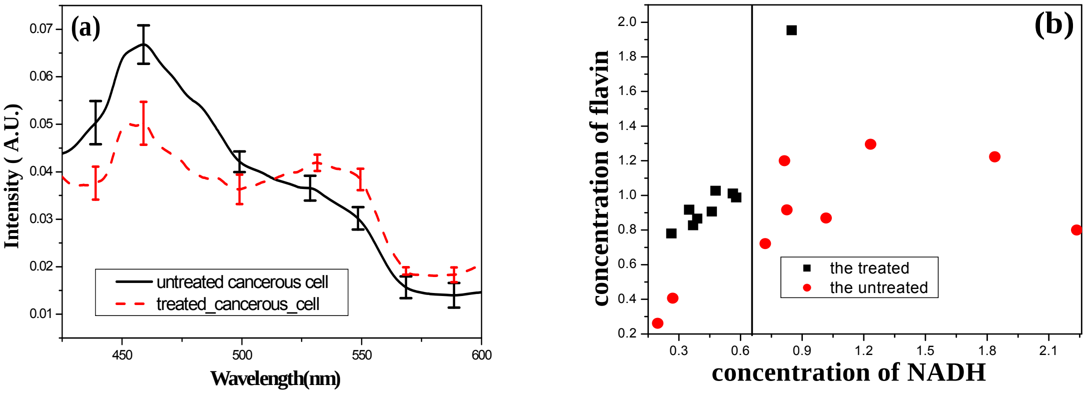

Fig. 11 (a) Average fluorescence spectra of the untreated (solid) and RA-treated (dash) cancerous breast cells obtained with the excitation wavelength of 340 nm.(b) Relative content of the NADH vs. flavin, obtained from the measured fluorescence spectroscopy of the breast cells with 340 nm excitation using the NMF analysis.

This study shows detection of the chemotherapeutic effects on malignant breast cells by measuring the nature fluorescence spectra of cells and extracting the fluorescence spectral features of principal components using an NMF method. The presence and contents of the detectable fluorophores in breast malignant cells such as tryptophan, NADH and flavin were analyzed as the Principal Components for the NMF. We demonstrated that fluorescence intensities of tryptophan, NADH and flavin decreased in the RA-treated cells in comparison with those in the untreated cells. This work shows the change of relative contents of tryptophan, NADH and flavin studied using native fluorescence spectroscopy with the NMF analysis may present potential criteria for evaluation of chemotherapeutic effects on malignant breast cells.

(6) Specific personnel supported by this grant:

Dr. Yang Pu, PI, postdoctoral fellow

Key Accomplishments

- The training program on biological knowledge and technique has been accomplished through laboratory rotations and attending group meetings and seminars at MSKCC, including small animal training sessions (*RARC Orientation*, *RARC Basic Mouse*, *RARC Rodent Survival Surgery*), training on cell culture, flow cytometry, fluorescence microscopic imaging techniques, bioluminescence assay application, cells viability monitoring, and other key techniques used in cancer research.
- The training program on time-resolved polarization and steady-state spectroscopic techniques has been accomplished through hands-on training at the mentor's laboratory in the Institute for the Ultrafast Spectroscopy and Lasers (IUSL) of CCNY. Time-resolved polarization and steady-state spectroscopic measurements of dye-polymer conjugate, target contrast agents in solution and in scattering medium have been performed.
- The time-resolve fluorescence depolarization caused by the Brownian rotation of the dipoles was investigated experimentally and theoretically. For simple and stable molecules, the effect of Brownian rotation is the main cause of the depolarization. We show this effect over a limited range of the molecular volume of Fluorescein dye attached with different polymer chains.
- A receptor target contrast agent, Cytate, was demonstrated as a prostate cancer receptor-targeted contrast agent using NIR scanning imaging technique. The results show the preferential uptake of Cytate by cancerous prostate tissue in comparison with normal prostate tissue. The results also indicate that OPTICA can be used to enhance the contrast of emission intensities between cancerous and normal tissue areas. These techniques (NIR imaging and OPTICA) can also be applied to obtain the three-dimensional locations of targets (Cytate-stained cancerous tissues) in large host normal prostate tissue.
- A systematic study was performed on cancerous and normal prostate tissues to obtain the scattering coefficient (μ_s), the absorption coefficient (μ_a), the reduced scattering coefficient (μ_s'), and the anisotropy factor (g). The values of fractal dimension (D_f) of cancerous and normal prostate tissues were obtained by fitting the wavelength dependence of μ_s'. The cutoff diameter d_{max} as a function of g were investigated using the fractal soft tissue model and Mie theory. Results show that d_{max} of the normal tissue is larger than that of the cancerous tissue. The cutoff diameter d_{max} is observed to agree with the nuclear size for the normal tissue and the nucleolar size for the cancerous tissue.
- The chemotherapeutic effects on malignant cells were evaluated by measuring the native fluorescence spectra of cells and extracting the fluorescence spectral features of principal components using an NMF method. The presence and contents of the detectable fluorophores in breast malignant cells such as tryptophan, NADH and flavin were analyzed as the Principal Components for the NMF. We demonstrated that fluorescence intensities of tryptophan, NADH and flavin decreased in the RA-treated cells in comparison with those in the untreated cells. This work shows the change of relative contents of tryptophan, NADH and flavin studied using native fluorescence spectroscopy with the NMF analysis may

present potential criteria for evaluation of chemotherapeutic effects on malignant breast cells.

Reportable Outcomes

- Three papers in peer-reviewed journals and five papers in conference proceeding resulted from the research supported by and related to this grant have been published in the first year.
- Eight conference and symposium presentations resulted from the research supported by this grant have been made.

The following lists the publications and presentations:

(1) Paper Publications in peer-reviewed journals:

1. Yang Pu, Wubao Wang Mohammad AL-Rubaiee, Swapan Kumar Gayen, and Min Xu, "Determination of optical coefficients and fractal dimensional parameters of cancerous and normal prostate tissues", accepted by *Appl. Spectrosc.*, to be published on July issue 66 (7), (2012).
2. E. Jeyasingh, Yang Pu, W. B. Wang, C. H. Liu, and R. R. Alfano, "Stokes Shift Spectroscopy Pilot Study for Cancerous and Normal Prostate Tissues", accepted by *Appl. Opt.*, to be published on June issue 51 (2012).
3. Y. Pu, W. B. Wang, M. Xu, G. C. Tang, Y. Budansky, M. Sharanov, S. Achilefu, J. A. Eastham and R. R. Alfano, "Near Infrared Photonic Finger Imager for Prostate Cancer Screening", *Technol. Cancer Res. Treat.*, (*TCRT*), 10, **selected as a cover page paper**, 507-517 (2011).

(2) Paper Publications in conference proceedings:

1. Yang Pu, Guichen Tang, Wubao Wang, H. E. Savage, S. P. Schantz, and Robert R. Alfano, "Chemotherapeutic Effects on Breast Malignant Cells Evaluated by Native Fluorescence Spectroscopy", in *Biomedical Optics (BIOMED)/ Digital Holography and Three-Dimensional Imaging (DH)*, JM3A45-1-3 (2012).
2. Y. Pu, W. B. Wang, R. B. Dorshow, R. R. Alfano, "Picosecond polarization spectroscopy of fluorescein attached to different molecular volume polymer influenced by rotational motion" in *Organic Photonic Materials and Devices XIV*, edited by Christopher Tabor, François Kajzar, Toshikuni Kaino, Yasuhiro Koike, Proceedings of SPIE Vol. 8258 (SPIE, Bellingham, WA 2012) 825818.
3. Y. Pu, W. B. Wang, G. C. Tang, Y. Budansky, M. Sharonov, M. Xu, S. Achilefu, J.A. Eastham, R. R. Alfano, "Screening prostate cancer using a portable near infrared scanning imaging unit with an optical fiber-based rectal probe" in *Optical Biopsy X*, edited by Robert R. Alfano, Stavros G. Demos, Proceedings of SPIE Vol. 8220 (SPIE, Bellingham, WA 2012) 822002.
4. Y. Pu, W. B. Wang, M. Alrubaiee, S. K. Gayen, M. Xu, "Systematic studies of fractal dimension parameters, absorption and scattering coefficients for cancerous and normal prostate tissues" in *Photonic Therapeutics and Diagnostics VIII*, edited by Hyun Wook

Kang, Bodo E. Knudsen, Proceedings of SPIE Vol. 8207 (SPIE, Bellingham, WA 2012) 82071H.

5. C.-H. Liu, X. H. Ni, Y. Pu, Y. L. Yang, F. Zhou, R. Zuzolo, W. B. Wang, V. Masilamani, A. Rizwan, R. R. Alfano, "Optical spectroscopic characteristics of lactate and mitochondrion as new biomarkers in cancer diagnosis: understanding Warburg effect" in *Optical Biopsy X*, edited by Robert R. Alfano, Stavros G. Demos, Proceedings of SPIE Vol. 8220 (SPIE, Bellingham, WA 2012) 82200Y.

(3) Presentations and Abstracts:

1. R. V. Simoes, E. Ackerstaff, N. Kruchevsky, Y. Pu, G. Sukenich, and J. Koutcher, "Dynamic metabolic signature of metastatic and non-metastatic breast cancer cells" ISMRM 2012 Annual Meeting, 5638, May 5 -11, (2012).

2. Yang Pu, Guichen Tang, Wubao Wang, H. E. Savage, S. P. Schantz, and Robert R. Alfano, "Chemotherapeutic Effects on Breast Malignant Cells Evaluated by Native Fluorescence Spectroscopy", presented in *Biomedical Optics (BIOMED)/ Digital Holography and Three-Dimensional Imaging (DH) OSA Optics & Photonics Congress*, held in Miami, Florida, on April 29 - May 02, 2012.
3. Y. Pu, W. B. Wang, R. B. Dorshow, R. R. Alfano, "Picosecond polarization spectroscopy of fluorescein attached to different molecular volume polymer influenced by rotational motion" presented at the 2012 OPTO, in SPIE Photonics West 2012, Conference 8258: Organic Photonic Materials and Devices XIV, held in San Francisco, CA, on January 25, 2012. In the Technical Program, PW12O-OE104-3.

4. Y. Pu, W. B. Wang, M. Alrubaiee, S. K. Gayen, M. Xu, "Systematic studies of fractal dimension parameters, absorption and scattering coefficients for cancerous and normal prostate tissues" presented at the 2012 International Biomedical Optics Symposium (BIOS), SPIE Photonics West 2012, Conference BO101: Photonic Therapeutics and Diagnostics VIII, held in San Francisco, CA, on January 21, 2012. In the Technical Program, PW12B-BO101-53.
5. Y. Pu, W. B. Wang, G. C. Tang, Y. Budansky, M. Sharonov, M. Xu, S. Achilefu, J. A. Eastham, R. R. Alfano, "Screening prostate cancer using a portable near infrared scanning imaging unit with an optical fiber-based rectal probe" presented at the 2012 International Biomedical Optics Symposium (BIOS), SPIE Photonics West 2012, Conference BO207: Optical Biopsy X, held in San Francisco, CA, on January 24-25, 2012. In the Technical Program, PW12B-BO207-1.

6. Yang Pu, "Prostate cancer detection using receptor-targeted contrast agents and a near infrared scanning imaging unit with fiber-based rectal probe", presented at "December Career Day", the NYAS/PepsiCo Day in NY December 12, 2011, In the Technical Program, 112.
7. Y. Pu, W. B. Wang, S. Achilefu, M. Xu, and R. R. Alfano, "Detecting prostate cancer in three dimensional position using a receptor-targeted contrast agent and near infrared scanning imaging", presented as the NIH Workshop 2011 7th Inter-Institute Workshop on Optical Diagnostic and Biophotonic Methods from Bench to Bedside, held in Natcher

Conference Center, National Institutes of Health Bethesda, Maryland, ob September, 15-16, 2011, In the Technical Program, NIH 100-68

8. Yang Pu, W. B. Wang, and R. R. Alfano "Detecting Cancerous Prostate Tissues in 3D position after Enhanced by a Receptor-targeted Contrast Agent using Near Infrared Scanning Imaging and Independent Component Analysis" in The City College of New York 2011 Structure Biology Faculty Retreat, held in Concourse Level of The Graduate Center of CUNY, on June 6, 2011.

Conclusions:

1. Successfully accomplished Task 1 of planned training objectives through laboratory rotations and attending group meetings and seminars at MSKCC. The biological and biomedical training include small animal training sessions (*RARC Orientation*, *RARC Basic Mouse*, *RARC Rodent Survival Surgery*), training on cell culture, flow cytometry, fluorescence microscopic imaging techniques, bioluminescence assay application, cells viability monitoring, and other key techniques used in cancer research.
2. Successfully accomplished Task 3 of planned training objectives through hands-on laboratory training at mentor's Lab in the Institute for the Ultrafast Spectroscopy and Lasers (IUSL) of CCNY. The biomedical optics training includes time-resolved polarization and steady-state spectroscopic measurements of dye-polymer conjugate, target contrast agents in solution and in scattering medium, the theory of time-resolve fluorescence depolarization caused by the Brownian rotation of the dipoles.
3. Started Task 2 of planned training objectives through hands-on laboratory training at Washington University School of Medicine at St Louis (WUSM). The biochemistry knowledge and techniques training include cellular and molecular assays, cell labeling, target contrast agent synthesizing. (Because conflicting schedule, Task 3 was arranged to be performed before Task 2. However, task 2 was partially achieved by remote mentoring and Lab-training was started on April 11th, 2012)
4. Following the training program of tasks 1 to 3, the following research programs have been carried out: (1) the time-resolve fluorescence depolarization caused by the Brownian rotation of the dipoles was investigated experimentally and theoretically; (2) a receptor target contrast agent, Cytate, was demonstrated as a prostate cancer receptor-targeted contrast agent using NIR scanning imaging technique, and NIR imaging and an algorithm named OPTICA were applied to obtain the three-dimensional locations of Cytate-stained cancerous tissues in large host normal prostate tissue; (3) a systematic study was performed on cancerous and normal prostate tissues to obtain μ_s, μ_a, μ_s', and g of cancerous and normal prostate tissues. The values of fractal dimension (D_f) and the cutoff diameter d_{max} of cancerous and normal prostate tissues were investigated using the fractal soft tissue model and Mie theory; and (4) the chemotherapeutic effects on malignant cells were evaluated by measuring the native fluorescence spectra of cells and extracting the fluorescence spectral features of principal components using an NMF method. The fluorescence intensities of tryptophan, NADH and flavin were observed to be decreased in the RA-treated cells in comparison with those in the untreated cells.

Plan for the Coming Year

The research tasks for the second year (04/15/2012 – 04/14/2013) are described by Tasks 2, 4, 5 of the Statement of Work. In the coming year, we will:

(1) Continue the PI's training on basic techniques for cellular assay synthesizing in the lab of Professor Alchilefu; study optical properties of different contrast agents to choose derisible spectra for synthesis; and synthesize 2-3 kinds of objective receptor target contrast agents, which will be used to target corresponding over-expressed receptors in prostate cancer cells under direction of Professor Alchilefu.

(2) Submicron resolution microscopic study of targeting contrast agents conjugated with prostate cancer cells using Confocal microscopy; training of operations of Alpha*NSOM* under direction of Professor Alfano; exploiting the specificity and affinity of synthesized contrast agents with prostate cancer cells monitoring using Confocal microscope; Submicron resolution microscopic study of targeting contrast agents conjugated with prostate cancer cells; control experiments with normal prostate cells; develop new method to image submicron resolution of receptor expression on cellular and molecular level.

(3) Time-resolved polarization and steady-state spectroscopic study of targeting contrast agents to prostate cancer cells to investigate the affinity between target contrast agents and prostate cancer cells; research on different kinds of over-expressed receptors of prostate cancer cell lines; time-resolved polarization and steady-state spectroscopic measurements of synthesized targeting contrast agents; time-resolved polarization and steady-state spectroscopic measurements of prostate cancer cells; time-resolved polarization and steady-state spectroscopic measurements of t contrast agents conjugated with prostate cancer cells; study conjugation of targeting contrast agents with prostate cancer cells based on the time-resolved polarization spectroscopic measurements and empirical theory of rotational dynamics and fluorescence polarization anisotropies in scattering medium; and Control experiments with normal prostate cells.

References

1. R. V. Simoes, E. Ackerstaff, N. Kruchevsky, Y. Pu, G. Sukenich, and J. Koutcher, "Dynamic metabolic signature of metastatic and non-metastatic breast cancer cells" ISMRM 2012 Annual Meeting, 5638, May 5 -11, (2012).

2. Y. Pu, W. B. Wang, R. B. Dorshow, R. R. Alfano, "Picosecond polarization spectroscopy of fluorescein attached to different molecular volume polymer influenced by rotational motion" in *Organic Photonic Materials and Devices XIV*, edited by Christopher Tabor, François Kajzar, Toshikuni Kaino, Yasuhiro Koike, Proceedings of SPIE Vol. 8258 (SPIE, Bellingham, WA 2012) 825818.

3. Y. Pu, W. B. Wang, M. Xu, G. C. Tang, Y. Budansky, M. Sharanov, S. Achilefu, J. A. Eastham and R. R. Alfano, "Near Infrared Photonic Finger Imager for Prostate Cancer Screening", *Technol. Cancer Res. Treat.*, (*TCRT*), 10, 507-517 (2011).

4. Yang Pu, Wubao Wang Mohammad AL-Rubaiee, Swapan Kumar Gayen, and Min Xu, "Determination of optical coefficients and fractal dimensional parameters of cancerous and normal prostate tissues", *Applied spectroscopy*, accepted to be published on July issue 66(7), (2012).

5. Yang Pu, G. C. Tang, W. B. Wang, H. E. Savage, S. P. Schantz, and R. R. Alfano, "Native fluorescence spectroscopic evaluation of chemotherapeutic effects on malignant cells using nonnegative matrix factorization analysis", *Technol. Cancer Res. Treat.*, (*TCRT*), 10, Issue 2, 113-120 (2011).
6. R. D. Spencer and G. Weber, "Influence of Brownian rotations and energy transfer upon the measurements of fluorescence lifetime". *J. Chem. Phys*. 52, 1654-1663, (1970).
7. Y. Pu, W. B. Wang, S. Achilefu, and R. R. Alfano, "Time-resolved spectroscopy and near infrared imaging enhanced by receptor-targeted contrast agents for prostate cancer detection", an **invited paper** in the Proceedings of SPIE, Vol. 7895, pp 78950B-1-10 (2011), in the "Optical Biopsy IX", edited by R. R. Alfano and Stavros G. Demos.
8. G. R. Fleming, J. M. Morris and G. W. Robinson, "Direct observation of rotational diffusion by pico-second spectroscopy", *Chemical Physics*, 17, 91-100, (1976).
9. G. Porter, P. J. Sadkowski and C. J. Tredwell, "Pico-second rotational diffusion in kinetic and steady state fluorescence spectroscopy", *Chemical Physics Letter*, 49, 416-420, (1977).
10. Scout Hell, "Size Matters: How big are molecules", http://www.bbc.co.uk/dna/h2g2/A791246
11. J. E. Bugaj, S. Achilefu, R. B. Dorshow and R. Rajagopalan, "Novel Fluorescent contrast agents for optical imaging of *in vivo* tumor based on a receptor-targeted dye-peptide conjugate platform", *Journal of Biomedical Optics,* 6(2), 122-133 (2001).
12. J. Hansson, A. Bjartell, V. Gadaleanu, N. Dizeyi, P. A. Abrahamsson, "Expression of somatostatin receptor subtypes 2 and 4 in human benign prostatic hyperplasia and prostatic cancer", *Prostate*, 53(1), 50-59 (2002).
13. Y. Pu, W. B. Wang, B. B. Das, S. Achilefu, and R. R. Alfano, "Time-resolved fluorescence polarization dynamics and optical imaging of Cytate: a prostate cancer receptor-targeted contrast agent", *Appl. Opt.*, 47, 2281-2289 (2008).
14. M. Xu, M. Alrubaiee, S. K. Gayen and R. R. Alfano, "Determination of light absorption, scattering and anisotropy factor of a highly scattering medium using backscattered circularly polarized light", *Optical interaction with tissue and cells XVIII, Proc. of SPIE*, 6435, J1-6 (2007).
15. J. X. Zhu, D. J. Pine and D. A. Weitz, "Internal reflection of diffusive light in random media", *Phys. Rev. A*, 44, 3948 – 3959 (1991).
16. Ruikang K. Wang, "Modeling optical properties of soft tissue by fractal distribution of scatterers", *J. Mod. Opt.*., 47, 103-120 (2000).
17. M. Xu and R. R. Alfano, "Fractal mechanisms of light scattering in biological tissue and cells", *Opt. Lett*. 30, 3051-3053 (2005).
18. Steven L. Jacques and Scott A. Prahl, "Introduction to tissue optics", http://omlc.ogi.edu/classroom/ece532/index.html
19. R. Montironi, R. Mazzucchelli, A. Santinelli, M. Scarpelli, A. Beltran and D. Bostwick, "Incidentally detected prostate cancer in cystoprostatectomies: pathological and

morphometric comparison with clinically detected cancer in totally embedded specimens", *Hum. Pathol.*, 36, 646– 654 (2005).

20. Y. Pu, W. B. Wang, G. C. Tang and R. R. Alfano, "Changes of collagen and NADH in human cancerous and normal prostate tissues studied using fluorescence spectroscopy with selective excitation wavelength", *J. Biomed. Opt.*, 15, 047008-1-5 (2010);
21. Raymond R. Brown, Caroll M. Lee, Peter C. Kohler, Jaquelyn A. Hank, Barry E. Storer and Paul M. Sondel, "Altered tryptophan and neopterin metabolism in cancer patients treated with Recombinant Interleukin 2", *Cancer Res.*, 49, 4941 - 4944 (1989).
22. George D. Birkmayer, M.D., Ph.D. "The role of NADH in cancer therapy", http://www.iatmo.org/abstract/birkmayer.pdf

Appendix

1. A abstract of presentation entitled "Dynamic metabolic signature of metastatic and non-metastatic breast cancer cells" by R. V. Simoes, E. Ackerstaff, N. Kruchevsky, Y. Pu, G. Sukenich, and J. Koutcher, presented in ISMRM 2012 Annual Meeting, 5638, May 5 -11, (2012).
2. A page proof of a paper entitled "Determination of optical coefficients and fractal dimensional parameters of cancerous and normal prostate tissues", by Yang Pu, Wubao Wang Mohammad AL-Rubaiee, Swapan Kumar Gayen, and Min Xu, accepted by *Appl. Spectrosc.*, to be published on July issue 66(7), (2012).
3. A page proof of a paper entitled "Stokes Shift Spectroscopy Pilot Study for Cancerous and Normal Prostate Tissues", by E. Jeyasingh, Yang Pu, W. B. Wang, C. H. Liu, and R. R. Alfano, accepted by *Appl. Opt.*, (2012).
4. A paper entitled "Near Infrared Photonic Finger Imager for Prostate Cancer Screening", by Y. Pu, W. B. Wang, M. Xu, G. C. Tang, Y. Budansky, M. Sharanov, S. Achilefu, J. A. Eastham and R. R. Alfano, published in *Technol. Cancer Res. Treat.*, (*TCRT*), 10, 507-517 (2011).
5. A paper entitled "Chemotherapeutic Effects on Breast Malignant Cells Evaluated by Native Fluorescence Spectroscopy", by Yang Pu, Guichen Tang, Wubao Wang, H. E. Savage, S. P. Schantz, and Robert R. Alfano, published in *Biomedical Optics (BIOMED)/ Digital Holography and Three-Dimensional Imaging (DH)*, JM3A45-1-3 (2012).
6. A paper entitled "Picosecond polarization spectroscopy of fluorescein attached to different molecular volume polymer influenced by rotational motion" by Y. Pu, W. B. Wang, R. B. Dorshow, R. R. Alfano, published in *Organic Photonic Materials and Devices XIV*, edited by Christopher Tabor, François Kajzar, Toshikuni Kaino, Yasuhiro Koike, Proceedings of SPIE Vol. 8258-18 (SPIE, Bellingham, WA 2012).

Attachment

1. Certificate of *RARC Orientation*;

2.Certificate *of RARC Basic Mouse*;

3. Certificate *of RARC Rodent Survival Surgery*.

Appendix 1

A abstract of presentation entitled “Dynamic metabolic signature of metastatic and nonmetastatic breast cancer cells” by R. V. Simoes, E. Ackerstaff, N. Kruchevsky, Y. Pu, G. Sukenich, and J. Koutcher, presented in ISMRM 2012 Annual Meeting, 5638, May 5 -11, (2012).

5638

DYNAMIC METABOLIC SIGNATURES OF METASTATIC AND NON-METASTATIC BREAST CANCER CELLS

Rui Vasco Simoes[1], Ellen Ackerstaff[1], Natalia Kruchevsky[1], Yang Pu[1,2], George Sukenick[1], and Jason A Koutcher[1]
[1]Memorial Sloan-Kettering Cancer Center, New York, NY, United States, [2]The City College of New York, New York, NY, United States

INTRODUCTION: Distinguishing metastatic from non-metastatic clinical breast cancer, non-invasively, would significantly improve evaluation of patient prognosis. Recent studies with two isogenic murine breast cancer lines, metastatic 4T1 and non-metastatic 67NR, revealed differences at the level of (a) LDH-A expression, in response to changing oxygen tensions *in vitro*, and (b) lactate accumulation, during tumor growth *in vivo* (1). Understanding how each cell line metabolically adapts to dynamic microenvironmental changes, such as oxygen availability vs. hypoxia, and major nutrient supply vs. deprivation (glucose and glutamine (2,3)), could provide unique non-invasive biomarkers of metastatic and non-metastatic breast cancer phenotypes, useful in developing new therapies.

PURPOSE: To study 4T1 and 67NR breast cancer lines in an NMR-compatible cell perfusion system and investigate differences in their dynamic metabolic responses to (a) oxygen availability vs. hypoxia, and (b) glutamine (Gln) supply vs. Gln deprivation.

METHODS: 4T1 and 67NR cells were initially studied *in vitro* to determine the response of cell growth to modified media composition (DME, supplemented with 1% P/S and 10% FBS: DME_{compl}): 1) DME_{compl}, contains 25 mM glucose (Glc) and 6 mM Gln; 2) DME with 2 mM Gln; 3) DME without Gln; 4) DME without Glc. Cells were incubated for 48 h in each medium, harvested, and counted (ViaCount Assay, Guava Technologies). Three independent experiments, with duplicate samples per experiment, were performed for each cell line. Slight modifications were introduced in our cell perfusion system described previously (4) to accommodate its use in a 500 MHz vertical-bore Bruker magnet. For each study, 3.0 x10^6 cells were seeded on microcarriers (Plastic Plus, SoloHill) and cultured for 3 days. Cells were then loaded into the perfusion system: a custom-made 10 mm screw-cap tube where culture medium and gas were circulated and the temperature controlled (37 °C) by a heating water jacket. The MR experiments consisted in repeatedly acquiring ^{13}C, ^{1}H, and ^{31}P spectra (standard Bruker BBO probe) while challenging the perfused cells with different metabolic perturbations. These were carried out in six steps (I – VI, 5 h each): I, DME_{compl} and carbogen gas (95% O_2 / 5% CO_2); II, 100% ^{13}C(1)-Glc labeled medium, without Gln, and carbogen gas; III, same medium as in II but during hypoxia (95% N_2 / 5% CO_2); IV, still hypoxia but replacing the medium with 100% ^{13}C(1)-Glc and 2 mM Gln; V, same medium as in IV but shifting the gas back to carbogen; VI, same as in I. Each experiment was repeated 3 times for each cell line. Spectral analysis of peak areas we carried out with AMARES (jMRUI v4.0). Statistical analyses were carried out with the paired t-Test (SPSS 15.0) to compare 4T1 vs. 67NR data (significance level: $p<0.05$).

RESULTS: As shown in Fig. 1, the *in vitro* cell growth is dependent on the availability of both Glc and Gln, in 4T1 and 67NR lines: cell growth drops by 85-95% in the absence of either Gln or Glc, and remains at 35-45% when Gln alone is decreased by 2/3; no significant differences were observed in growth between the two cell lines in response to each nutrient deprivation. As for dynamic cell perfusion studies, ^{31}P-monitored ATP levels were kept within ±27% of their initial concentration during the experiments (I-VI), in both cell lines, although showing significant differences during stages IV-VI (data not shown). ^{1}H-visible total choline compounds (3.21 ppm) and mobile lipids (1.29 ppm, mixed contribution with lactate) showed consistent stress-response changes at each stage, similar in both cell lines (data not shown). ^{13}C-labeling studies revealed that 67NR cells are significantly more glycolytic than 4T1 cells in the experimental conditions tested: in 67NR cells, the rate of glucose-derived lactate (Lac) production is 2-fold higher than in 4T1 cells. The glycolytic Lac synthesis during hypoxia is Gln-dependent in 4T1 cells (2-fold higher rate in presence of glutamine vs. deprivation), but not in 67NR cells. Supply of Gln vs. deprivation, generates significantly different dynamic responses between 4T1 and 67NR cells, as far as turnover of glycolytic intermediates, e.g. glyceraldehyde-3-phosphate, alanine synthesis, and TCA cycle activity. In aerobic conditions and presence of Gln, 4T1 cells incorporate more Glc into the TCA cycle (3-fold higher rate of glutamate synthesis) than 67NR cells, whereas the latter show higher glycolytic activity, i.e. 2.4-fold higher rate of Lac synthesis, and also 25-fold faster synthesis of alanine.

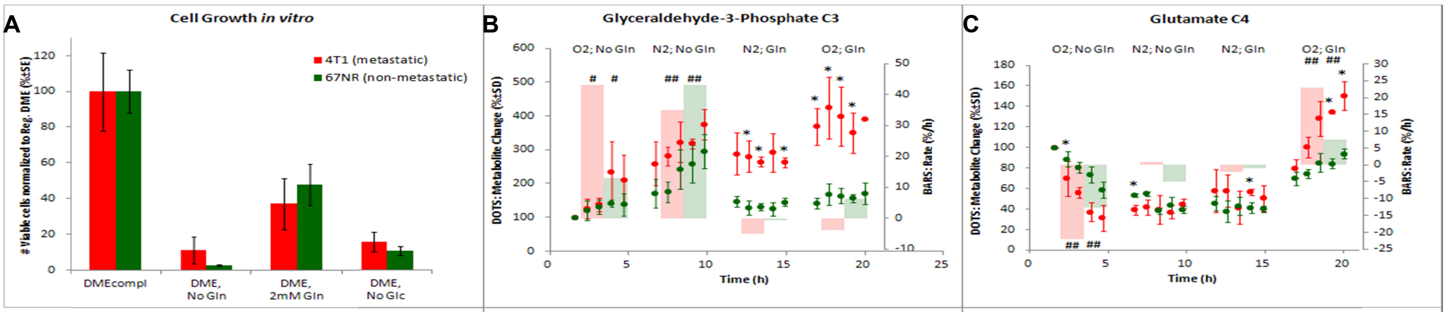

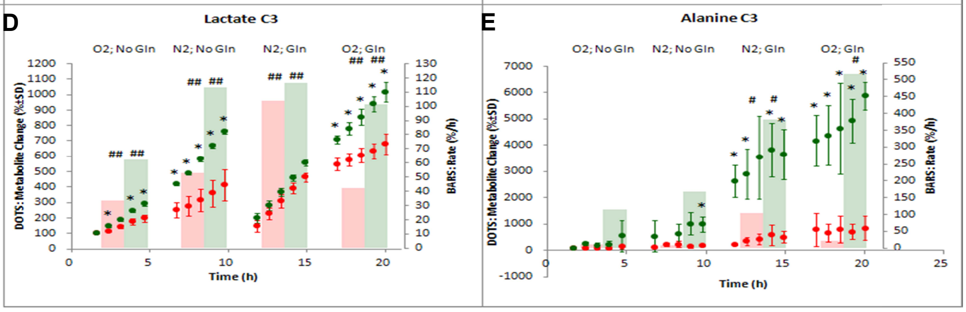

Figure 1 – Cell growth (A) and cell perfusion studies (B-E) of 4T1 (red) and 67NR (green) lines. A, Stress conditions, from left to right: DME_{compl}; Gln deprivation; 2mM Gln; Glc deprivation. B-E, ^{13}C-NMR monitoring: I (0-5h), Gln deprivation; II (5-10h), hypoxia; III (10-15h), 2mM Gln; IV (15-20h), oxygen supply. Chemical Shifts (ppm): glyceraldehyde-3-P C3, 65.98; lactate C3, 21.18; alanine C3, 17.30; glutamate C4, 34.59. Time-points normalized to the initial value of each curve: *, $p<0.05$. Slopes (synthesis/ consumption rates): #, $r^2>0.8$; ##, $r^2>0.9$.

CONCLUSIONS: Although no significant differences in cell growth were observed *in vitro* between 4T1 and 67NR cells, when exposed to defined metabolite stress conditions each cell line adopts different metabolic strategies to cope with said changes, depending on the level of oxygen availability. Mostly, non-metastatic 67NR cells revealed higher glycolytic activity than metastatic 4T1 cells. Unlike in 67NR cells, glycolysis is Gln-dependent in the more aggressive cell line (4T1) during hypoxia, dropping when oxygen becomes available to favor TCA cycle activity. Ongoing ^{13}C(3)-Gln studies should provide further insight into these metabolic differences.

ACKNOWLEDGMENTS: Work supported by NIH grants PO1 CA115675 and NCI P30 CA0874 (Cancer Center Support Grant).

REFERENCES: (1) Serganova *et al.* Clin. Cancer Res. 2011, 17: 6250-6261; (2) Yuneva et al. Cell Cycle 2008, 7: 2083-2089; (3) DeBerardinis et al. PNAS 2007, 104: 19345-19350; (4) Simões et *al.* Proc ISMRM 2011, p330, a3148.

Appendix 2

A page proof of a paper entitled “Determination of optical coefficients and fractal dimensional parameters of cancerous and normal prostate tissues”, by Yang Pu, Wubao Wang Mohammad AL-Rubaiee, Swapan Kumar Gayen, and Min Xu, accepted by *Appl. Spectrosc.*, to be published on July issue 66(7), (2012).

Determination of Optical Coefficients and Fractal Dimensional Parameters of Cancerous and Normal Prostate Tissues

Yang Pu,[a] Wubao Wang,[a] Mohammad AL-Rubaiee,[b] Swapan Kumar Gayen,[b] Min Xu[c]*

[a]Institute for Ultrafast Spectroscopy and Lasers, Department of Physics, The City College of the City University of New York, 160 Convent Avenue, New York, NY 10031 USA
[b]Department of Physics, The City College and the Graduate Center of the City University of New York, 160 Convent Avenue, New York, NY 10031 USA
[c]Department of Physics, Fairfield University, Fairfield, CT 06824 USA

Optical extinction and diffuse reflection spectra of cancerous and normal prostate tissues in the 750 to 860 nm spectral range were measured. Optical extinction measurements using thin *ex vivo* prostate tissue samples were used to determine the scattering coefficient (μ_s), while diffuse reflection measurements using thick prostate tissue samples were used to extract the absorption coefficient (μ_a) and the reduced scattering coefficient (μ_s'). The anisotropy factor (g) was obtained using the extracted values of μ_s and μ_s'. The values of fractal dimension (D_f) of cancerous and normal prostate tissues were obtained by fitting to the wavelength dependence of μ_s'. The number of scattering particles contributing to μ_s as a function of particle size and the cutoff diameter $d_{\max}$ as a function of g were investigated using the fractal soft tissue model and Mie theory. Results show that $d_{\max}$ of the normal tissue is larger than that of the cancerous tissue. The cutoff diameter $d_{\max}$ is observed to agree with the nuclear size for the normal tissues and the nucleolar size for the cancerous tissues. Transmission spectral polarization imaging measurements were performed that could distinguish the cancerous prostate tissue samples from the normal tissue samples based on the differences of their absorption and scattering parameters.

Index Headings: **Prostate tissue; Prostate cancer detection; Biomedical imaging; Absorption coefficient; Scattering coefficient; Reduced scattering coefficient; Anisotropy factor; Near-infrared imaging; NIR spectroscopy; Diffusion; Mie theory; Fractal tissue model; Transmission imaging.**

INTRODUCTION

Prostate cancer is the most common visceral malignancy in American men. Hence, there exists a need for development of affordable, noninvasive modalities for early detection and diagnosis of prostate tumors. Near-infrared (NIR) optical imaging and spectroscopy offer the potential for noninvasive detection and diagnosis based on differences in pathological architecture and optical characteristics between cancerous and normal prostate tissues. The disruption of the normal architecture of tissue that accompanies cancer and its progression may be modeled by fractal geometry.[1] A combination of optical spectroscopic investigations and fractal geometric analysis presents an intriguing possibility for development of a useful modality for prostate cancer detection and diagnosis.

Variations in extracellular[2] and nuclear[3] structures and chromophore compositions cause differences in optical scattering and absorption properties of cancerous and normal prostate tissues, which in turn provide optical contrast, and may serve as native markers for prostate cancer detection. A survey of the literature suggests that the change of water content within living cells might be the primary factor in carcinogenesis.[4–6] Tissues with high water content will usually be hypodense in relation to normal tissue.[5] The dominant chromophore in biological tissue, which absorbs light in the infrared range, is water.[4,5]

A systematic investigation of the absorption coefficient (μ_a), the scattering coefficient (μ_s), the reduced scattering coefficient (μ_s'), and the anisotropy factor (g) of tissue is necessary for accurate modeling of light transport in tissues.[7] The differences in the values of μ_a, μ_s, μ_s', and g between normal and cancerous tissues may provide a basis for biomedical imaging and potential diagnostics using optical techniques.[7,8]

Several authors have suggested fractal analysis as a useful tool in the study of cancer.[9–14] Baish and Jain elucidated the role of fractal geometry in describing the pathological architecture of tumors and its potential for providing insight into tumor growth mechanism.[9] Bizzarri et al. emphasized that the appropriate level of observation for the study of carcinogenesis is tissue and suggested that fractal measures may provide reliable information about the system complexity.[10] The fractal approach was used to model soft tissues and, along with the Mie scattering theory, provided the basis for numerical evaluation of the phase functions, the optical scattering coefficient, the reduced scattering coefficient, the backscattering coefficient, and the anisotropy factor.[11–14] However, there is a paucity of systematic and detailed investigations exploring the correlation between optical properties and fractal characteristics of normal and cancerous tissues involving different types of cancers and cancers in different stages of progression.

Received 13 September 2011; accepted 22 March 2012.
* Author to whom correspondence should be sent. E-mail: mxu@mail.fairfield.edu.
DOI: 10.1366/11-06471

0003-7028/12/6607-000000$2.00/0

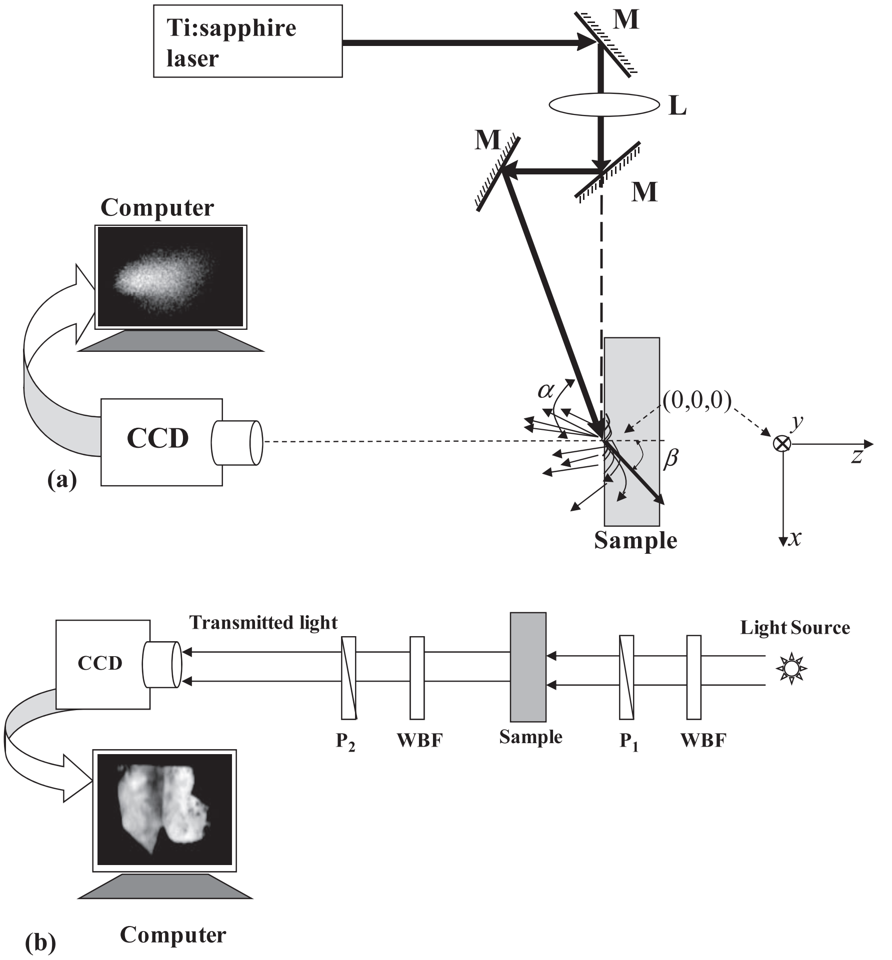

FIG. 1. (**a**) Schematic diagram of the diffuse reflectance imaging experimental setup; (**b**) NIR spectral polarization imaging arrangement (CCD: charge-coupled device, M: mirror; L: lens, P_1: polarizer, P_2: analyzer, and WBF: wide-band filter).

In this paper, we report on the initial results of a study of optical properties and fractal parameters of ex vivo normal and cancerous prostate tissues and how these parameters vary between these two types of tissues. We obtained μ_a, μ_s, μ_s', and g of cancerous and normal prostate tissues in the 750–860 nm spectral range using extinction measurements on thin samples and diffuse reflection measurements on thick samples. Light extinction by a thin specimen (thickness << mean scattering length, l_s) within the spectral range investigated here is dominated by light scattering. Therefore, measurements on thin tissue may approximate μ_s in tissue and present a good starting estimation. Light transport through a thick tissue slice is usually modeled as a diffusion process, and diffuse reflectance measurements provide information for assessment of μ_a, and $\mu_s' = \mu_s(1 - g)$, where g is the anisotropy factor.[7,8,15]

EXPERIMENTAL METHODS AND SAMPLES

Prostate tissue specimens were obtained from the Cooperation Human Tissue Network (CHTN), the National Disease Research Interchange (NDRI), and Hackensack University Medical Center (HUMC) under an Institutional Review Board (IRB) approval at the City College of New York (CCNY). For every cancerous tissue sample, a normal tissue specimen from the same patient was obtained for comparison. CHTN, NDRI, and HUMC provided pathology reports for the samples. The samples were received on dry ice and were neither chemically treated nor frozen before spectroscopic and imaging measurements. The time elapsed between tissue resection and measurements varied from sample to sample due to different sample sources, but all were within 30 hours.

Six pairs of different prostate tissue specimens obtained from six patients of age between 49 and 64 years were investigated. The Gleason scores of the six cancerous tissue specimens varied from 5 to 8 as indicated in the pathology reports. The cancerous samples were carefully checked to determine the hard parts to locate the cancerous regions before making any measurements. Assessment using hardness is acknowledged to be a simple way to locate regions of malignancy.[6]

For extinction spectral measurements, the cancerous and normal prostate tissues were cut to a thickness of ~100 μm and an area of ~2 cm × 3 cm. The tissue samples were then put into 100 μm thick quartz cells and slightly compressed to ensure same thickness for the extinction measurements. The extinction spectra (optical density, O.D., vs. wavelength) of normal and cancerous prostate tissues in the 400 to 2400 nm spectral range were measured using a Perkin-Elmer Lambda-9 UV/VIS/NIR Spectrophotometer.

For diffuse reflectance measurements, the cancerous and normal prostate tissue samples were cut into ~2 cm × 2 cm × 1.1 cm pieces. The schematic diagram of the diffusive reflectance experimental setup is shown in Fig. 1a. A

Ti : sapphire laser (Spectra-Physics Tsunami) beam tunable from 750 to 860 nm was used to illuminate the sample. The laser was operated in continuous-wave (cw) mode and had a spectral full width at half-maximum bandwidth less than 1 nm The beam passed through a 40-cm focal length converging lens and illuminated the sample at an incidence angle of $\alpha = 72.4°$. Backscattered light in the direction normal to the surface of the sample was recorded by a charge-coupled device (CCD) camera. Measurements made in 10 nm steps over the 750 to 860 nm spectral range resulted in 12 sets of backscattering data.

The effective area recorded for the backscattered light intensity distribution used for analyzing is ~2 mm × 5 mm. Light reflectance predominantly probes the volume of the sample around the point of incidence. The effective area recorded for the backscattered light intensity distribution and used for analysis is on the order of ~2 mm × 5 mm. While the light penetrates deep into the tissue, the major contribution to backscattered signal at the detection angle comes mainly from a depth of approximately 1 mm. The incident beam was aimed at the cancer site. In the case of a tumor of size smaller than the probed volume, the fitted optical parameters should be regarded as the average property of the probed volume (including the tumor and its surrounding environment). The cancer sites examined in the diffuse reflectance measurements were of sizes comparable to the effective area mentioned above, and hence the probed optical properties approximate those of the cancerous areas.

A spectral polarization imaging setup used for transmission imaging measurements is schematically shown in Fig. 1b. A white light beam collimated to a diameter of ~2 cm was passed through wide band filters (WBF) with a typical bandwidth of 60 nm centered at 700 nm and 800 nm to select the desirable spectral range for imaging. A polarizer (P_1) was located in the incident beam path before the sample to obtain a linearly polarized incident beam of light. The second polarizer (P_2) was positioned in front of the CCD camera for selecting the detection polarization direction (parallel or perpendicular to the orientation of P_1). A cooled silicon CCD camera (Photometric CH350L), which has spectral response in the 400 to 1000 nm range and is equipped with a 50-mm focal-length zoom lens, was used to record the images in transmission geometry.

THEORETICAL FORMALISM

Determination of μ_a, μ_s, μ_s', g from Optical Spectroscopic Measurements. Since $\mu_a << \mu_s$ in the 750 to 860 nm spectral range for prostate tissue, the extinction coefficient, $\mu_t = \mu_s + \mu_a \simeq \mu_s$, and the optical density (O.D.) spectrum of a thin prostate tissue sample is dominated by scattering. The scattering coefficient (μ_s) is given by:

$$\mu_s \cong \mu_t = 2.303 \frac{O.D.}{L} \tag{1}$$

where L is the light path length in the tissue.

Backscattered light intensities measured in diffuse reflection experiments for a thick prostate tissue sample with thickness of ~1.1 cm were used to extract the optical absorption and the reduced scattering coefficients. The ordinate of (x, y, z) is defined in Fig. 1a. In the case of an obliquely incident pencil beam, the origin of the system co-ordinate is set on the surface ($z = 0$) and the incident direction is ($\sin\alpha$, 0, $-\cos\alpha$), where α is the incidence angle ($\alpha = 72.4°$ in our case). The Snell's law predicted direction of the diffraction beam within the tissue is ($\sin\beta$, 0, $-\cos\beta$), where $\sin\alpha = n \sin\beta$, and n is the index of refraction of prostate tissue ($n = 1.35$).[16] The backscattered diffuse intensity at position (x, y, 0) on the surface of the sample is given by:[15]

$$\begin{aligned} I(x,y) = {} & \frac{l_t \cos\beta}{4\pi\rho_1^3}(1 + \mu_{\text{eff}}\rho_1)\exp(-\mu_{\text{eff}}\rho_1) \\ & + \frac{l_t \cos\beta + 2z_e}{4\pi\rho_2^3}(1 + \mu_{\text{eff}}\rho_2)\exp(-\mu_{\text{eff}}\rho_2) \end{aligned} \tag{2}$$

where

$$\rho_1 = \sqrt{(x - l_t \sin\beta)^2 + y^2 + l_t^2 \cos^2\beta},$$

$$\rho_2 = \sqrt{(x - l_t \sin\beta)^2 + y^2 + (2z_e + l_t \cos\beta)^2},$$

and $\mu_{\text{eff}} = \sqrt{3\mu_a/l_t}$; $l_t = (\mu_s')^{-1}$ is the transport mean free path; z_e is the extrapolation length that depends on the mismatch of the index of refraction at the interface.[17] The extrapolation length is computed to be $z_e = 1.69 l_t$. Equation 2 is used to fit the measured diffuse reflectance along a line in the x direction on the tissue surface to obtain μ_a and l_t. The anisotropy factor g is then obtained using $g = 1 - (\mu_s'/\mu_s)$.

Fractal Soft Tissue Model for Determination of D_f and d_{max}. As many biological tissues have fractal-like organization and are statistically self-similar, various tissue light scattering models based on fractal geometry have been proposed. The distribution of the number density of particles of diameter d_i is given by[11,12]

$$n(d_i) = \frac{\eta_0 d_i^{3-D_f}}{\pi d_i^3/6} = \frac{6\eta_0}{\pi} d_i^{-D_f} \tag{3}$$

where D_f is the fractal volume dimension, η_0 is a scale-dependent constant, and $n(d_i)\Delta d$ gives the number density of the particles with diameters between d_i and $d_i + \Delta d$. The value of η_0 can be determined from the total volume fraction of all particles, T_v, using equations[11,12]

$$T_v = \eta_0 \int_{d_{\min}}^{d_{\max}} d_i^{3-D_f} \mathrm{d}d_i \Rightarrow \eta_0 = T_v \Big/ \int_{d_{\min}}^{d_{\max}} d_i^{3-D_f} \mathrm{d}d_i,$$

where $d_{\min}$ and $d_{\max}$ are diameters of the smallest and largest ?1
scattering particles, respectively.

The discrete particle model may not be appropriate to describe tissue inhomogeneities, as on a microscopic scale the constituents of tissue have no clear boundaries and merge into a quasi-continuum structure. As the refractive index variation in biological tissue is weak, tissue is better modeled as a continuous random medium where light scattering is not due to the discontinuities in refractive index but is considered to be a consequence of weak random fluctuations of the dielectric permittivity.

In such a fractal soft tissue model, the correlation function $R(r)$ of the random fluctuation of the refractive index is a weighted average of fluctuations over a range of correlation length l, that depends on the fractal dimension D_f and the cutoff length or the maximum correlation length, $d_{\max}$.[13] Light scattering property of the tissue is fully determined by the power spectrum (the Fourier transform) of $R(r)$. This model has been shown to be in good

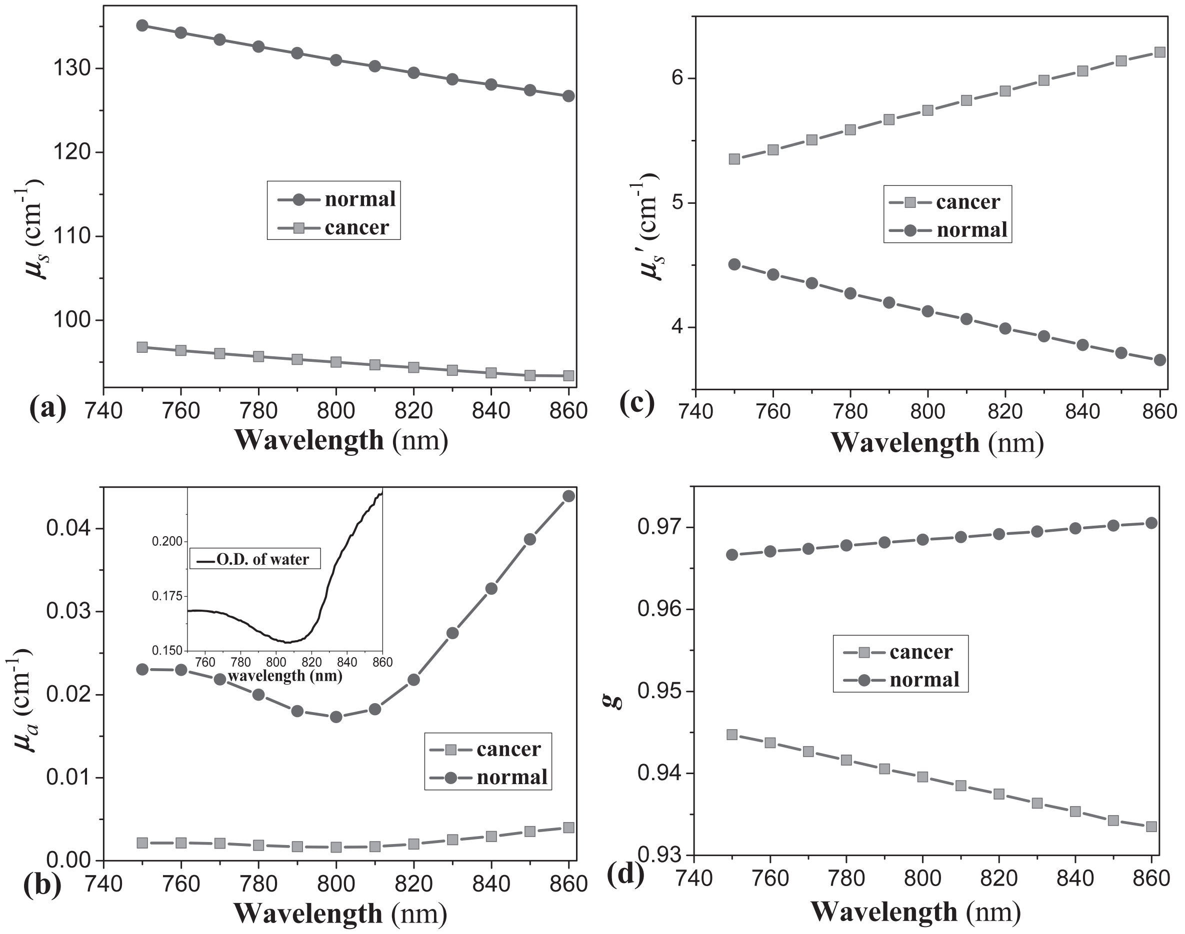

FIG. 2. The wavelength dependence of (**a**) the scattering coefficient (μ_s) of cancerous (solid square) and normal (solid circle) prostate tissues extracted from the measured optical density (O.D.) data in the spectral range of 750 nm to 860 nm using Eq. 1 in the text; (**b**) the absorption coefficient (μ_a) of cancerous (solid square) and normal (solid circle) prostate tissues; (**c**) the reduced scattering coefficients (μ_s') of cancerous (solid square) and normal (solid circle) prostate tissues. The absorption spectrum of water with 2 cm thickness in the spectral range of 750 to 860 nm is shown at upper left as a reference; and (**d**) the scattering anisotropy factor g of cancerous (solid square) and normal (solid circle) prostate tissues in the spectral range of 750 to 860 nm.

agreement with NIR light scattering experimental results in biological tissues and cell suspensions.[13,14]

The amplitude scattering function $S(\theta)$ at the scattering angle θ is given:[13]

$$|S(\theta)|^2 = \int_{kd_{\min}}^{kd_{\max}} \frac{\varepsilon^2 \eta_0 k^{D_f-1} x^{6-D_f}}{2\pi[1+2(1-\cos\theta)x^2]^2}\,dx \qquad (4)$$

where $\varepsilon^2 = 4n_0^4 \delta m^2$, $k \equiv 2\pi n_0/\lambda$, n_0 is the index of refraction of the surrounding medium, and δm is the amplitude of the relative refractive index fluctuation. The anisotropy factor (g), the mean cosine of the scattering angle, was then found as[13]

$$g = \int d\Omega \frac{(1+\cos^2\theta)\cos\theta|S(\theta)|^2}{2k^2} \Big/ \int d\Omega \frac{(1+\cos^2\theta)|S(\theta)|^2}{2k^2} \qquad (5)$$

where Ω is the solid angle and $d\Omega = 2\pi \sin\theta d\theta$ for a scattering angle θ.[13] The reduced scattering coefficient in the fractal soft tissue model follows a power law:

$$\mu_s' \propto \lambda^{3-D_f} \qquad (6)$$

This provides a simple procedure to estimate the fractal dimension D_f from the wavelength dependence of μ_s'.[13]

Using Eqs. 4 and 5, and the known value of $d_{\min}$, the variation of g as a function of $d_{\max}$ can be plotted in a $g \sim d_{\max}$ curve. Using the $g \sim d_{\max}$ curve, the maximum correlation length $d_{\max}$ can be obtained from any determined anisotropy factor g.

EXPERIMENTAL RESULTS AND ANALYSIS

Determination of Optical Coefficients of Cancerous and Normal Prostate Tissues. The wavelength dependence of μ_s, μ_a, μ_s', and g in the 750 to 860 nm spectral range is shown in Figs. 2a, 2b, 2c, and 2d, respectively. Typical values of the scattering coefficients (Fig. 2a) of the normal and cancerous prostate tissues at 800 nm were found to be $\mu_s^{\text{normal}} = 131.0 \pm 9.5$ cm^{-1} and $\mu_s^{\text{cancer}} = 94.9 \pm 6.1$ cm^{-1}, respectively. Over the entire wavelength range, the value of μ_s for normal prostate tissue is larger than that for cancerous prostate tissue, indicating that normal tissue scatters light more strongly than cancerous tissue. The gradual decrease in the value of μ_s with wavelength is consistent with Mie theory prediction. ?2

As Fig. 2b shows, the absorption coefficient of normal prostate tissue is higher than that of the cancerous tissue in the

750 to 860 nm spectral range, with typical values of $\mu_a^{normal} = (1.73 \pm 0.14) \times 10^{-2}$ cm^{-1} and $\mu_a^{cancer} = (1.62 \pm 0.13) \times 10^{-3}$ cm^{-1}, respectively at 800 nm. Comparison with the absorption spectrum of water in the inset shows that the absorption spectra of the tissues follow that of water closely, and the behavior is more prominent for the absorption spectrum of the normal tissue. This result indicates that water is the dominant absorptive tissue constituent in this spectral range. What is even more important is that water content is much higher in normal prostate tissues than in prostate tumors, an observation consistent with known relative abundance of water in normal and cancerous tissues.[4,5]

Reduced scattering coefficient (Fig. 2c) of normal prostate tissue decreases and that of cancerous prostate tissues increases monotonically in the 750 to 860 nm range, while the behavior is reversed for anisotropy factor g. The overall magnitude of μ_s' is significantly higher for cancerous prostate tissue than for normal prostate tissue, with typical values of $(\mu_s')_{normal} = 4.13 \pm 0.21$ cm^{-1} and $(\mu_s')_{cancer} = 5.74 \pm 0.19$ cm^{-1} at 800 nm. The observed lower values of g for cancerous tissue than that for normal tissue (Fig. 2d) follow readily from the behavior of μ_s' because of the simple algebraic relation between the two parameters. Typical values of g at 800 nm for normal and cancerous prostate tissues are estimated to be 0.968 ± 0.04 and 0.939 ± 0.06. It is intriguing that the g factor of normal tissue is always larger than that of cancerous tissues in this spectral range. Since μ_s, μ_s', and g depend on a number of parameters, such as index of refraction and scattering particles' size and distribution, detailed analysis is given in the next section using the fractal soft tissue model to illustrate the origin of these observations.

Numerical Evaluation of Fractal Dimension (D_f) and Cutoff Diameters of Scatterers in Cancerous and Normal Prostate Tissues. To study how the absorption and scattering spectra reflect micro-structural properties of cancerous and normal prostate tissues, we analyzed the scattering data of these two types of tissues numerically using the fractal soft tissue model outlined in the Theory section. The following parameters were used in our simulation: the total volume fraction of all scatterers $T_v = 0.2$,[11,12] the diameter of the smallest particle $d_{min} = 50$ nm,[11,18] the index of refraction of the cytoplasm of prostate tissue (host medium) $n_0 = 1.35$,[16] and the index of refraction of prostate cellular nuclei (scattering particles) $n_1 = 1.46$.[12–14,16]

The values of fractal dimension, D_f, were obtained by fitting the data shown in Fig. 2c using Eq. 6, and the results show that $D_f = 1.9 \pm 0.04$ and 4.4 ± 0.06 for the cancerous and normal prostate tissues, respectively.

The g values of the cancerous and normal prostate tissues at 800 nm as a function of cutoff diameter d_{max} were obtained using Eqs. 4 and 5, and the results are displayed as solid and dashed lines, respectively, in Fig. 3a. Using the previously determined values of g in Fig. 2d, the cutoff diameters of the cancerous and normal prostate tissues were found to be 1.42 ± 0.06 μm for the cancerous tissue and 6.48 ± 0.08 μm for the normal tissue.

The distribution of the number density as a function of the diameter d of scattering particles (scatterers) in cancerous and normal prostate tissues was then calculated using Eq. 3, and the results are shown as Fig. 3b. The salient feature of Fig. 3b is that the normal tissue has many more smaller scatterers than the cancerous tissue in the $d < \sim 0.6$ μm range while the cancerous tissue has more larger scatterers than the normal tissue in the $d > \sim 0.6$ μm range.

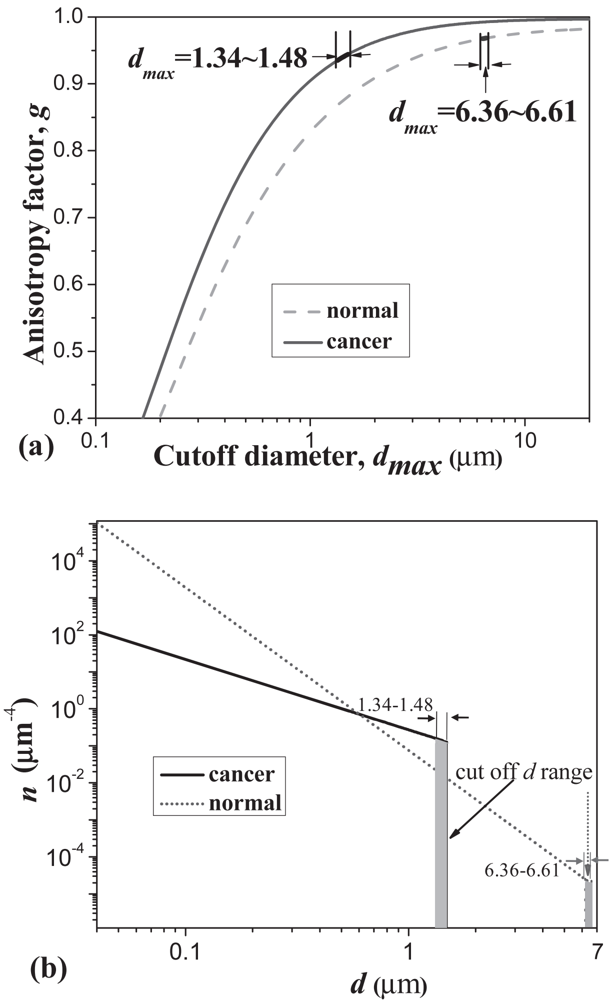

FIG. 3. (**a**) The anisotropy factor g of the cancerous and normal prostate tissues as a function of cutoff diameter d_{max} at 800 nm, and (**b**) distribution of the number density of scatterers with different diameters, evaluated by fractal tissue model using Eq. 3. The curves representing the behavior of cancerous and normal prostate tissues are displayed by solid and dashed lines, respectively. The cancerous prostate tissue (solid line) has lower weight of smaller particles and higher weight of larger particles than the normal prostate tissue (dashed line).

The fractal parameters for the normal and cancerous prostate tissues are summarized in Table I.

NEAR-INFRARED OPTICAL POLARIZATION IMAGING

The efficacy of near-infrared (NIR) optical imaging as a detection and diagnostic tool for prostate cancer will depend on the contrast between normal and cancerous prostate tissues, which arise from differences in intrinsic optical spectroscopic properties when no external agents are used. The differences in optical scattering coefficient and anisotropy factor reported in the previous section prompted us to explore the potential of NIR imaging in prostate cancer detection using a model prostate tissue sample consisting of a piece of cancerous tissue on the right side and a piece of normal tissue on the left side. The NIR spectral polarization imaging system is schematically shown in Fig. 1b. The sample with dimensions of ~2 cm × 3

TABLE I. D_f and d_{max} for cancerous and normal prostate tissues.

Tissue type	D_f	d_{max} (μm)
Cancer	1.9 ± 0.04	1.42 ± 0.06
Normal	4.4 ± 0.06	6.48 ± 0.08

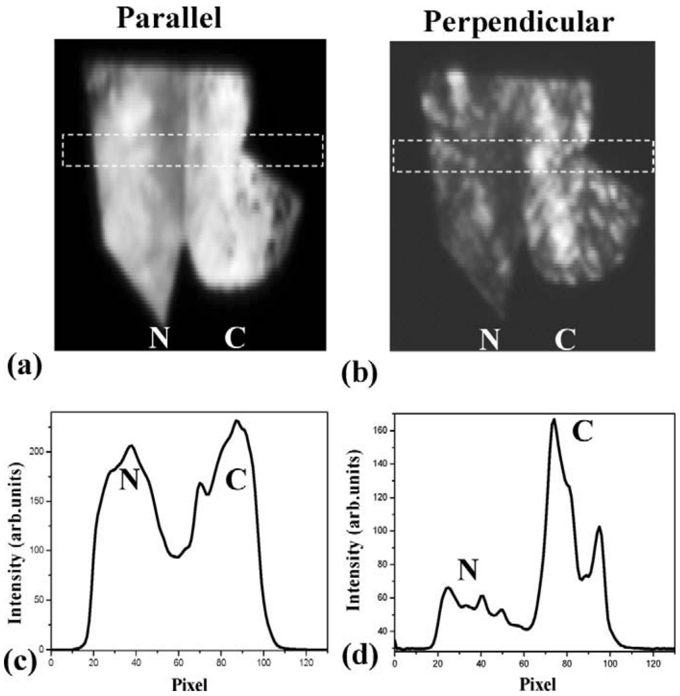

FIG. 4. Transmission images of a normal (N) and cancerous (C) human prostate tissue sample, obtained using 800 nm light for (**a**) parallel and (**b**) perpendicular polarization configurations. The size of tissue for imaging is ~2 cm × 3 cm × 0.035 cm (length × height × depth). (**c**, **d**) The digitized spatial intensity distributions of images (a) and (b), respectively, obtained by integrating the image intensity over the horizontal rectangular region as marked with the dashed boxes in (a) and (b).

cm × 0.035 cm was held between two glass plates under slight compression to ensure uniform thickness. Figures 4a and 4b display the polarization-gated images of the sample recorded with transmitted light polarized parallel and perpendicular to polarization of the incident light, respectively. The center wavelength of the imaging beam was 800 nm. It can be seen from Fig. 4 that the image of the right side of the sample (consisting primarily of cancerous tissue) is brighter than that of the left side (consisting mainly of normal tissue). This can be explained by the differences of scattering and absorption coefficients between cancerous and normal prostate tissues. Since both the scattering and absorption coefficients of the cancerous tissue at 800 nm are smaller than the corresponding coefficients of the normal tissue, as shown in Figs. 2a and 2b, the light propagating in the cancerous tissue undergoes less scattering and absorption. As a result, the light transmitted through the cancerous tissue area is stronger than that through the normal tissue.

The differences between the intensities transmitted through the cancerous and normal prostate tissue areas can be seen more clearly from the spatial intensity distributions obtained by integrating the image intensity over a horizontal rectangular region as marked with the dashed boxes in Figs. 4a and 4b. The integrated image intensity distributions for the images shown in Figs. 4a and 4b are displayed in Figs. 4c and 4d, respectively. The average image intensities of the cancerous tissue area were found to be 1.04 and 1.71 times stronger than that of the normal tissue area for the parallel and perpendicular images, respectively.

The image intensity distributions were also used to calculate the degree of polarization, defined as $P = (I_{||} - I_{\perp})/(I_{||} + I_{\perp})$, where $I_{||}$ and $I_{\perp}$ are intensities of transmitted light parallel and perpendicular to the polarization of the incident light beam, respectively. The value of P for the normal and cancerous prostate tissues at 800 nm are $P_{cancer} = 0.24$ and $P_{normal} = 0.46$. Similar higher values of P for normal tissue than for cancerous tissue are observed for images with other wavelengths in the 760 to 850 nm range. This is expected since the g factor of normal prostate tissue is larger than that of the cancerous tissue, as shown in Fig. 2d. Linearly polarized light propagating in a more strongly forward-peaked scattering medium (characterized by a larger value of g) is less depolarized in one scattering event. The smaller g factor for the cancerous tissue results in more depolarization and a smaller value of P in comparison with that in the normal tissue.[19]

DISCUSSION

In this paper we have presented the initial results of a study to explore potential correlation between optical properties and fractal dimensional parameters in normal and cancerous human prostate tissues. The extinction spectra of cancerous and normal prostate tissues in the 750 to 860 nm spectral range were used to obtain the scattering coefficient (μ_s). The absorption coefficient (μ_a) and the reduced scattering coefficient (μ_s') were acquired by fitting the diffuse reflectance of an obliquely incident beam using the diffusion model in a thick tissue sample. The values of μ_s' were found to be greater than μ_a by 2 to 3 orders of magnitude in this spectral range, and the results are consistent with literature values for prostate tissue.[7,8] The anisotropy factor g was calculated from μ_s and μ_s'.

A fractal soft tissue model was used to extract the values of fractal dimension (D_f) from the wavelength dependence of μ_s' and were found to be 1.9 and 4.4 for the cancerous and normal prostate tissues, respectively. The values are markedly different. Similar remarkable difference was observed in the values for cutoff diameter, d_{max}: 1.42 ± 0.06 μm for the cancerous tissue and 6.48 ± 0.08 μm for the normal tissue. Since the cutoff diameter may be considered to be an upper limit on the size of scatterers in tissue specimens, this result may be quite significant. Further probing revealed that the observed value of the cutoff diameter of the cancerous tissue (1.42 ± 0.06 μm) falls within the range of 1.38–1.96 μm for the nucleolar diameter of cancerous prostate cell,[20] and the cutoff diameter for normal tissue (6.48 ± 0.08 μm) closely matches the nuclear diameter of normal prostate cell (6.3–6.72 μm).[20] These close agreements point to the intriguing implication that in normal prostate cells the largest scatterers are the nuclei, while in cancerous prostate cells nucleoli are the largest scatterers. However, such a hypothesis raises the question why it is that the nucleoli represent the upper limit to the size of scatterers in cancerous cells, while nuclei determine the upper limit in normal cells. In this context it should be noted that the diameter of the normal prostate nucleoli lie in the 1.10 to 1.24 μm range, and that of cancerous nuclei is in the 8.4 to 10.31 μm range.[20]

A quantitative answer to this question is beyond the scope of this paper. However some qualitative and plausible observations based on the morphological changes associated with cancer and consequent changes in optical spectroscopic characteristics can be made in support of the hypothesis.[20–25] Normal cells, in general, are characterized by uniformity in size and shape of nuclei (round or oval) and have an ordered morphological structure.[21] The cell nucleus is dense and compact and may be considered as an entity with a localized index of refraction inhomogeneity. So, the entire nucleus acts as a scattering entity that happens to be larger than any other scatterer within the normal cell. This neat, regular, and ordered structure breaks down in cancerous cells. Malignant cells are characterized by irregular morphology, including changes in the shape and size of the nucleus, the nuclear envelope, the nucleolus, and the chromatin.[21] Richards-Kortum et al. found that light scattering is strongly influenced by the difference in morphology of nucleus and nucleolus, DNA content, and clumping and coarse chromatins.[22] Fischer et al. show that two important cell structure changes in human prostate cancer are nucleolar enlargement and nuclear envelope irregularity.[23] Varma et al. investigated the morphologic criteria for diagnosis of prostate adenocarcinoma in 250 consecutive cases and observed that dysplastic nuclei have irregular size and shape, clumps of condensed chromatin, and multiple nucleoli.[24] They suggest that the prominent nucleoli, marginated nucleoli (location of nucleoli is close to or at the inner nuclear membrane) and multiple nucleoli are criteria having highest sensitivity and specificity for diagnosis of prostate cancer.[24] To sum up, because of high density of malignant prostate cells, irregularity of nuclear envelope, enlargement of nucleoli, clumping and condensation of the chromatin and marginated nucleoli,[22–25] and fragmentation of nuclei and nuclear degeneration, it seems that nuclei no longer behave as the largest compact entities in cancerous cells when it comes to light scattering: that role is taken up by nucleoli.

Fractal model analysis of optical spectroscopic measurements on normal prostate tissues and prostate tumors at different stages of growth and different Gleason grades corroborated by microscopic and histological examinations of the samples will be needed to put the hypothesis presented above to stringent test. Affirmation of the hypothesis would imply that the fractal dimension and the cutoff diameter predicted by the fractal soft tissue model may be used as criteria for prostate cancer detection. The results further indicate that the NIR spectral polarization imaging[26] has the potential to be developed as a modality for prostate cancer detection.

ACKNOWLEDGMENTS

This research is supported in part by U.S. Army Medical Research and Material Command (USAMRMC) under the grants numbered W81XWH-08-1-0717, W81XWH-10-1-0526, and W81XWH-11-1-0335. The authors acknowledge the help of NDRI, CHTN, and HUMC for providing cancerous and normal prostate tissue samples for the measurements. Min Xu acknowledges Research Corporation and NIH (1R15EB009224) for additional support.

---

1. L. Goutzanis, N. Papadogeorgakis, P.M. Pavlopoulos, K. Katti, V. Petsinis, I. Plochoras, C. Pantelidaki, N. Kavantzas, E. Patsouris, C. Alexandridis. “Nuclear fractal dimension as a prognostic factor in oral squamous cell carcinoma”. Oral Oncol. 2008. 44: 345-353.
2. C. Morrison, J. Thornhill, E. Gaffney. “The connective tissue framework in the normal prostate, BPH and prostate cancer: analysis by scanning electron microscopy after cellular digestion”. Urol. Res. 2000. 28: 304-307.
3. R. Montironi, A. Filho, A. Santinelli, R. Mazzucchelli, R. Pomante, P. Colanzi, M. Scarpelli. “Nuclear changes in the normal-looking columnar epithelium adjacent to and distant from prostatic intraepithelial neoplasia and prostate cancer. Morphometric analysis in whole-mount sections”. Virchow Arch. 2000. 437: 625-634.
4. M. Chaplin. “Do we underestimate the importance of water in cell biology?” Nature Rev. Molecular Cell Biol. 2006. 7: 861-866.
5. P. Atluri, G.C. Karakousis, P.M. Porrett, L.R. Kaiser. “The Surgical Review: An Integrated Basic and Clinical Science Study Guide”. Lippincott Williams and Wilkins, ISBN 0781756413, 2005. Pp. 10-32.
6. A. Shmilovici. “Incomplete tumor volume reduction may improve cancer prognosis”. Med. Hypotheses. 2007. 68: 1236-1239.
7. W.-f. Cheong, S.A. Prahl, A.J. Welch. “A review of the optical properties of biological tissues”. IEEE J. Quant. Electron. 1990. 26: 2166-2185.
8. M. Xu, Y. Pu, W.B. Wang. “Clean image synthesis and target numerical marching for optical imaging with backscattering light”. Biomed. Opt. Exp. 2011. 2: 850-857.
9. J.W. Baish, R.K. Jain. “Fractals and Cancer”. Cancer Res. 2000. 60: 3683-3688.
10. M. Bizzarri, A. Giuliani, A. Cucina, F. D’Anselmi, A.M. Soto, C. Sonnenschein. “Fractal analysis in a systems biology approach to cancer”. Sem. Cancer Biol. 2011. 21: 175-182.
11. R.K. Wang. “Modeling optical properties of soft tissue by fractal distribution of scatterers”. J. Mod. Opt. 2000. 47: 103-120.
12. S.K. Sharma, S. Banerjee. “Volume concentration and size dependence of diffuse reflectance in a fractal soft tissue model”. Med. Phys. 2005. 32: 1767-1774.
13. M. Xu, R.R. Alfano. “Fractal mechanisms of light scattering in biological tissue and cells”. Opt. Lett. 2005. 30: 3051-3053.
14. M. Xu, T. Wu, J.Y. Qu. “Unified Mie and fractal scattering by cells and experimental study on application in optical characterization of cellular and subcellular structures”. J. Biomed. Opt. 2008. 13: 0240151-9.
15. M. Xu, M. Alrubaiee, S.K. Gayen, R.R. Alfano. “Determination of light absorption, scattering and anisotropy factor of a highly scattering medium using backscattered circularly polarized light”. Proc. SPIE. 2007. Optical interaction with tissue and cells XVIII. 6435: J1-6.
16. S.L. Jacques, S.A. Prahl. “Introduction to tissue optics”. 2002. http://omlc.ogi.edu/classroom/ece532/index.html.
17. J.X. Zhu, D.J. Pine, D.A. Weitz. “Internal reflection of diffusive light in random media”. Phys. Rev. A. 1991. 44: 3948-3959.
18. J.M. Schmitt, G. Kumar. “Optical Scattering Properties of Soft Tissue: A Discrete Particle Model”. Appl. Opt. 1998. 37: 2788-2797.
19. M. Xu, R.R. Alfano. “Random walk of polarized light in turbid media”. Phys. Rev. Lett. 2005. 95: 213905.
20. R. Montironi, R. Mazzucchelli, A. Santinelli, M. Scarpelli, A. Beltran, D. Bostwick. “Incidentally detected prostate cancer in cystoprostatectomies: pathological and morphometric comparison with clinically detected cancer in totally embedded specimens”. Human Pathol. 2005. 36: 646-654.
21. I. Ramzy. “Clinical cytopathology and aspiration biopsy”. The McGraw-Hill Companies, 2001.
22. R. Drezek, M. Guillaud, T. Collier, I. Boiko, A. Malpica, C. Macaulay, M. Follen, R. Richards-Kortum. “Light scattering from cervical cells throughout neoplastic progression: influence of nuclear morphology, DNA content, and chromatin texture”. J. Biomed. Opt. 2003. 8: 7-16.
23. A. Fischer. S. Bardarov Jr. and Z. Jiang “Molecular aspects of diagnostic nucleolar and nuclear envelope changes in prostate cancer”. J. Cell. Biochem. 2004. 91: 170-184.
24. M. Varma, M. Lee, P. Tamboli, R. Zarbo, R. Jimenez, P. Salles, M. Amin. “Morphologic criteria for the diagnosis of prostatic adenocarcinoma in needle biopsy specimens: A study of 250 consecutive cases in a routine surgical pathology practice”. Arch Pathol. Lab. Med. 2002. 126: 554-561.
25. S. Bektaş, B. Bahadir, B. Gün, G. Kertiş, Ş. Özdamar. “The relation between gleason score, and nuclear size and shape factors in prostatic adenocarcinoma. Turk J. Med. Sci. 2009. 39: 381-38.
26. Y. Pu, W.B. Wang, G.C. Tang, F. Zeng, S. Achilefu, J.H. Vitenson, I. Sawczuk, S. Peters, J.M. Lombardo, R.R. Alfano. “Spectral polarization imaging of human prostate cancer tissue using near-infrared receptor-targeted contrast agent”. Technol. Cancer Res. Treat. (TCRT). 2005. 4: 429-436.

Appendix 3

A page proof of a paper entitled “Stokes Shift Spectroscopy Pilot Study for Cancerous and Normal Prostate Tissues”, by E. Jeyasingh, Yang Pu, W. B. Wang, C. H. Liu, and R. R. Alfano, accepted by *Appl. Opt.*, (2012).

Stokes Shift Spectroscopy Pilot Study for Cancerous and Normal Prostate Tissues

E. Jeyasingh,[1] Y. Pu,[2] W. B. Wang,[2] C. H. Liu,[2] and R. R. Alfano[2,*]

[1]PG & Research Department of Physics, Jamal Mohamed College, Tiruchirappalli, Tamilnadu 620020, India

[2]Institue for Ultrafast Spectroscopy and Lasers, Department of Physics, The City College of New York,
160 Convent Avenue, New York, New York 10031, USA

*Corresponding author: ralfano@sci.ccny.cuny.edu

Received 6 March 2012; accepted 4 April 2012;
posted 10 April 2012 (Doc. ID 164088); published 0 MONTH 0000

Stokes shift spectroscopy (S3) is an emerging approach for cancer detection. The goal of this paper is to evaluate the diagnostic potential of the S3 technique for the detection and characterization of normal and cancerous prostate tissues. Pairs of cancerous and normal prostate tissue samples were taken from each of eight patients. Stokes shift spectra were measured by simultaneously scanning both the excitation and emission wavelengths while keeping a fixed wavelength interval $\Delta\lambda = 20$ nm between them. The salient features of this technique are the highly resolved emission peaks and significant spectral differences between the normal and cancerous prostate tissues, as observed in the wavelength region of 250 to 600 nm. The Stokes shift spectra of cancerous and normal prostate tissues revealed distinct peaks around 300, 345, 440, and 510 nm, which are attributed to tryptophan, collagen, NADH, and flavin, respectively. To quantify the spectral differences between the normal and cancerous prostate tissues, two spectral ratios were computed. The findings revealed that both ratio parameters $R_1 = I_{297}/I_{345}$ and $R_2 = I_{307}/I_{345}$ were excellent diagnostic ratio parameters giving 100% specificity and 100% sensitivity for distinguishing cancerous tissues from the normal tissue. Our results demonstrate that S3 is a sensitive and specific technique for detecting cancerous prostate tissue.

1. Introduction

Prostate cancer is the second leading cause of cancer death among American men. During 2010, an estimated 217,730 new prostate cancer cases were reported in the United States, and it was predicted that among them, 32,050 men might die [1]. Currently, prostate cancer diagnosis is based on a prostate specific antigen (PSA) test and digital rectal examination (DRE). If either of these two tests is abnormal, a biopsy is usually performed guided by transrectal ultrasound (TRUS). Although a TRUS-guided biopsy is considered the gold standard, it suffers from lack of sensitivity and specificity and leads to a significant number of false negatives, which then often leads to unnecessary biopsies, patient trauma, and the time needed to obtain a histopathological diagnosis [2]. Consequently, new detection technologies are needed that can overcome the current limitations and improve patient well-being.

Optical spectroscopy offers a novel diagnostic approach for tissue and can be considered as an alternative technique to conventional methods because of its advantages, such as minimal invasiveness, less time, and reproducibility. For more than three decades, various optical spectroscopic techniques for cancer diagnosis have been widely explored as potential diagnostic tools in the discrimination of normal from abnormal tissues. In 1980 s, Alfano's group first reported on the light-induced fluorescence differences from malignant and nonmalignant breast and lung tissues [3]. Since then, some groups around the world have reported the use of native fluorescence

---

1559-128X/12/160001-01$15.00/0

spectroscopy [4,5] and/or diffuse reflectance spectroscopy [6,7] for diagnosis of cancers in different organs. These reported studies indicate that optical spectroscopy has the potential to improve the screening and early detection of cancer. the optical spectra method, known as “optical biopsy,” as termed by Alfano, is a potential technique by which the medical community can diagnose tissues without removing them.

Native fluorescence of tissues, also called autofluorescence, is believed to be produced by several endogenous fluorophores, such as tryptophan, collagen, elastin, a reduced form of nicotinamide adenine dinucleotide (NADH), flavin adenine dinucleotide (FAD), and endogenous porphyrins. During the development from benign prostatic hyperplasia to premalignant (dysplastic) and malignant stages, prostate cells undergo proliferations that modify these fluorophore levels [8]. Additionally, the connective tissue frameworks of prostate tissue can be impaired during cancer development [9]. Such changes are likely to alter both tissue morphology and biochemistry, which could be detected using tissue fluorescence spectroscopy [10]. Thus, by measuring the fluorescence signal from tissue, changes in tissue structure and composition and information concerning the pathological state of the tissue could be obtained [11,12].

Cells/tissues contain several key fluorophores with broad and partly overlapped excitation and emission spectra [13]. Further, each fluorophore has a distinct absorption peak wavelength and a characteristic “fingerprint” peak emission wavelength [14]. The emission spectra at one or more excitation wavelengths or excitation spectra corresponding to one or more emission wavelengths have been used for diagnostic purposes [15]. The conventional laser-induced fluorescence spectroscopic method for cancer detection has limited applicability since most tissue fluorescence spectra have a series of overlapping bands from different fluorophores, and it often cannot be resolved satisfactorily by a single-excitation wavelength. To overcome this problem, multiple-excitation wavelengths are sequentially used to generate an excitation-emission matrix (EEM) in order to identify the optimal excitation wavelengths at which tissue classification is enhanced and to determine the origin of the measured fluorescence signal in a more reliable manner [5]. However, EEM measurement requires a large number of fluorescence emission scans at sequential excitation wavelengths at small wavelength intervals, and this is time- consuming. In order to reduce time consumption, a two-dimensional detector, such as a CCD camera, is used in conjunction with a spectrograph.

Alfano and Yang were the first to introduce the physical concept of Stokes shift spectroscopy (S3) as a rapid method for diagnosing diseased tissue that depends on both absorption and emission properties of the fluorophores [16]. In S3, the excitation wavelength λ_{ex} and the emission wavelength λ_{em} are scanned synchronously with a constant wavelength interval $\Delta\lambda = \lambda_{\mathrm{em}} - \lambda_{\mathrm{ex}}$ between the excitation and emission. Earlier, this technique was called synchronous fluorescence spectroscopy, and it begins with a multicomponent analysis to obtain spectral emission peaks of tissue samples, and it enhances the selectivity in the assay of complex systems [17]. Recently, S3 was used as a potential tool for the diagnostic purposes. Ebenezar *et al.* investigated the potential use of S3 as a diagnostic tool for the discrimination between normal and abnormal cervical and breast tissues [18,19]. Masilamani *et al.* studied the use of S3 in the discrimination of benign and malignant prostate tissues [20]. However, to the best of our knowledge, no report is available using S3 technique for the comparison and discrimination of cancerous and normal prostate tissues from the same patients. Therefore, this paper is designed to demonstrate the potential use of the S3 technique to detect and characterize the normal and cancerous prostate tissues from the same patients, and to determine the optimal offset wavelength $\Delta\lambda$ for distinguishing cancerous tissue from normal prostate tissue.

2. Materials and methods

A. Tissue Samples

A total of sixteen fresh human prostate tissue samples were collected from eight patients from the Cooperation Human Tissue Network (CHTN) under the
IRB approval of The City College of New York. Each 1
patient provided a pair of normal and cancerous samples. The spectroscopic data were classified into two groups: (1) normal and (2) cancerous tissues according to their post-spectroscopy studies. The optical biopsy of each tissue sample was compared to the histopathology analyses.

B. S3 Measurements

The Stokes shift (SS) spectra of *ex vivo* prostate tissues were recorded using spectrofluorometer (LS 50, PerkinElmer). The prostate tissue samples of solid chunks of approximately 1.5 mm × 1 mm × 0.3 mm (length × width × thickness) were placed in a quartz cuvette with the epithelium toward the face of the cuvette and the beam. The excitation light of approximately 2 mm × 4 mm was incident perpendicular to the face of the tissue epithelium surface, and the emitted fluorescence light was collected at a 90° angle to the excitation light. During data acquisition, the excitation and emission monochromators had fixed band passes of 3 nm each, and the wavelength increment was set at 0.5 nm. The variation in the excitation light source intensity as a function of wavelength was taken into account during SS spectra measurements. This was done by detecting
the fluorescence signal (S) by the PMT as well as re- 2
cording the reference excitation intensity (R) by a photodiode and taking their ratio S/R to serve as the final S3 signal to account for the wavelength-dependent light intensity.

C. Optimization of Offset Wavelength $\Delta\lambda$

The SS is dependent upon the vibrational and electronic interaction and the polarity of the host environment surrounding the emitting organic molecules. The wavelength interval of the SS spectrum can be simply compressed or expanded just by decreasing or increasing the selected $\Delta\lambda$ parameter [19]. During S3 acquisition, the excitation and emission monochromators were scanned simultaneously at the same speed with a constant wavelength interval $\Delta\lambda$ between them. In this paper, we investigated various $\Delta\lambda$ value, ranging from 10 to 50 nm, in increments of 10 nm. Among the five $\Delta\lambda$ alues, a $\Delta\lambda = 20$ nm revealed four key identifiable fluorophores with a good signal-to- noise ratio. Therefore, the value of $\Delta\lambda = 20$ nm was selected as the favored offset wavelength interval for the entire series of investigation. The S3 of normal and cancerous prostrate tissues were recorded in wavelengths of 250 to 600 nm, where $\Delta\lambda = 20$ nm, and with a scanning speed of 5 nm/sec. Because the S3 measurements involved the simultaneous scanning of both excitation and emission monochromators, significant contribution from the excitation light source was expected. By dividing each of the SS spectra by the lamp spectrum measured under the same instrumental parameters, the contribution from the excitation light source to the SS spectra was counted.

D. Statistical Analysis

The measured spectral data were analyzed statistically to discriminate cancerous tissue from normal prostate tissue. Data were initially preprocessed by normalizing each spectral profile with respect to the maximum fluorescence intensity of spectrum. From the normalized spectrum, two intensity ratios were calculated at different wavelengths corresponding to the characteristic spectral features of different groups of the prostate tissues studied. The mean and standard deviation values were calculated for each group of prostate tissue, and their statistical significance was verified using an unpaired Student's t-test to calculate the level of physical significance p with 95% confidence interval using origin statistical software (OriginPro7). The corresponding tissues, which yielded significant differences ($p < 0.005$) in the ratio values, were selected for further histopathological analyses.

The classification analysis was determined on the basis of discrimination cutoff values. Discrimination cutoff lines are drawn between the normal (mean of all normal tissues) and cancerous (mean of all cancer tissues), at values that correspond to the mean ratio value of the respective groups. The sensitivity and specificity in discriminating each of these categories were determined on the basis of the cutoff values identified by ratio method by validation with the gold standard, namely, histopathological results of biopsy specimens taken from SS emission measurement sites. Similar ratio intensity variable methods have been adopted by earlier researchers to discriminate normal from different tissue categories of bladder tissues, and the sensitivity and specificity were determined on the basis of the discrimination cutoff lines [5].

3. Results

The normalized mean S3 of cancerous (solid) and normal (dash) prostate tissues in the wavelength region between 250 and 600 nm is shown in Fig. 1. The normal tissues show a small hump around of 307 nm, with a single primary band centered at 345 nm, a small shoulder around 375 nm, and secondary peaks observed at 405, 440 and 510 nm. Although cancerous tissue is found to exhibit two primary, highly resolved bands at 297 and 345 nm, with secondary peaks observed at 440 and 510 nm, and the spectral band at 297 nm was higher than that at 345 nm. From this normalized spectrum, it was also observed that all the spectral bands are highly resolved, and one could discern the spectral shift of primary emission bands between normal and cancerous tissues. For example, the normalized spectra of normal tissues show an emission band at 307 nm, which was blueshifted to 297 nm for cancerous tissues. In addition, a spectral dip or valley was also observed around 425 nm for normal and cancerous tissues. It was noted that the valley at 425 nm is deeper in the case of cancerous than normal tissues.

A. S3 Measurements of Standard Fluorophores

To investigate the origin of the observed spectral peaks from normal and cancerous prostate tissues and to assign them to various endogenous fluorophores, the S3 of commercially obtained fluorophores (Sigma Chemicals, USA) of tryptophan, collagen, NADH, and FAD were measured with the same experimental parameters maintained as for the prostate tissues. The SS spectra of the commercial-grade fluorophores were corrected for the variation in the lamp intensity and normalized with respect to the corresponding peak intensity. Figure 2 shows the normalized SS spectra of the standard fluorophores,

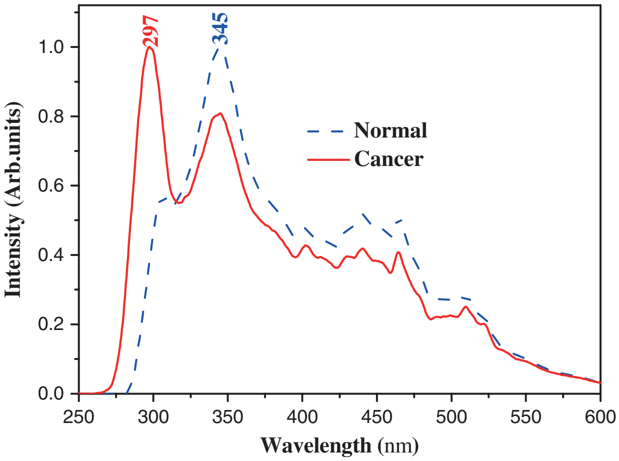

Fig. 1. (Color online) Normalized mean Stokes shift spectra of cancerous (solid) and normal (dash) prostate tissues.

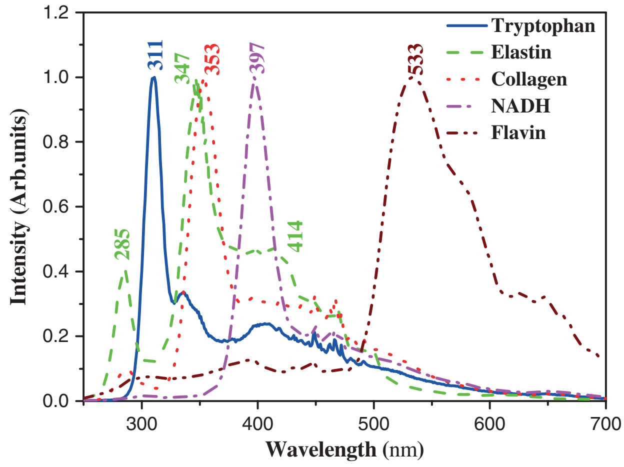

Fig. 2. (Color online) Normalized Stokes shift spectra of standard fluorophores of tryptophan (solid), elastin (dash), collagen (dot), NADH (dash dot), and FAD (dash dot dot).

such as tryptophan (solid), elastin (dash), collagen (dot), NADH (dash dot) and FAD (dash dot dot), with their narrow emission peaks observed at 311, 347, 353, 397 and 533 nm, respectively. The SS spectra of elastin also showed secondary peaks at 285 nm, with a small shoulder around 414 nm. Further, the fine structures observed in the wavelength region between 440 and 500 nm may be due to the stray light contribution from the xenon lamp passing through the exit slit of the excitation monochromator. A sharp spectral feature was observed at 467 nm due to the contribution from the xenon lamp source.

B. Results of Statistical Analysis

In order to validate the diagnostic utility of the observed spectral signatures between normal and cancerous tissues, two ratio variables were introduced for SS spectra, with $\Delta\lambda = 20$ nm. The mean and standard deviation of the SS spectral ratios of normal and cancerous prostate tissues were calculated, and the results are listed in Table 1 along with p values. The statistical significance was computed through an unpaired Student's t-test to determine the level of significance p. The p values for both the ratio variables are less than 0.005, indicating a high statistical significance. From Table 1, for both ratio variables $R_1 = I_{297}/I_{345}$ and $R_2 = I_{307}/I_{345}$, the mean value of the normal tissue was lower than that of the cancerous tissue. In the SS spectrum, it is the relative intensities between the maxima that are of importance rather than the numerical intensity value of each maximum. Table 1 shows the computed ratios of the fluorescence peak intensities at 297 to 345 nm (R_1), and 307 to 345 nm (R_2), correlating with their histologic findings. For example, the mean ratio value of R_1 in normal tissues was 0.36 ± 0.05, which is significantly different from the mean value of 1.24 ± 0.09 in cancerous tissues (unpaired Student's t-test, $p < 0.005$). By selecting the I_{297}/I_{345} of ~0.80 as the demarcation ratio level (between the normal and cancerous tissues), it is found to yield 100% specificity and 100% sensitivity for differentiating cancerous from normal tissues (Fig. 3). Similarly, the mean ratio value of R_2 for normal tissue was 0.57 ± 0.05, which is also significantly different from the mean value of 0.92 ± 0.05 for cancerous prostate tissues (unpaired Student's t-test, $p < 0.005$). By selecting I_{307}/I_{345} of ~0.74 as a cutoff for tissue demarcation, 100% specificity and 100% sensitivity were achieved (Fig. 4).

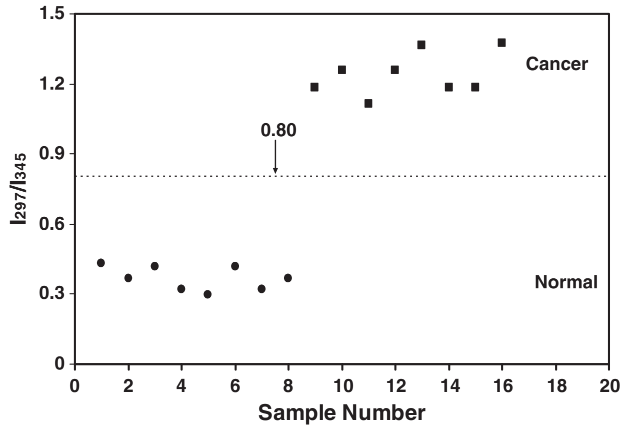

Fig. 3. Scatter plot of intensity ratio of I_{297}/I_{345} for normal (●) and cancerous (■) prostate tissues.

4. Discussion

The potential use of the S3 technique in detection and characterization of normal and cancerous prostate tissues was explored, and the spectral data were analyzed by a simple statistical method, which validated the diagnostic potentiality of the present method. The comparison of S3 spectra of normal and cancerous tissues with those corresponding to commercial-grade standard fluorophores suggests that the peaks observed around 297, 307, 345, 440, and 510 nm may be primarily attributed to tryptophan, collagen and/or elastin, NADH, and FAD respectively. Similar peaks of S3 were reported earlier in the discrimination of normal and different pathological studies of cervical tissues [18]. In this paper, the

Table 1. Mean ±SD of the Stokes Shift Spectral Ratios of Normal and Cancerous Prostate Tissues

Tissue types	Spectral Intensity At 297 nm	At 307 nm	At 345 nm	Intensity ratio $R_1 = I_{297}/I_{345}$	Intensity ratio $R_2 = I_{307}/I_{345}$
Normal	0.36 ± 0.05	0.57 ± 0.05	0.99 ± 0.00	0.36 ± 0.05	0.57 ± 0.05
~~Cancer-ous~~	0.98 ± 0.01	0.73 ± 0.03	0.79 ± 0.05	1.24 ± 0.09	0.92 ± 0.05
P value	<0.005	<0.005	<0.005	<0.005	<0.005

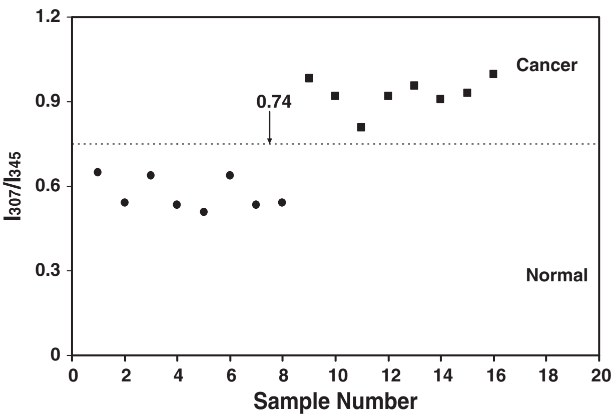

Fig. 4. Scatter plot of intensity ratio of I_{307}/I_{345} for normal (•) and cancerous (■) prostate tissues.

wavelengths of the spectral peaks observed for prostate tissues were not exactly the same as those of the standard fluorophores. This observed spectral shift of the peak positions in the spectra of prostate tissues may be due to the different microenvironments of these endogenous fluorophores in tissues. In particular, the band position of standard fluorophore of NADH at 397 nm does not exactly match our prostate tissue band position, which has been observed around 440 nm. Earlier reported studies have shown that exact determination of NADH emission is difficult because this compound significantly changes the spectral shape and intensity after undergoing oxidation after resection [13]. In addition, the fluorescence data of NADH compound obtained from *ex vivo* tissue may not accurately represent the *in vivo* or living situation [21]. Thus oxidation of tissue fluorophores will influence the fluorescence properties of the tissues, which leads to change in spectral peak positions and the line width and fluorescence intensities [22,23].

Distinct salient differences in the spectral signatures of tryptophan, collagen and/or elastin, NADH, and FAD were observed from normal and different pathological conditions of prostate tissues, as shown in Fig. 1. The normal tissue exhibits a small peak around 307 nm, most likely due to tryptophan, an aromatic amino acid. This peak was significantly higher, and it shifted to 297 nm for cancerous tissues. Table 1 also shows that the intensity of the tryptophan emission band was higher in the cancerous tissues (0.98 ± 0.01 at 297 nm and 0.73 ± 0.03 at 307 nm) than in normal tissues (0.36 ± 0.05 at 297 nm and 0.57 ± 0.05 and 307 nm). Significantly, the tryptophan emission band was lower (0.57 ± 0.05 at 307 nm) for normal tissues, and it was noticed that the same band was blueshifted with increased emission intensity (0.98 ± 0.01 at 307 nm) for cancerous tissues. The striking observation is the increase in the tryptophan fluorescence signals in cancerous tissues relative to its normal counterpart. This increase is probably due to hyperactivity or epithelium glandular proliferation resulting in higher transient concentration of proteins in cells and/or increased thickness of the epithelium [9,24]. The observed increase in tryptophan fluorescence correlates with the earlier reported data on cervical epithelial cancer cells, non-melanoma, and bladder cancerous tissues [4,5,25]. In addition to the increase in tryptophan fluorescence intensity, the peak emission wavelength was blueshifted to 297 nm for cancerous tissues in comparison with the normal tissues. This observed blueshift may be attributed to changes in the local microenvironment and conformational changes of the protein-bound tryptophan, relative to the free amino acid [26]. Similar spectral blueshifts have been noted in human laryngeal epithelial cells [27], carcinogen-transformed human bronchial epithelial cells [28], and SS spectra of breast tissues [19]. Further, it is suggested that sensitivity of tryptophan fluorescence and its peak emission due to polarity and mobility of environment makes tryptophan fluorescence useful for monitoring structural changes in a protein [29]. Based on the results, it is concluded that changes in intrinsic tryptophan fluorescence and its peak emission wavelength from cancerous prostate tissues can be used as one of the diagnostic criteria for classifying early neoplastic changes.

The structural proteins collagen and/or elastin have been noted in the S3 spectrum. As we know, collagen and/or elastin is a major component of extracellular matrix and dominates the stoma fluorescence associated with crosslinks. From Fig. 1, the primary prominent band was observed for the normal tissue at 345 nm, corresponding to structural protein collagen and/or elastin, with a small shoulder around 375 nm, and secondary peak was observed at 405 nm due to elastin. These bands are drastically decreased in the cases of cancerous prostate tissues. Table 1 also shows that the intensity of collagen emission band (0.99 ± 0.00 at 345 nm) was high in normal tissues and low (0.79 ± 0.05 at 345 nm) in cancerous tissues. In normal prostate tissues, the collagen and elastin network is dense, with larger numbers of fibers compared to non-uniform of size and shape of the epithelial cells, and loss and disintegration of collagen and elastin fibers in the cancerous prostate tissue was expected [24,30,31]. The significant decrease of collagen and/or elastin fluorescence in cancerous prostate tissues may be due to structural changes in the epithelium, and sub-epithelial collagen network may be due to nuclear enlargement and because epithelial cells are crowded with increased cell density, loss of cellular maturation, and overall thickening of the epithelium [81032]. Thus, increased thickness of the epithelium in malignant prostate glands attenuates both excitation light and emission fluorescence light from the vascular stroma, leading to reduced penetration depth of the excitation light as well as the re-absorption of the emitted fluorescence. This may present a potential criterion for prostate cancer detection. This criterion agreement with reported studies has shown that collagen fluorescence is decreased in cancerous prostate tissues [8].

The characteristic hemoglobin absorption features were clearly found as a dip at 420 nm for normal and cancerous prostate tissues. The hemoglobin absorption is deeper in the case of cancerous tissues than for normal tissues due to possible increase of hemoglobin content from angiogenesis [32]. Most cancerous tissue is known to exhibit increased vasculature due to angiogenic developments with recurrence in hypoxia, and, hence, there is increased blood content in superficial tissue layers, which leads to increased hemoglobin absorption when compared to normal tissues [33]. This hypothesis is also consistent with the findings of earlier reports on S3 of cervical [18] and breast tissues [19] and other studies by Demos *et al.* [14] and Volynskaya *et al.* [34].

In addition to this, in Fig. 1, the normal tissue exhibits a broad peak around 440 nm and has a small sharp peak at 510 nm at a longer wavelength. However, cancerous prostate tissues also reveal similar spectral bands but with a less fluorescence intensity compared with the normal tissues. The observed spectral bands at 440 and 510 nm may be attributed to the coenzyme of NADH and FAD. The relative decrease of NADH and FAD fluorescence in malignant prostate tissues may be due to changes in tissue morphology (thickening of epithelium), the decrease of fluorophores (NADH and FAD) quantum yields, and/or oxidation of tissue fluorophores [5,22].

The present result shows that the overall S3 signature provides information about tissue architecture (epithelial thickness), changes in absorption due to hemoglobin, and concentration of fluorescing molecules, which can be correlated to histological changes. Therefore, alteration in tissue architecture that inhibits excitation photons from reaching the native fluorophores and/or the emission photons from the fluorophores from escaping from the tissue could be detected by the S3. Additionally, as the hemoglobin concentration increased, the fluorescence intensity decreased and the fluorescence profile was altered significantly. Thus, changes in the concentration of the key native fluorophores could alter the emitted fluorescence in a single scan, which is manifested in our study.

Many studies have been reported that the fluorescence spectral intensity ratio could be used as a potential tool for tissue diagnosis [5,18–20]. In this paper, a simple classification method was adopted based on the ratio values estimated from the intensities at different wavelengths characterizing the peaks of different groups under study. To quantify the observed spectral results and to estimate the diagnostic potentiality of the present technique, two intensity ratios, such as I_{297}/I_{345} for normal tissues and I_{307}/I_{345} for cancerous tissues, were selected. Each emission wavelength used in these ratios represents a specific fingerprint of one fluorophore. The component identified as I_{307} represents the peak emission wavelength of tryptophan for normal tissues, whereas I_{207} represents the peak emission wavelength of tryptophan for cancerous tissues, and I_{345} represents the peak emission wavelength of collagen and/or elastin from normal and cancerous tissues. Both intensity ratio values increase significantly for cancerous tissues in comparison with normal tissues. From these ratio parameters, we found variations in the relative distribution of tryptophan, collagen and/or elastin corresponding to the different histopathology of the tissues.

In this paper, we performed the classification analysis for two ratio parameters (I_{297}/I_{345} and I_{307}/I_{345}) in order to find out the specificity and sensitivity of the present technique to discriminate between two groups. Figure 3 shows the scatter plot of the spectral intensity ratio of I_{297}/I_{345} from sixteen samples from eight patients categorized as normal prostate tissues ($n = 8$) and cancerous prostate tissues ($n = 8$). The classification specificity and sensitivity in discriminating each of these categories were determined on the basis of discrimination cutoff values, given in the scatter plot (Fig. 3). For example, the cutoff line discriminating the normal from the cancerous was drawn at 0.80, corresponding to the mean ratio of normal (0.36) and the mean of the cancerous (1.24) group. For the I_{297}/I_{345} ratio, by selecting a cutoff at the mean (0.80) of the normal and cancerous tissues yield, 100% specificity and 100% sensitivity was obtained for discrimination of the normal from the cancerous. Similarly, we performed other ratio parameter I_{307}/I_{345} for the same classification analysis. Figure 4 shows the scatter plot of the spectral intensity I_{307}/I_{345} ratio, the cutoff line drawn at 0.74 discriminates the normal from cancerous, with the specificity and sensitivity of 100% and 100%, respectively.

Statistical analysis showed that both intensity ratios yielded 100% diagnostic sensitivity and specificity. Since the increased value of the fluorescence ratios of I_{297}/I_{345} and I_{307}/I_{345} for cancerous prostate tissues compared to normal tissue reflects an increase in the tryptophan fluorescence contribution and a decrease in the collagen and/or elastin fluorescence contribution. Among the all the fluorophores, the finding of increased band of tryptophan fluorescence and decreased fluorescence of collagen and/or elastin band from prostate cancer could be particularly useful for detecting prostate cancer.

The major advantage of the S3 technique is that all the fluorophores in complex structures, such as tissue, are excited under optimal conditions, such as wavelength of excitation, slit widths, scan speed, and scan range, which is practically impossible in the case of conventional fluorescence measurements. In the case of conventional fluorescence measurements, optimal conditions are chosen based on the fluorophores of interest. Though, EEM offers great resolution, it takes some time to carry out, even with multichannel detectors. Also, the large amount of data of EEM could significantly slow down the data processing procedures and clearly is impractical in a clinical setting. On the other hand, S3 represents the diagonal scan over the entire EEM, thereby reducing the time of data acquisition without any alterations in the details over the entire spectral range of the different fluorophores present in the different tissues. The S3 technique reduces the time of data acquisition and can be identified in a specific spectral range with narrower spectral band attributed by each fluorophore than the conventional fluorescence spectrum. S3 improves the diagnostic capability of optical spectroscopy for prostate cancer diagnosis because all the key fluorophores, such as tryptophan, collagen and/or elastin, hemoglobin absorption, NADH, and FAD, can be obtained in a single scan [16], and they are reported as cancer markers [8–11]. On the basis of above factors, S3 may also be considered as a technique alternative or/and complementary to the existing conventional methods for tissue diagnosis.

5. Conclusion

This paper suggests that S3 holds the potential for differentiating between diseased and normal prostate tissues *in vitro*. Results of the current study demonstrate that spectral changes due to the changes of contents of tryptophan, collagen and/or elastin, NADH, and FAD have good diagnostic potential. Two ratio parameters ($R_1 = I_{297}/I_{345}$ and $R_2 = I_{307}/I_{345}$) were empirically selected and evaluated by an unpaired Student's t-test, which showed useful diagnostic information with excellent discrimination of mean ratio values between normal and cancerous prostate groups. To improve on the diagnostic capability of S3, a larger number of samples of normal and different pathological prostate tissues would need to be validated in blinded manner. Such investigations with a large group of tissue biopsies will be useful for the development of a statistical database and a user-friendly diagnostic algorithm that could facilitate a real-time *in vivo* clinical diagnosis of prostate cancer. Currently, we are working on the above aspects to prove S3 as a useful and novel technique in the diagnostic clinical oncology for different tissue types.

This research is supported in part by U.S. Army Medical Research and Material Command under grants W81XWH-08-1-0717 (CUNY RF 47170-00-01) and W81XWH-11-1-0335 (CUNY RF # 47204-00-01). The authors gratefully acknowledge the help of CHTN for providing normal and cancerous prostate tissue samples for the measurements. E. Jeyasingh specially thanks A. Alimova and G. C. Tang for their help to use the spectrofluoremeter in IUSL at CCNY. Jeyasingh also gratefully acknowledges the Department of Science and Technology (DST), Government of India, for providing the travel grant to carry out this study.

References

3 1. American Cancer Society, Cancer Facts and Figures (American Cancer Society, 2009).
2. L. V. Rodriguez and M. K. Terris, "Risks and complications of transrectal ultrasound guided prostate needle biopsy: a prospective study and review of the literature," J. Urol. (Baltimore) **160**, 2115–2120 (1998).
3. R. R. Alfano, D. Tata, J. Cordero, P. Tomashefsky, F. Longo, and M. Alfano, "Laser-induced fluorescence spectroscopy from native cancerous and normal tissue," IEEE J. Quantum Electron. **20**, 1507–1511 (1984).
4. R. R. Alfano, G. C. Tang, A. Pradhan, W. Lam, D. J. Choy, and E. Opher, "Fluorescence spectra from cancerous and normal human breast and lung tissues," IEEE J. Quantum Electron. **23**, 1806–1811 (1987).
5. W. Zheng, W. Lau, C. Christopher, K. C. Soo, and M. Oliva, "Optimal excitation-emission wavelengths for autofluorescence diagnosis of bladder tumors," International Journal of cancer control and prevention **104**, 477–481 (2003).
6. Y. Yang, E. J. Celmer, J. A. Koutcher, and R. R. Alfano, "UV reflectance spectroscopy probes DNA and protein changes in human breast tissues," Journal of clinical laser medicine and surgery **19**, 35–39 (2001).
7. G. M. Palmer, C. Zhu, T. M. Breslin, F. Xu, K. W. Gilchrist, and N. Ramanujam, "Comparison of multiexcitation fluorescence and diffuse reflectance spectroscopy for the diagnosis of breast cancer," IEEE Trans. Biomed. Eng. **50**, 1233–1242 (2003).
8. Y. Pu, W. Wang, G. Tang, and R. R. Alfano, "Changes of collagen and nicotinamide adenine dinucleotide in human cancerous and normal prostate tissues studies using native fluorescence spectroscopy with selective excitation wavelength," J. Biomed. Opt. **15**, 047008 (2010).
9. C. Morrison, J. Thornhill, and E. Gaffney, "The connective tissue framework in the normal prostate, BPH and prostate cancer: analysis by scanning electron microscopy after cellular digestion," Urol. Res. **28**, 304–307 (2000).
10. I. Georgakoudi, B. C. Jacobson, M. G. Muller, E. E. Sheets, K. Badizadegan, D. L. Carr-Locke, C. P. Crum, C. W. Boone, R. R. Dasari, J. Van Dam, and M. S. Feld, "NAD(P)H and collagen as in vivo quantitative fluorescent biomarkers of epithelial precancerous changes," Cancer Res. **62**, 682–687 (2002).
11. R. Richards-Kortum and E. Sevick-Muraca, "Quantitative optical spectroscopy for tissue diagnosis," Annu. Rev. Phys. Chem. **47**, 555–606 (1996).
12. D. C. G. De Veld, M. Skurichina, M. J. H. Witjes, R. P. W. Duin, H. J. C. M. Sterenborg, W. M. Star, and J. L. Roodenburg, "A clinical study for classification of benign, dysplastic, and malignant oral lesions using autofluorescence spectroscopy," J. Biomed. Opt. **9**, 940–950 (2004).
13. L. Rigacci, R. Alterini, P. A. Bernabei, P. R. Ferrini, G. Agati, F. Fusi, and M. Monici, "Multispectral imaging autofluorescence microscopy for the analysis of lymph-node tissues," Photochem. Photobiol. **71**, 737–742 (2000).
14. S. G. Demos, A. J. Vogel, and A. H. Gandjbakhche, "Advances in optical spectroscopy and imaging of breast lesions," J. Mammary Gland Biol. Neoplasia **11**, 165–181 (2006).
15. Y. Yang, E. J. Celmer, M. J. Szczepaniak, and R. R. Alfano, "Excitation spectrum of malignant and benign breast tissues: a potential optical biopsy approach," Lasers Life Sci. **7**, 249–265 (1996). 4
16. R. R. Alfano and Y. Yang, "Stokes shift emission spectroscopy of human tissue and key biomolecules," IEEE J. Quantum Electron. **9**, 148–153 (2003).
17. T. Vo-Dinh, "Multicomponent analysis by synchronous luminescence luminescence spectrometry," Anal. Chem. **50**, 396–401 (1978).
18. J. Ebenezar, P. Aruna, and S. Ganesan, "Synchronous fluorescence spectroscopy for the detection and characterization of cervical cancers in vitro," Photochem. Photobiol. **86**, 77–86 (2010).
19. J. Ebenezar, P. Aruna, and S. Ganesan, "Stokes shift spectroscopy for breast cancer diagnosis," Proc. SPIE **7561**, 75610B (2010).
20. V. Masilamani, D. Rabah, M. Alsalhi, V. Trinka, and P. Vijayaraghavan, "Spectra discrimination of benign and malignant prostate tissues: a preliminary report," Photochem. Photobiol. **87**, 208–214 (2011).
21. R. S. DaCosta, H. Andersson, and B. C. Wilson, "Molecular fluorescence excitation-emission matrices relevant to tissue spectroscopy," Photochem. Photobiol. **78**, 384–392 (2003).

22. B. Chance, B. Schoener, R. Oshino, F. Itshak, and Y. Nakase, “Oxidation-reduction ratio studies of mitochondria in freeze-trapped samples: NADH and flavoprotein fluorescence signals,” J. Biol. Chem. **254**, 4764–4771 (1971).
23. D. C. G. De Veld, T. C. Bakker Schut, M. Skurichina, M. J. H. Witjes, J. E. Van der Wal, J. L. N. Roodenburg, and H. J. C. M. Sterenborg, “Autofluorescence and Raman microspectroscopy of tissue sections of oral lesions,” Lasers Med. Sci. **19**, 203–209 (2005).
24. M. McLaren, “Prostate gland,” *Toronto Health and Nutrition* (2008), http://www.atozhealthguide.com/index2.php?optioncom_content&do_pdf=1&id=56-. **5**
25. D. L. Heintzelman, R. Lotan, and R. Richards-Kortum, “Characterization of autofluorescence of polymorphonuclear leukocytes, mononuclear leukocytes and cervical epithelial cancer cells for improved spectroscopic discrimination of inflammation from dysplasia,” Photochem. Photobiol. **71**, 327–332 (2000).
26. J. R. Lackowicz, *Principles of Fluorescence Spectroscopy* (Plenum, 1983).
27. D. Parmeswarn, S. Ganesan, R. Nalini, P. Aruna, V. Veeraganesh, and R. R. Alfano, “Native cellular fluorescence characteristics of normal and malignant epithelial cells from human larynx,” Proc. SPIE **2979**, 759–764 (1997).
28. J. D. Pitts, R. D. Sloboda, K. H. Dragnev, E. Dmitrovsky, and M. A. Mycek, “Autofluorescence characteristics of immortalized and carcinogen-transformed human bronchial epithelial cells,” J. Biomed. Opt. **6**, 31–40 (2001).
29. A. S. Ladokhin, “Fluorescence spectroscopy in peptide and protein analysis,” in Encyclopedia of Analytical Chemistry, R. A. Meyers, ed. (Wiley, 2000), pp. 5762–5779.
30. C. Morrison, J. Thornhill, and E. Gaffney, “The connective tissue framework in the normal prostate, BPH and prostate cancer: analysis by scanning electron microscopy after cellular digestion,” Urol. Res. **28**, 304–307 (2000).
31. D. F. Gleason and G. T. Mellinger, “Prediction of prognosis for prostatic adenocarcinoma by combined histological grading and clinical staging,” J. Urol. **111**, 58–64 (1974).
32. R. Drezek, K. Sokolov, U. Utzinger, I. Boiko, A. Malpica, M. Follen, and R. Richards-Kortum, “Understanding the contributions of NADH and collagen to cervical tissue fluorescence spectra: modeling, measurements, and implications,” J. Biomed. Opt. **6**, 385–396 (2001).
33. M. M. Sholley, G. P. Ferguson, and H. R. Seibel, “Mechanisms of neovascularization: vascular sprouting can occur without proliferation of endothelial cells,” Laboratory investigation **51**, 624–634 (1984).
34. Z. Volynskaya, A. S. Haka, K. L. Bechtel, M. Fitzmaurice, R. Shenk, N. Wang, J. Nazemi, R. R. Dasari, and M. S. Feld, “Diagnosing breast cancer using diffuse reflectance spectroscopy and intrinsic fluorescence spectroscopy,” J. Biomed. Opt. **13**, 024012 (2008).

Appendix 4

A paper entitled “Near Infrared Photonic Finger Imager for Prostate Cancer Screening”, by Y. Pu, W. B. Wang, M. Xu, G. C. Tang, Y. Budansky, M. Sharanov, S. Achilefu, J. A. Eastham and R. R. Alfano, published in *Technol. Cancer Res. Treat.*, (*TCRT*), 10, 507-517 (2011).

TCRT
Technology in Cancer Research & Treatment

Volume 10, Issue 6, December 2011, ISSN 1533-0346

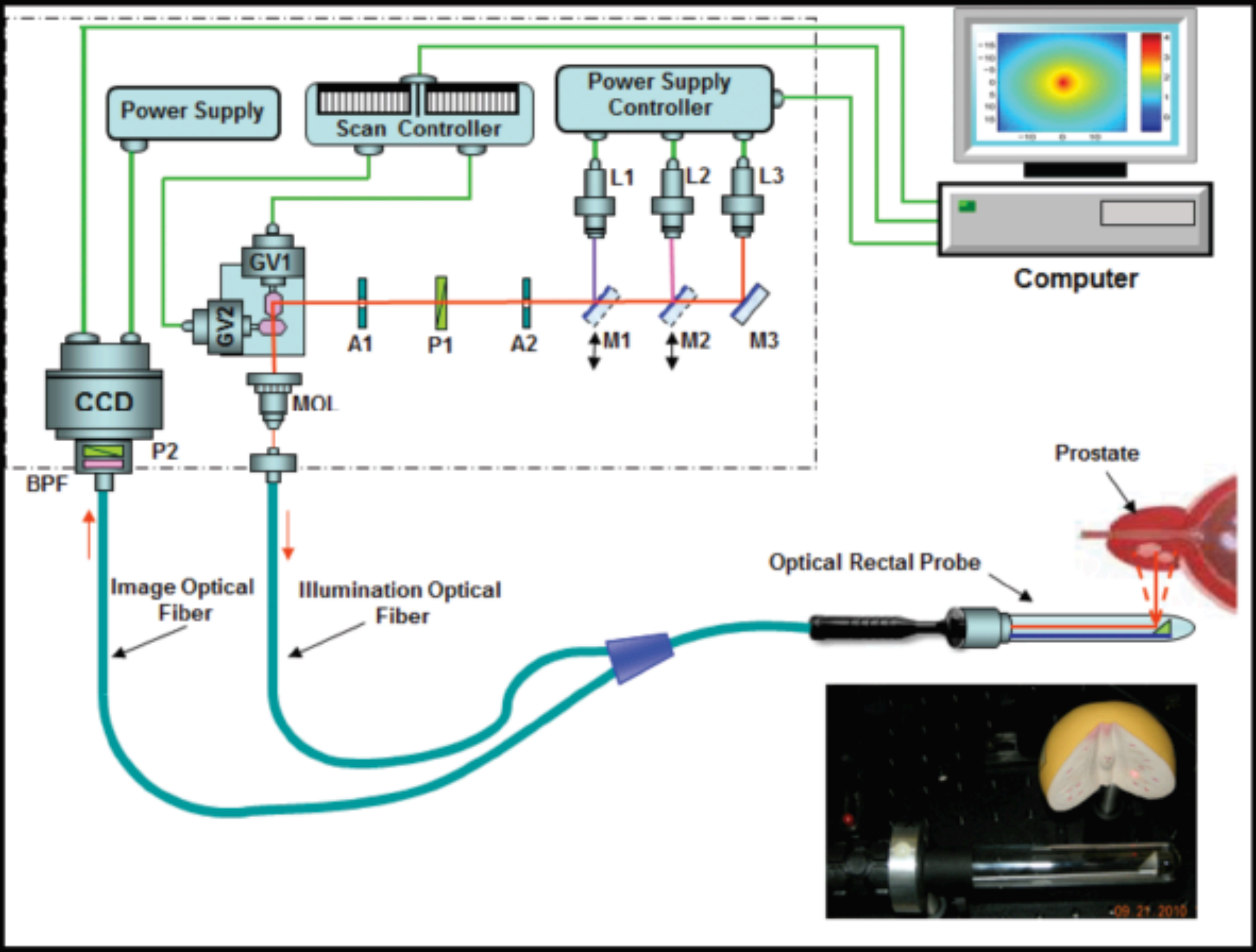

A bimonthly publication of
Adenine Press
2066 Central Avenue
Schenectady NY 12304

www.tcrt.org

Technology in Cancer Research and Treatment
ISSN 1533-0346
Volume 10, Number 6, December 2011
©Adenine Press (2011)

Near Infrared Photonic Finger Imager for Prostate Cancer Screening

www.tcrt.org

Y. Pu, Ph.D.[1]
W. B. Wang, Ph.D.[1]*
M. Xu, Ph.D.[2]
G. C. Tang, M.S.[1]
Y. Budansky, M.S.[1]
M. Sharanov, Ph.D.[1]
S. Achilefu, Ph.D.[3]
J. A. Eastham, M.D.[4]
R. R. Alfano, Ph.D.[1]*

[1]Institute for Ultrafast Spectropscopy and Lasers, Department of Physics, City College of the City University of New York, 160 Convent Avenue, New York, NY 10031
[2]Department of Physics, Fairfield University, Connecticut, CT 06824
[3]Washington University School of Medicine, 4525 Scott Avenue, St. Louis, Missouri 63110
[4]Department of Urology, Sidney Kimmel Center for Prostate and Urologic Cancers, Memorial Sloan-Kettering Cancer Center, New York, NY 10065

A portable rectal near infrared (NIR) scanning polarization imaging unit with an optical fiber-based rectal probe, designated as a Photonic Finger (PF), was designed, developed, built and tested. PF was used to image and locate the three dimensional (3D) positions of abnormal prostate tissue embedded inside normal prostate tissue. An inverse image reconstruction algorithm, namely **Op**tical **T**omography using **I**ndependent **C**omponent **A**nalysis (OPTICA) was developed to unmix the signal from targets (cancerous tissue) embedded in a turbid media (normal tissue) in the backscattering imaging geometry. The Photonic Finger combined with OPTICA was *ex vivo* tested to characterize different target(s) inside different tissue medium, including cancerous prostate tissue embedded inside large pieces of normal tissue. This new developed instrument, Photonic Finger, may provide an alternative imaging technique, which is accurate, of high spatial resolution and non-or-less invasive for prostate cancers screening.

Key words: Photonic finger (PF); Backscattering; Scanning optical polarization imaging; Optical fiber-based rectal probe; Three-dimensional localization; Human prostate tissue; Receptor-target contrast agents; Independent component analysis (ICA); Photon propagation model.

Introduction

In year 2010, 217,730 new cases of prostate cancer were diagnosed, and approximately 32,050 men died from prostate cancer in the U.S.A. (1). The common screening tests for prostate cancer diagnosis are digital rectal examination (DRE), measurement of the serum tumor marker namely prostate specific antigen (PSA), and the transrectal ultrasound (TRUS) imaging (2). A value of PSA over 4.0 ng/ml is the commonly used threshold for further diagnostic evaluation (3). Although PSA test appears to have acceptable sensitivity for late stage cancers (4) and disease with histopathologic features associated with tumor progression of a large volume, poorly differentiated cells, and extracapsular penetration (5), its accuracy is limited as low as 28%-35% (6). During the DRE, a doctor inserts a lubricated, gloved finger into the patient's rectum to feel for lumps, enlargements, or hard areas of prostate that might indicate prostate cancer. DRE has a reported sensitivity of 18%-22% (7, 8). TRUS is no longer considered as a first-line screening test for prostate cancer (9) because of its poor spatial resolution and contrast, but it does play a role in mapping the locations of the biopsy sampling (9). The confirmation of prostate cancer finally needs a needle biopsy of the prostate. In the biopsy, a number [12 to 18] of cores of prostate tissue are

---

Abbreviations: Photonic Finger (PF); Independent Component Analysis (ICA); **Op**tical **T**omography using **I**ndependent **C**omponent **A**nalysis (OPTICA).

*Corresponding authors:
W. B. Wang, Ph.D.
R. R. Alfano, Ph.D.
E-mail: wwang@sci.ccny.cuny.edu
ralfano@sci.ccny.cuny.edu

randomly taken from whole region of the prostate using a thin needle with the help of TRUS to map the locations of the sampling (10).

The early detection and treatment of prostate cancers can reduce mortality (11). Conventional oncology imaging methods for prostate cancer diagnosis still depend on bulk physical properties of cancer tissue and are not effective for early-stage primary tumors (12). Since PSA and DRE have limited accuracy, TRUS has poor contrast between normal and abnormal tissue regions, and needle biopsy is invasive and may cause damages of prostate, it is highly desirable to develop a better method which is accurate, of higher spatial resolution and non-or-less invasive for prostate cancer screening.

Optical imaging technique using near infrared (NIR) light provides an attractive noninvasive approach for screening human diseases. The "tissue optical window" in the NIR range, which corresponds to lower absorption from major tissue chromophores such as water, oxygenated and deoxygenated hemoglobin, allows light to penetrate deep into the tissue, up to several centimeters (12). The other main advantages of NIR optical approaches are its inherent low-cost, the ability to monitor multiple independent optical reporters simultaneously *in vivo* based upon wavelength, the absence of radioactive intermediates, and the relative simplicity of the imaging hardware as compared with Magnetic resonance imaging (MRI) and Positron emission tomography (PET) equipment. These advantages make optical imaging unmatched by any other *in vivo* imaging techniques. Over the past decade, Indocyanine Green (ICG, also called cardio-green), a clinically approved NIR dye by FDA, has been investigated as a contrast agent for optical detection of tumors. However, ICG is not designed to specifically target cancer cells. The investigations of receptor expression in normal and cancer tissues suggest that small peptide-dye conjugates can be used to target over-expressed receptors on tumors to enhance specificity (13). Biological studies have indicated that somatostatin receptors (SSTR) are over-expressed in human prostate tumor (14). The previous investigation showed that a small ICG-derivative dye-peptide, namely Cypate-Octreote Peptide Analogue Conjugate (Cytate) could be used for effectively targeting somatostatin receptor-rich tumor in the animal model because of the high affinity of Cytate for the somatostatin receptors (13). This motivates us to apply Cytate in optical scanning imaging in human prostate tissue for cancer detection. The major disadvantage of optical imaging approaches is that strong scattering by biological tissue causes most photons diffused. The very few percentage of ballistic and snake photons make direct imaging practical only in surface and subsurface layers of tissue (15, 16). Scientists have to explore optical tomography methods and/or inverse image reconstruction approaches to locate the three dimension (3D) positions of abnormal tissue or recover the 3D spatial distribution information of optical parameters of the tissue (16).

In this research, a portable rectal NIR scanning polarization imaging unit with an optical fiber-based rectal probe, named Photonic Finger (PF), was developed. The transrectal optical imaging approach was used to locate the 3D positions of abnormal prostate sites hidden in normal prostate tissue based on differences of optical parameters between cancerous and normal prostate tissues. The difference can also be enhanced using an extrinsic chromophore or fluorophore such as a receptor-targeted contrast agent. The rectal NIR scanning polarization imaging and 3D inverse location technique has potential to address the critical issues of the conventional screening methods for prostate cancer detection. The scanning polarization imaging acquires 2D images by sequentially scanning a polarized illuminating light beam at different areas of a prostate gland through rectum, and recording the distribution of light intensity backscattered from the prostate using a CCD camera. An Independent Component Analysis (ICA)-based inverse 3D location reconstruction algorithm was improved specifically for the application of backscattering configuration and used to locate the 3D positions of foreign inhomogeneities from the recorded array of the 2D images. This research provides a noninvasive optical imaging technique for detecting and 3D locating cancerous sites in prostate. Therefore, PF may introduce a new criteria/indicator for prostate cancer screening in addition to the conventional examinations to enhance the accuracy of prostate cancer detection.

Experimental Setup and Methods

Design and Construction of Photonic Finger

The Photonic Finger is a portable rectal NIR scanning polarization imaging unit with an optical fiber-based rectal probe. The unit was designed to be capable of recording sets of 2D images of the prostate by scanning the illuminating beam on the prostate through rectum walls. The major optical and electronic components of the unit include laser diodes and their power supplies, miniature scanning Galvanometric mirrors with their electronic control boards (servo driver circuit boards) and the LabVIEW control software, and illumination and imaging coherent optical fiber-bundles.

A photograph of the portable rectal NIR scanning polarization imaging unit is shown in Figure 1(A). Three diode lasers emitting at 635 nm, 750 nm, and 980 nm, respectively, are alternatively used as light sources. These wavelengths were selected to probe the native molecules such as Hb, HbO_2 and H_2O in tissues. The output beam from a laser diode is directed to the scanning galvanometric mirror system (ThorLab GVSM002 with Dual Axis Galvo Mirrors) after passing through two pinholes and a polarizer (P_1). The beam can be scanned by two miniature galvanometric mirrors in the x- and y-directions, respectively. The beam output from the galvanometric mirrors is focused using a microscopy objective

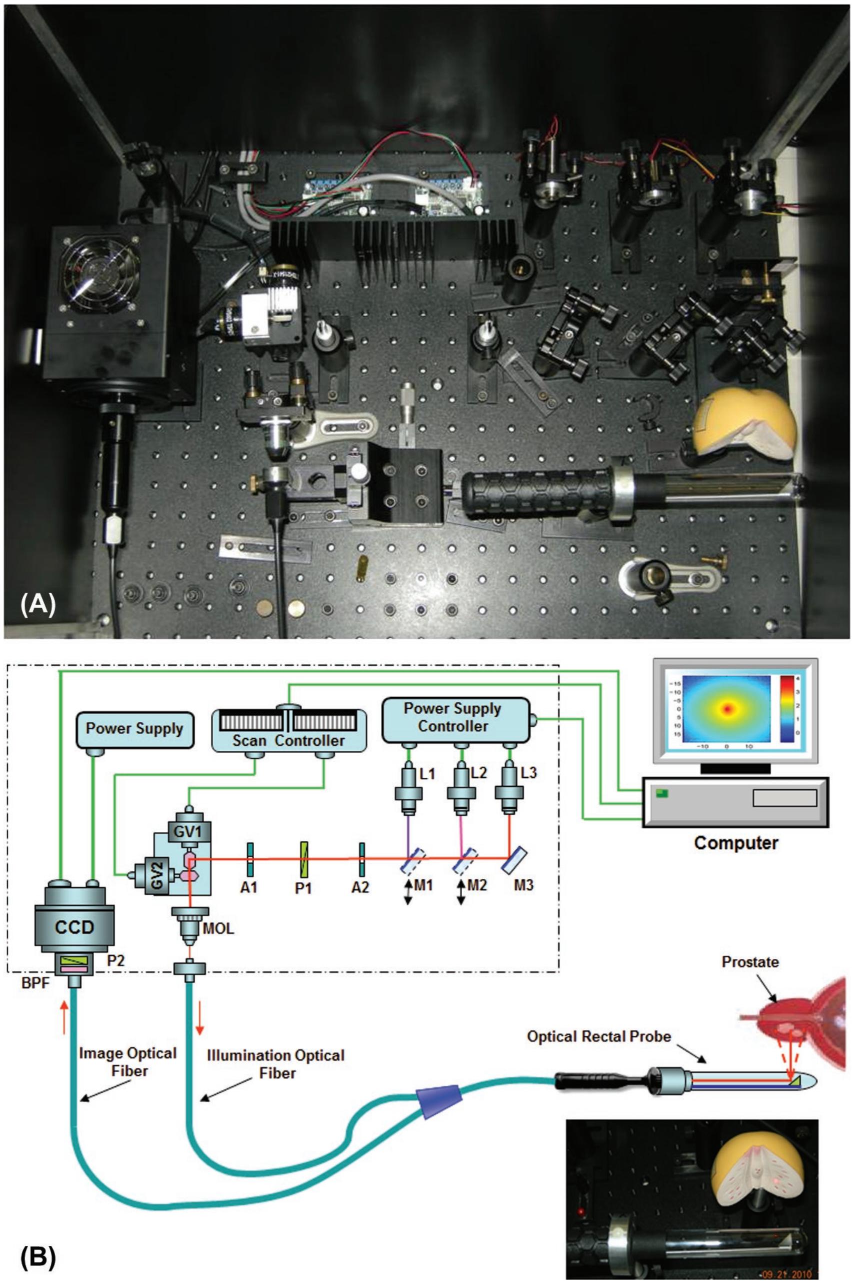

Figure 1: (**A**) A photograph of the Photonic Finger: a portable rectal NIR scanning polarization imaging unit. The power supplies and computer system are not shown in the picture. (**B**) The schematic diagram of the portable rectal NIR scanning polarization imaging unit, where L-laser, M-mirror, A-aperture, P-polarizer, GV-galvanometric scanning mirror, BPF-band pass filter, MOL-microscopy objective lens.

lens on a coherent fiber-bundle (Mytiad Fiber Imaging, 20-0826 Fiberscope Assy) used for illumination. The position of the microscopy objective lens can be adjusted in the *x*-, *y*- and *z*- three directions for the beam-fiber coupling. The output beam from the illumination fiber is directed to a small reflection prism located inside the rectal probe. The beam reflected from the prism is used to illuminate a prostate sample. This illumination beam with a diameter of ~1 mm can be scanned in the *x*- and *y*-directions on the prostate sample.

The light backscattered (or emitted) from a prostate sample is first passing through the rectal wall and reflected from the prism inside the probe head. The diameter of the probe is ~2 cm and the length is ~12 cm. The beam is then collected by a lens into another coherent fiber-bundle (Mytiad Fiber Imaging, 20-0826 Fiberscope Assy) used for imaging. The diameter of a single fiber in the bundle is ~3.2 μm each with numerical aperture N.A. ≅ 0.4. The image information formed in the optical fiber bundle was sent to a CCD camera through the coherent imaging fiber bundle and coupling lens for recording 2D images of the prostate sample. The coupling loss of the system is ~10% and the transverse resolution is 100 μm associated with Air Force resolution target bar chart (AFBC) at group 3. A polarizer (P_2) and a band pass filter are placed in front of the CCD camera to record the 2D images at different polarization configuration and wavelengths. A cross-polarization image for each scanned illumination position of the laser beam is recorded when the polarization direction of P_2 is perpendicular to that of P_1 to suppress the contribution of light scattered (or emitted) from the surface and sub-surfaces to the images of the prostate sample. For the backscattering light imaging, a narrow band filter corresponding to the illumination wavelength is used in front of the CCD camera to ensure that the recorded images are formed only by the light backscattered from the prostate sample. For the tissue emission and/or contrast agent emission light imaging, a long pass filter is used in front of the CCD camera to ensure that the recorded images are formed only by the light emitted from the prostate sample. When the illumination light beam is scanned in the x-y plane of the sample with $n \times n$ points, an array of n^2 2D images will be recorded.

The key part of the scanning imaging unit is the scan of the illumination beam on the surface of the prostate sample with adjustable scanning parameters such as scanning area, step, speed and the number of scanning points. Figure 1(B) schematically shows the layout of the major parts and the control boards for the PF unit. This scanning system consists of (1) the Dual Axis Galvo mirrors (ThorLab GVS 002), (2) the two servo driver circuit boards and their power supply (ThorLab, GPS011), (3) the drive unit for sending voltage output to servo circuit boards (National Instruments, NI DAQmx USB-9263 USB DAQ - data acquisition), and (4) a PC with an installed LabVIEW software (LabVIEW Signal Express 2009) to power and send a command to DAQ USB 9263 to generate desired output voltage through a USB connection. In the scanning system, the drive unit NI-9263 powered by USB interface of the PC, is used to generate an analog voltage, which can be varied from −10 V to +10 V using the LabVIEW software. This analog voltage is sent to the two servo driver boards to drive the rotations of the Galvo Mirrors. For example, 1V input to the servo board can make the mirror rotate 1^o. One servo board controls the X-axis, and another is for Y-axis. Both servo driver boards are powered by the power supply of GPS011. The beam scanning, the image acquiring and recording, and the synchronization of scanning and imaging are controlled by the Graphical User Interface (GUI) software developed using LabVIEW. Figure 2 shows a screenshot of the GUI after completing an $n \times n$ scan. All parameters of the scanning imaging unit (the position of the original, scanning steps, step size, exposure time, and waiting time between two adjacent imaging acquiring), can be adjusted through the GUI.

Test Samples

The Photonic Finger scanning imaging unit was tested for different types of tissue samples. The first sample used for scanning imaging was a black rubber absorber with the size of ~2.7 mm × ~3.0 mm × ~1.5 mm embedded in chicken breast tissue at different depth. The fresh chicken breast tissues were purchased at the local super market. The black rubber was covered by the chicken breast tissues at two different depths of ~5.1 mm and ~6.6 mm with a lateral dimension 38 mm × 29 mm for scanning imaging measurements. The thickness of the tissue behind the object is ~8 mm. A transport length $l_t = 1.1$ mm and an absorption coefficient $\mu_a = 0.007\,\text{mm}^{-1}$ were taken for chicken breast tissue for imaging analysis (17).

The second study was performed to distinguish *in vitro* cancerous prostate tissue from surrounding normal prostate tissue. Human prostate tissues were obtained from the Cooperation Human Tissue Network (CHTN) and the National Disease Research Interchange (NDRI) under the approval of the Institutional Review Board (IRB) at CCNY. The cancerous and normal prostate samples were diagnosed by pathologist before the optical imaging experiments. Samples were neither chemically treated nor were frozen prior to the experiments. The time elapsed between tissue resection and taking the scanning imaging measurements may vary for different sample sources. The longest elapsed time is about 30 hours. The sample consists of a small piece of cancerous prostate tissue (4 mm × 4 mm × 1.5 mm) embedded inside a large piece of normal prostate tissue at the depth of $z = 3.0$ mm from the front surface. The thickness of the whole tissue sample is 10 mm. For imaging analysis, the absorption and reduced scattering coefficients for normal prostate tissue (the host medium) were taken as $\mu_a \approx 0.026\,\text{mm}^{-1}$ and $\mu_s' \approx 0.53\,\text{mm}^{-1}$. The cancerous prostate tissue absorbs much less light with $\mu_a \approx 0.0025\,\text{mm}^{-1}$ and scatters less with $\mu_s' \approx 0.44\,\text{mm}^{-1}$ at the probing wavelength of 635 nm estimated from our earlier spectroscopic investigations of *ex vivo* prostate tissues (18). The piece of cancerous prostate tissue embedded behaves predominantly as an absorption inhomogeneity in homogeneous normal prostate tissue. Here, we simply assume that the optical parameters of normal tissue are macroscopically homogeneous throughout the tissue volume. Although this is not a rigorous description of tissue, for many cases of interest, it will be sufficient. OPTICA is applied here to extract different independent components by treating cancerous tissue as inhomogeneity embedded inside a "homogeneous" normal tissues.

The third study was designed to characterize cancerous prostate tissue after enhancing imaging contrast by extrinsic fluorescent marker, a receptor-targeted contrast agent, namely Cytate. Cytate was synthesized by Achilefu's group at the Washington

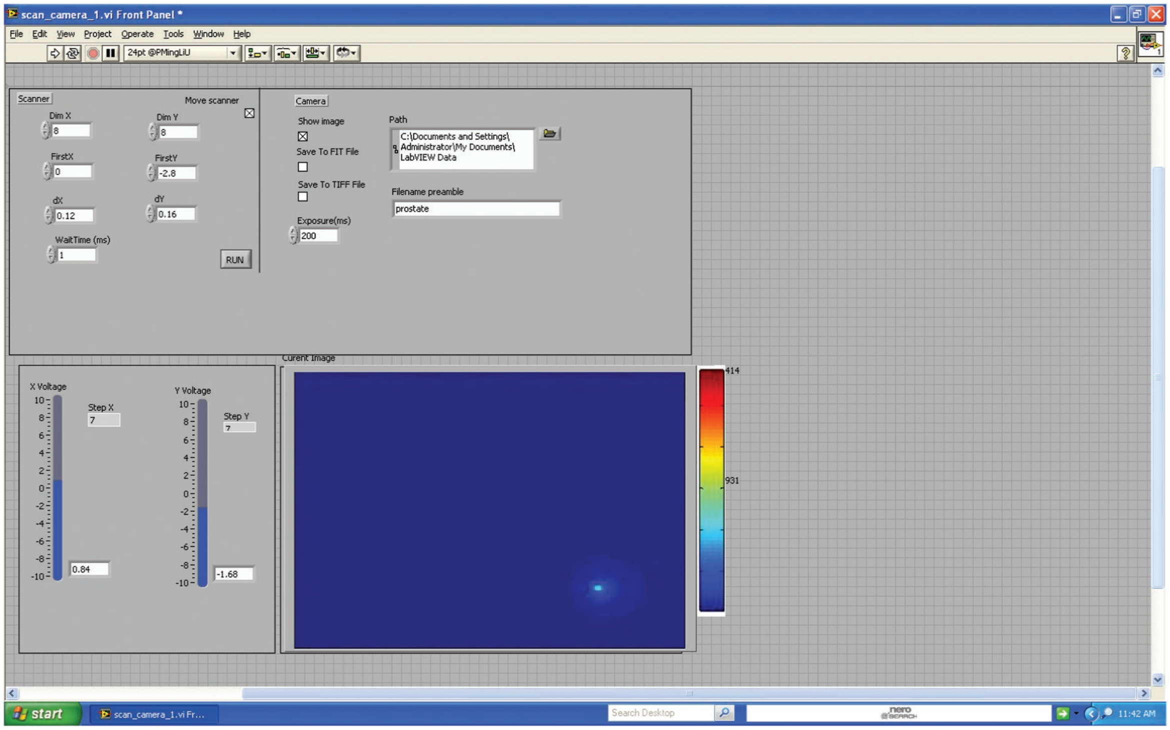

Move scanner ☒

Dim X 8

Dim Y 8

FirstX 0

FirstY -2.8

dX 0.12

dY 0.16

WaitTime (ms) 1

Show image ☒

Save To FIT File ☐

Save To TIFF File ☐

Exposure(ms) 200

Path C:\Documents and Settings\Administrator\My Documents\LabVIEW Data

Filename preamble prostate

Step X 7

Step Y 7

X Voltage 0.84

Y Voltage -1.68

Figure 2: A screenshot of the Graphical User Interface (GUI) after completing an $n \times n$ scan. The GUI was developed using LabVIEW for operation of the Photonic Finger. All parameters of the scanning imaging (the position of the original, scanning steps, step size, exposure time, and waiting time between two adjacent imaging acquiring, *e.g.*) can be adjusted through the GUI.

University School of Medicine. This contrast agent is mainly composed of ICG and the somatostatin receptor ligand, which delivers ICG to the corresponding somatostatin receptors over-expressed in the tumor (13, 14). The prostate tissue samples for the scanning imaging study were prepared following this protocol: (1) samples (cancerous and normal prostate tissues) were cut into very tiny size, which is less than ~1 mm (in length, width and thickness) pieces. Each pair of cancerous tissue and the corresponding normal tissue used as a control sample was obtained from same patient; (2) both small pieces of prostate tissue samples were soaked in a same Cytate solution with a concentration of ~3.2×10^{-6} M for ~10 minutes; (3) Cytate-stained tissue samples were put into sodium phosphate buffer (Sigma-Aldrich) to wash off and consequently reduce the amount of un-bound Cytate (19); and (4) the Cytate-stained small pieces of cancerous and normal prostate tissues were covered by a large piece of normal prostate tissue at two different depths of ~2.5 mm and ~3.7 mm for scanning imaging measurements.

The orthogonal co-ordinate system to locate 3D positions of the target in the scanning polarized image measurements is schematically shown in Figure 3. The samples to be tested were embedded inside large slices of host tissue at different depths. The illuminating laser beam was scanned along the *x*- and *y*-directions on the front surface of the sample. The 2D images formed by the light backscattered from the sample in the normal direction are recorded. In the first and second studies, only one target (black rubber or cancerous prostate tissue) is involved in each case and the sample was illuminated by a collimated laser beam with $\lambda = 635$ nm. The elastic backscattering from the samples was collected through a narrow band filter (NF). In the third study for contrast agents' fluorescence, the Cytate-stained tiny cancerous and normal prostate tissue samples were embedded inside large pieces of normal prostate tissue. The sample was illuminated by a laser beam with $\lambda = 635$ nm in the direction close to the normal to the surface. A narrow band-pass filter at 830 nm was placed in front of a CCD camera to record emission images based on the emission peak of Cytate at ~837 nm (20).

Algorithm of OPTICA

The theory of **Op**tical **T**omography using **I**ndependent **C**omponent **A**nalysis (OPTICA) method was described in elsewhere (21). ICA, the core of OPTICA, is a solution to the *blind source separation* problems, which is a class of the problems that no precise knowledge is available on neither the mixing channels nor the sources. Typically the observations are the output of a set of sensors, where each sensor receives a set of mixed source signals (21). The algorithm of OPTICA is based on that ICA of the perturbations in the spatial intensity distributions provides the corresponding independent intensity

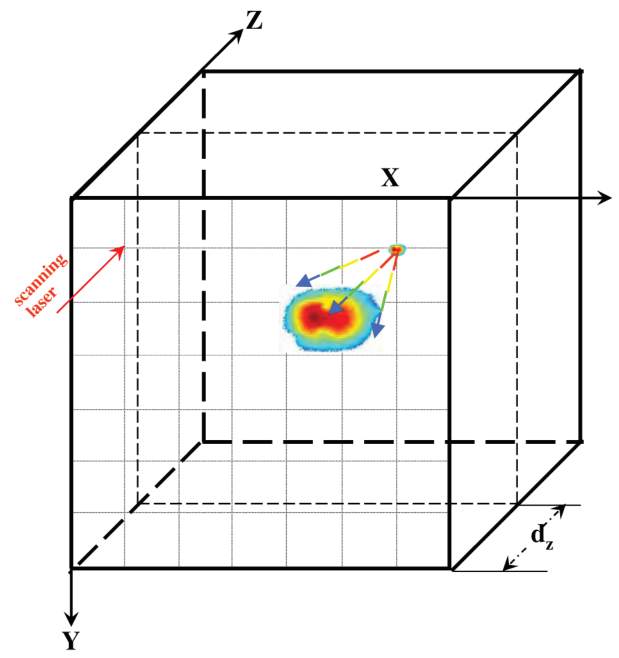

Figure 3: The schematical diagram that displays our calculated position of objects in an orthogonal co-ordinate system to locate 3D positions of the target using the scanning polarized image unit.

distributions (IID) on the detector planes (21). The measured array image is given by (16):

$$I(\rho_d, \rho_s) = I_0 G_0(\boldsymbol{r}_d, \boldsymbol{r}_s) - I_0 \Delta z \int G_0(\boldsymbol{r}_d; \rho', z')\,\delta\mu_a(\rho', z')\, G_0(\rho', z'; \boldsymbol{r}_s)\, d^2\rho' \quad [1]$$

where ρ_d covers the whole 2D array, ρ_s is the scanning positions of incident light source with the intensity of I_0 at the $z = 0$ plane, G_0 denotes the exact Green's function for light propagation in the host medium. It is assumed that one tiny object (with absorptive perturbation $\delta\mu_a$ of volume ΔV) is located at $r' = (\rho', z')$ with the extension $\Delta z \ll 1$ along the axial direction and that $\delta\mu_a$ is constant within ΔV. The speed of light is set to be unity. Scattering targets can be treated in a similar fashion.

The background image could be approximately generated using an "average" image of all acquired images by shifting the scanning position for each image ρ_s to the origin 0, which is given by (16):

$$\bar{I}(\rho_d, 0) = I_0 G_0(r_d, 0) - h(\rho_d, 0) \quad [2]$$

where the term h stands for the error term. This "averaged" background image is called "dirty" background image since the object(s) with $\delta\mu_s$ and $\delta\mu_s$ is included in the averaging calculation. To generate a "clean" background image, the shifted images which are minimally perturbed by the embedded objects were selected and averaged (16):

$$\bar{I}_c = \bar{I}(\rho_d, 0) + h(\rho_d, 0) \quad [3]$$

where the error term is chosen by:

$$h(\rho_d - \rho_s, 0) = \frac{1}{N_B} \sum_{\rho_s \in B} \Delta I(\rho_d - \rho_s, 0) \quad [4]$$

where B denotes the perimeter of the scanning grid which contains N_B scanning positions. After h and the clean image of the host medium have been obtained, the difference images are calculated more accurately (16) since the cleaning imaging suppresses the contributions from embedded objects (cancerous tissues) to simulate a more "homogeneous" background.

The difference images were then generated by subtracting the "clean" background image from the recorded 2D images. Based on the difference images, ICA was used to unmix the signal arising from individual targets and the independent intensity distribution due to the target(s). Each target is associated with one independent component (IC), which consists of the projection of the Green's functions, $G_0(\boldsymbol{r}_s, \boldsymbol{r}_t)$ and $G_0(\boldsymbol{r}_d, \boldsymbol{r}_t)$, on the source or detector plane, respectively (21). The position of the target is obtained by numerically marching the target(s) to the surface until matching the retrieved independent component, incorporating both the beam profile and the surface property of the sample (14). The 3D locations of a black rubber hidden inside chicken breast tissue medium, and 3D locations of a small piece of cancerous prostate tissue embedded in the host normal prostate tissue were used to verify our new OPTICA algorithm using the recorded sets of 2D backscattering images. The procedures of OPTICA for obtaining 3D locations of objects in scattering media are listed in Table I.

Table I

Steps of OPTICA to locate 3D position of target(s) inside scattering medium at backscattering configuration.

1. Record a set of images with embedded inhomogeneities at different illuminated scanning positions;
2. Generate a "clean" background image from the "dirty" background image produced by selecting and averaging the minimally perturbed images;
3. Calculate the difference images between the recorded images and the "clean" background image;
4. Do ICA analysis of the set of difference images to generate the Independent Components (ICs);
5. Obtain the contribution of each target to intensity distribution;
6. Estimate 3D location of the target relative to boundaries by numerically marching the target to the surface until matching the retrieved IC.

Experimental Results

To illustrate the procedures and improvement of OPTICA using PF particularly developed for backscattering geometry, a set of scanning optical polarized images of a small piece of cancerous prostate tissue embedded in normal prostate tissue were acquired by the Photonic Finger. Figure 4 shows the typical scanning images chosen from the total 8 × 8 polarized images recorded by scanning the incident beam on the *x-y* plane of the sample. The images shown on the four corners [images (1, 1), (1, 8), (8, 1), (8, 8)] are chosen by the *x-y* positions of the incident light far from the embedded object while other images in the central area [images (3, 5), (3, 6), (4, 5), (4, 6)] are chosen by the *x-y* positions of the incident light close to the embedded cancerous tissue. There is no big difference of the light intensity distribution pattern among these recorded images except the position at the maximum intensity. This is because of the sharp peak of light intensity scattered from the surface and subsurface in the backscattered direction (16), which suppresses the perturbation caused by $\delta\mu_a$ and/or $\delta\mu_s'$ from the embedded cancerous tissue. To overcome this difficulty, a "clean" background image (CBI) needs to be synthesized. In "clean" background image synthesis, the incident light position of each of 8 × 8 images is set to origin. All array images are then shifted to the origin and the size of each image is cropped at the boundary while incident light distribution reaches the noise level. The images minimally perturbed by the embedded targets are selected for synthesizing the "clean" image.

After the "clean" background image is obtained, the perturbation 2D (*x-y*) images are generated by extracting the "clean" background image from the recorded images. In the perturbation 2D images, the perturbation caused by the embedded cancerous tissue was highlighted. ICA is then performed upon the perturbation images to recognize leading independent components (ICs). Each target is associated with one independent component (IC). As an example, Figure 5 shows the OPTICA-generated independent intensity distributions of a cancerous prostate tissue embedded in normal prostate tissue. Figure 5(A) is for the leading independent component, and Figure 5(B) is for residual (noise) component. It is clear that the existence of target (the cancerous prostate tissue) can be discerned from Figure 5(A). The *x*- and *y*-locations of the cancer tissue can be obtained from the position of maximum intensity of Figure 5(A). The signal strength of Figure 5(A) is much stronger than that of Figure 5(B), indicating

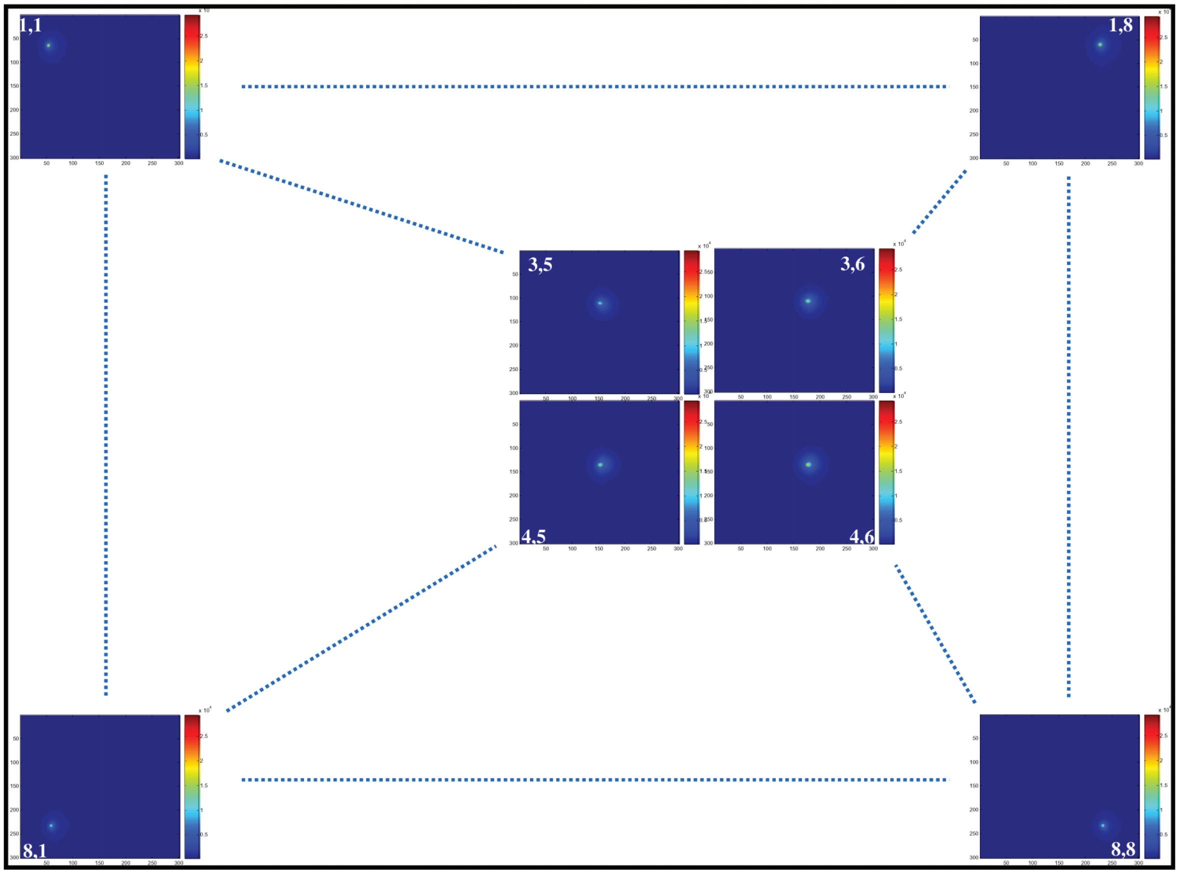

Figure 4: A set of 64 (8 × 8) images recorded by scanning the incident beam on the *x-y* plane of the sample (a small piece of cancerous prostate tissue hidden in the host normal tissue).

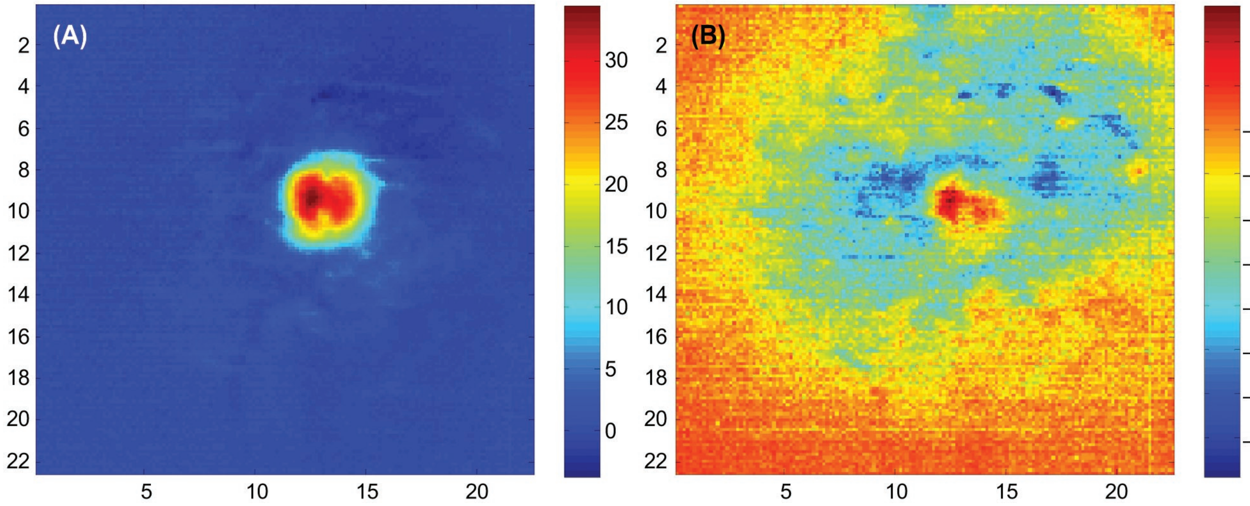

Figure 5: OPTICA-generated intensity distributions of the independent components on the detector plane for the sample consisting of a small piece of cancerous prostate tissue embedded in normal prostate tissues. (**A**) is the leading IC; and (**B**) is the residual (noise) component.

independent intensity distribution in Figure 5(A) generated by OPTICA is the leading IC. The OPTICA-generated intensity distributions of the leading independent component(s) on the detector plane can be used to locate the z-position of the cancerous tissue by numerical matching the target to the surface of the medium until matching the retrieved IC. (14). The result of $z = 3.1$ mm obtained from OPTICA analysis is in good agreement with the actual depth of ~3 mm.

The OPTICA-generated independent components using data of the scanning fluorescent images of Cytate-stained cancerous and normal prostate tissues embedded in large normal prostate tissue are shown in Figures 6(A) to 6(F). Figure (A) and (B) show the first leading IC standing for Cytate-stained cancerous tissue location; (C) and (D) show the second IC indicating Cytate-stained normal tissue location; (E) and (F) show residual – noise. The 3D locations of the Cytate-stained cancerous prostate tissues were obtained using similar methods described above.

OPTICA-generated results are summarized in Table II under different conditions using backscattering polarized imaging and OPTICA, which lists the OPTICA-determined positions of different objects in the different experiments mentioned above in comparison with their known 3D locations.

Another salient feature shown in Figure 6 is the higher emission intensity of the stained cancerous tissue compared to the stained normal tissue. This is attributed to the preferential uptake of Cytate by cancerous prostate tissue (12, 17-19). Using the data shown in Figure 6, the ratio of I_c/I_n after OPTICA analysis was found to be ~3.9 and ~2.3, for the samples with depths of 2.5 mm and 3.5 mm, respectively.

Discussion

Prostate cancer is classified as an adenocarcinoma, or glandular cancer which is developed from epithelial cells (22). About 70% of prostate cancer arises in the peripheral zone (22). The mean mucosa thickness of 830 ± 60 μm and the mean rectal wall thickness of 2.57 ± 0.15 mm (22, 23) allows the NIR scanning laser beam to penetrate the rectal wall to reach prostate for optical imaging through rectum (12, 24). By employing scanning NIR imaging, Photonic Finger can be used to characterize cancerous prostate tissue up to ~3 mm

Table II
Comparison of the known and OPTICA determined positions of embedded objects.

Object	Covered tissue	Known (x, y, z) position (mm)	OPTICA-generated (x, y, z) position (mm)
Cancerous prostate tissue	Normal prostate tissue	(13.5, 10.1, 3.0)	(13.8, 10.3, 3.1)
Stained cancerous tissue	Normal prostate tissue	(17.8, 14.6, 2.5)	(17.9, 14.4, 2.3)
Stained cancerous tissue	Normal prostate tissue	(18, 24, 3.5)	(17.6, 23.8, 3.6)
Black rubber	Chicken tissue	(15.6, 10.4, 5.1)	(15.2, 10.2, 4.7)
Black rubber	Chicken tissue	(15.6, 10.4, 6.6)	(15.3, 10.8, 6.2)

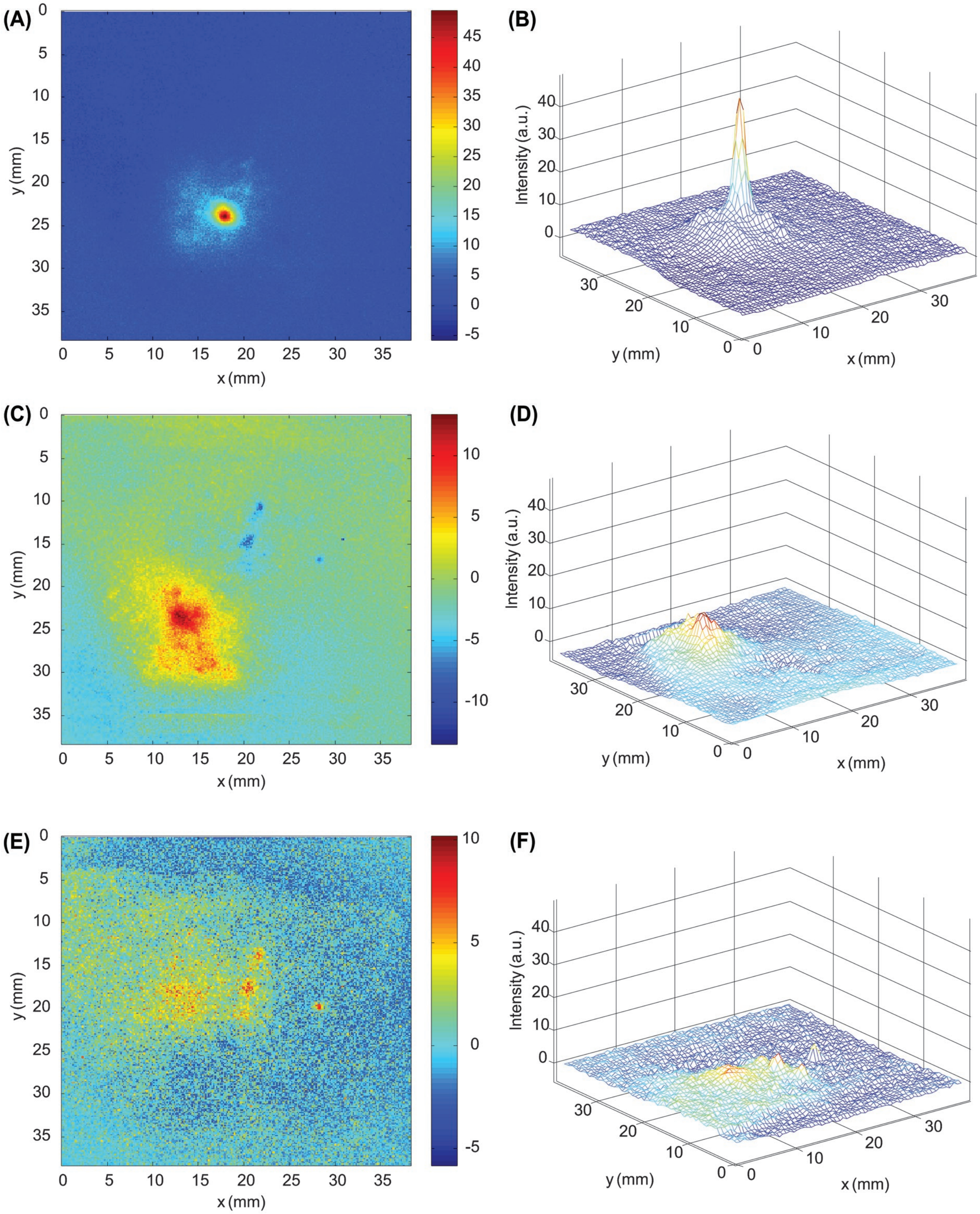

Figure 6: OPTICA-generated intensity distributions of the independent components on the detector plane for the sample consisting of the Cytate-stained cancerous and normal prostate tissues embedded in normal prostate tissue. (**A**) and (**B**) show the first leading IC indicating for Cytate-stained cancerous prostate tissue; (**C**) and (**D**) show the second leading IC standing for Cytate-stained normal prostate tissue; and (**E**) and (**F**) show the residual (noise) component.

without contrast agents. With the enhancement of the receptor-target contrast agent, PF can detect cancer at much deeper tissue layer. Previous spectral polarized imaging experiments performed in IUSL show that ICG-stained small object hidden inside the host prostate tissues in the rectum-membrane-prostate structures at depths of 7.5 mm can be imaged and identified using fluorescence imaging methods (25). ICG is the fluorescent part of Cytate. It is reasonable to assume that PF can detect cancer in deep prostate tissue layer more than 7.5 mm under optimal condition with the enhancement of the receptor-target contrast agent. The PF will achieve diagnostic function as a screening tool other than TRUS. It is well known that TRUS alone cannot be considered as a screening tool for prostate cancer detection (9). It is used as location map when numbers of biopsy samples were taken randomly from the prostate using biopsy needles of ~1.2 millimeters in diameter (25). The number of biopsies that should be performed is debated. Twelve or eighteen biopsies suggested by different protocols were reported (22). The oversampling and overtreatment of prostate cancer is now a great concerning in prostate cancer research (22, 25) not only because of the increased numbers of sampling will cause bleeding and pain, but also because the penetration and bleeding may cause the metastasis of prostate cancer to other organ (22, 25). In contrast to TRUS, Photonic Finger can locate the 3D positions of cancerous prostate sites. Therefore, it may function as a detecting and screening instrument. Photonic Finger, an optical scanning imaging system may have positive impact in clinic applications to reduce significant pain and amount of bleeding for patients in prostate cancer detection.

Conclusion

In conclusion, a portable rectal NIR scanning polarization imaging unit with an optical fiber-based rectal probe, named Photonic Finger, was designed, developed, assembled and tested on *ex vivo* tissues at IUSL in CCNY. This instrument combined with OPTICA was achieved to characterize and 3D-locate cancerous prostate tissue embedded in normal prostate tissue in backscattered geometry for the first time. The retrieved 3D locations are in good agreement with the known position of the embedded object. This technique was able to sense weak/small absorptive, scattering, or fluorescent inhomogeneities. This new developed Photonic Finger instrument may provide an alternative imaging technique for prostate cancer detection, which is accurate, of higher spatial resolution and non-or-less invasive, and can be applied in near-real-time for *in-vivo* detection.

Acknowledgement

This research is supported by U. S. Army Medical Research and Material Command (USAMRMC) grant of W81XWH-08-1-0717(CUNY RF # 47170-00-01). Y. Pu acknowledges additional support from the USAMRMC grant of W81XWH-11-1-0335 (CUNY RF # 47204-00-01), and M. Xu acknowledges additional support from USAMRMC grant of W81XWH-10-1-0526 and NIH (1R15EB009224). The authors acknowledge the help of CHTN and NDRI for providing normal and cancerous prostate tissue samples for the measurements.

Reference

1. American Cancer Society, Cancer Facts & Figures 2010, *Atlanta: American Cancer Society* (2010).
2. Abrahamsson, A., Bostwick, D. The biological nature of prostate cancer – a basis for new treatment approaches. http://www.urologi.org/sota/STA026/sta26app.pdf
3. Optenberg, S. A., Thompson, I. M. Economics of screening for carcinoma of the prostate. *Ural Clin North Am 17*, 719-737 (1990).
4. Gann, P. H., Hennekens, C. H., Stampfer, M. J. A prospective evaluation of plasma prostate-specific antigen for detection of prostate cancer. *JAMA 263*, 289-294 (1995).
5. Mettlin, C., Mruphy, G. P., Lee, F., *et al.* Characteristics of prostate cancer detected in the American Cancer Society National Prostate Cancer Detection Project. *J Urol 152*, 1737-1740 (1994).
6. Catalona, W. J., Smith, D. S., Ratliff, T. L., Dodds, K. M., Coplen, D. E., Yuan, J. J., Petros, J. A., Andriole, G. L. Measurement of prostate specific antigen in serum as a screening test for prostate cancer. *N Engl J Med 324*, 1156-1161 (1991).
7. Catalona, W. J., Richie, J. P., Ahmann, F. R., *et al.* Comparison of digital rectal examination and serum prostate specific antigen in the early detection of prostate cancer: results of a multi-center clinical trial of 6,630 men. *J Urol 151*, 1283-1290 (1994).
8. Vihko, P., Kontturi, O., Ervast, J., *et al.* Screening for carcinoma of the prostate: rectal examination and enzymatic radioimmunologic measurements of serum acid phosphatase compared. *Cancer 56*, 173-177 (1985).
9. Ferrini, R., Woolf, S. H. Screening For Prostate Cancer in American Men. http://www.acpm.org/prostate.htm, *American College of Preventive Medicine – Practice Policy Statement.*
10. Tindall, D. J., Scardino, P. T. Defeating prostate cancer: Crucial direction for research — except from the report of the Prostate Cancer Progress Review Group (Review). *Prostate 38*, 166-171 (1999).
11. Catalona, W. J., Smith, D. S., Ratliff, T. L., Basler, J. W. Detection of organ-confined prostate cancer is increased through use of prostate-specific antigen-based screening. *JAMA 270*, 948 (1993).
12. Pu, Y., Wang, W. B., Tang, G. C., Zeng, F., Achilefu, S., Vitenson, J. H., Sawczuk, I., Peters, S., Lombardo, J. M., Alfano, R. R. Spectral polarization imaging of human prostate cancer tissue using a near-infrared receptor-targeted contrast agent, *Technol Cancer Res Treat 4*, 429-436 (2005).
13. Achilefu, S., Dorshow, R. B., Bugaj, J. E., Rajagopalan, R. Novel receptor-targeted fluorescence contrast agent for *in vivo* tumor imaging. *Investigative Radiology 35*, 479-485 (2000).
14. Hansson, J,, Bjartell, A., Gadaleanu, V., Dizeyi, N., Abrahamsson, P. A. Expression of somatostatin receptor subtypes 2 and 4 in human benign prostatic hyperplasia and prostatic cancer. *Prostate 53*, 50-59 (2002).
15. Wang, L., Ho, P. P., Liu, C., Zhang, G., Alfano, R. R. Ballistic 2-D imaging through scattering wall using an ultrafast Kerr gate. *Science 253*, 769-771 (1991).
16. Pu, Y., Wang, W. B., Tang, G. C., Budansky, Y., Alfano, R. R., Xu, M. Backscattering scanning optical imaging with independent component analysis: three-dimensional localization of objects in tissue., *Proceedings of SPIE 7895*, pp. 78950K-1-5 (2011), in the "Optical Biopsy IX", BO206, edited by R. R. Alfano and Stavros G. Demos.
17. Cheong, W. F., Prahl, S. A., Welch, A. J. A review of the optical properties of biological tissues. *IEEE J Quantum Electron 26*, 2166-2185 (1990).
18. Pu, Y. Fractal dimensional parameters and optical coefficients of cancerous and normal prostate tissues. A dissertation thesis of the City University of New York, Chapter 3, 48-76 (2010).
19. Pu, Y., Wang, W. B., Das, B. B., Achilefu, S., Alfano, R. R. Time-resolved fluorescence polarization dynamics and optical Imaging of Cytate: a prostate cancer receptor-targeted contrast agent. *Applied Optics 47*, 2281-2289 (2008).

20. Pu, Y., Wang, W. B., Achilefu, S., Alfano, R. R. Study of rotational dynamics of receptor-targeted contrast agents in cancerous and normal prostate tissues using time-resolved picosecond emission spectroscopy. *Applied Optics 50*, 1312-1322 (2011).
21. Xu, M., Alrubaiee, M., Gayen, S. K., Alfano, R. R. Optical imaging of turbid media using independent component analysis: theory and simulation. *J Biomed Opt 10(5)*, 051705-1-12 (2005).
22. Theodorescu, D., Krupski, T. L. Prostate cancer – biology, diagnosis, pathology, staging, and natural history. http://emedicine.medscape.com/article/458011-overview, May 21 (2009).
23. Huh, C. H., Bhutani, M. S., Farfan, E. B., Bolch, W. E. Individual variations in mucosa and total wall thickness in the stomach and rectum assessed via endoscopic ultrasound. *Physiol Meas 24*, N15-N22 (2003).
24. Wang, W. B., Ali, J. H., Alfano, R. R., Vitenson, J. H., Lombardo, J. M. Spectral polarization imaging of human rectum-membrane-prostate tissues. *IEEE Journal of Selected Topics in Quantum Electronics 9*, 288-293 (2003).
25. Dr. Tom. Urologist. "Men's Prostate Biopsy", http://www.articlesbase.com/advertising-articles/men039s-prostate-biopsy-1925566.html

Received: June 14, 2011; Revised: August 15, 2011;
Accepted: August 24, 2011

Appendix 5

A paper entitled “Chemotherapeutic Effects on Breast Malignant Cells Evaluated by Native Fluorescence Spectroscopy”, by Yang Pu, Guichen Tang, Wubao Wang, H. E. Savage, S. P. Schantz, and Robert R. Alfano, published in *Biomedical Optics (BIOMED)/ Digital Holography and Three-Dimensional Imaging (DH)*, JM3A45-1-3 (2012).

Chemotherapeutic Effects on Breast Malignant Cells Evaluated by Native Fluorescence Spectroscopy

Yang Pu[a], G. C. Tang[a], W. B. Wang[a] , H. E. Savage[b], S. P. Schantz[b], and R. R. Alfano[a*]

[a]*Institute for Ultrafast Spectroscopy and Lasers, and Department of physics of The City College of the City University of New York, Convent Avenue at 138th Street, New York, NY 10031*
[b]*Department of Surgery of Memorial Sloan-Kettering Cancer Center, New York, NY 10021 and Department of Otolaryngology, Head, Division of Head and Neck Surgery, Manhattan Eye, Ear & Throat Hospital, New York, NY 10003*
** The corresponding author: R. R. Alfano may be reached by email at alfano@sci.ccny.cuny.edu*

Abstract: The decreasing relative content of tryptophan, NADH and flavin of the retinoic acid-treated breast cancerous cells were demonstrated using native fluorescence spectra. The changes may be used to evaluate the chemotherapeutic effects on cancer.

OCIS codes: 170.0170, 170.4580, 170.6280

1. Introduction

Optical spectroscopy has been considered as an alternative technique for cancer detection since Alfano and coworkers were the first to measure native fluorescence spectra of malignant breast tissues [1]. The aim of this present research is to determine if the native fluorescence spectroscopy is effective enough to detect changes of fluorophore compositions related to the treatment of chemotherapy on malignant cell lines using Nonnegative Matrix Factorization (NMF) analysis.

2. Samples and Methods

The human breast cells were purchased from American Type of Culture Collection (ATCC), Rockville, MD. The cell lines used in the study were: malignant human breast cell lines ATCC HTB22 (Adenocarinoma Pleural Effusion) and ATCC HTB126 (Dutal Carcinoma). The cells were cultured with 90% modified Dulbeco's minimal essential medium (Eagle) (GIBO) and 10% of the fetal bovine serum (GIBCO) in a humidified atmosphere of 4% CO_2 at 37^oC. Half of the cells were treated with ~10^{-6} M retinoic acid and the remainder served as controls while the cell lines are cultured. The measured cell concentration was estimated as ~$105 - 110 \times 10^6$ cells/ml.

The fluorescence emission spectra of cells were measured using Perkin-Elmer LS 50 spectrometer. The excitation wavelengths of 300nm and 340 nm were selected based on our previous spectral study of the main fluorophores in breast cells [2]. Combined with NMF, the native fluorescence measurements were used to distinguish the RA-treated breast cancer cells from the untreated cell. The main advantage of NMF is that the NMF-recovered spectral data and concentrations of constituents are positive values. This makes the calculated results represent more physically and/or biologically meaning because the spectra and contents of the fluorephores should have non-negative values.

3. Experimental results and discussion

Fourteen pairs of the RA-treated and untreated breast cancer cell samples were investigated using fluorescence spectroscopy with excitation wavelength of 300 nm. The average fluorescence spectral profiles with standard deviation error bars at key wavelengths for the RA-untreated and treated cancerous breast cells are shown in Figs. 1(a) and 1(b), respectively. Each spectral profile was normalized to unit value of 1 (i.e., the sum of squares of the elements in each emission spectra data was set as 1) before taking average and calculation.

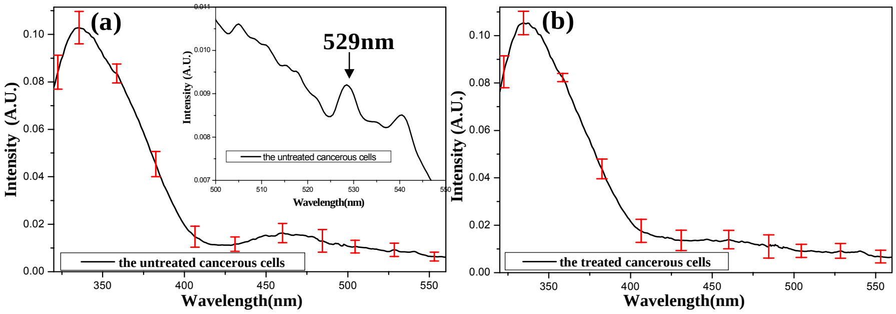

Fig. 1 Average fluorescence spectra of (a) untreated and (b) Retinoic Acid (RA)-treated cancerous breast cells obtained with the excitation of 300 nm.

The main emission peaks of both untreated and treated cancerous breast cells were found at 337nm. The major difference of the fluorescence profiles between the untreated and treated cells is that there exists a much lower local peak at ~ 460nm for the untreated cells while no such a peak for the treated cells. A tiny local peak at 529 nm may be observed in the emission of the untreated cells, which can be more clearly seen by enlarging the fluorescence profile at the spectral range of 700 nm to 900 nm as shown in insert of Fig. 1 (a).

To investigate the relative content changes of Principal Components (PCs) and compare with their corresponding fluorophores, NMF was used to extract spectra of PCs (fluorophores) of the 1st component (tryptophan), the 2nd (NADH) and the 3rd (flavin) for the cells, which are shown as dash, dot and dash-dot lines in Fig. 2(a), respectively. The measured spectra of individual tryptophan, NADH and flavin in solutions are plotted as thicker, thick and thin solid lines, respectively, as references. The two groups of spectra (the extracted and the measured) for each fluorophore show reasonable agreement, which demonstrates that NMF model accounts for the major spectroscopic feature observed, and indicates that the measurements are reasonable [2].

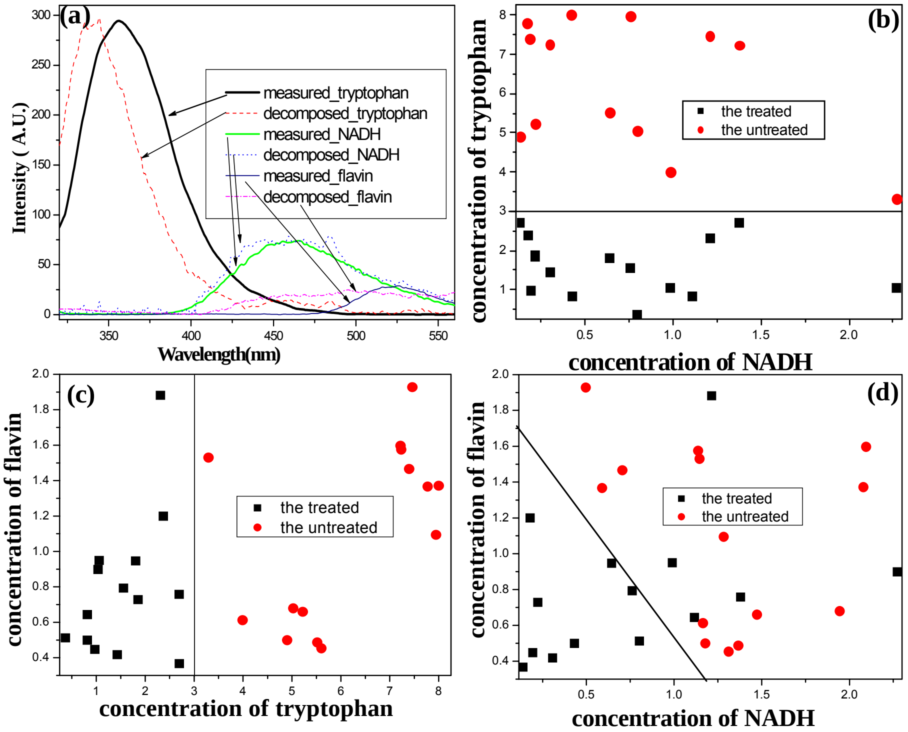

Fig. 2 (a) Comparison of the extracted spectra of the three principal components (PCs) of the 1st PC – tryptophan (dash line), 2nd PC – NADH (dot line) and 3rd PC – flavin (dash-dot line) for the untreated and treated breast cancerous cells, and the measured spectra of individual tryptophan (thicker line), NADH (thick line) and flavin (thin line) in solution; (b) Fractional content of the 1st PC - tryptophan vs. that of the 2nd PC - NADH; (c) Fractional content of the 3rd PC - flavin vs. that of the 1st PC - tryptophan; (d) Fractional content of the 3rd PC - flavin vs. that of the 2nd PC - NADH by analyzing emission spectra excited at 300 nm using NMF method. The data for the untreated and treated cells are displayed with the solid circles and solid squares in 2 (b) – 2 (d), respectively.

To investigate the relative content changes of PCs, the contents of tryptophan, NADH and flavin in two types of cells were extracted from the measured total fluorescence spectra using the NMF analysis. Fig. 2(b) shows the relative content of the 1st PC (tryptophan) vs. the 2nd PC (NADH); 2(c) displays the 3rd PC (flavin) vs. the 1st PC (tryptophan) and 2(d) exhibits the 3rd PC (flavin) vs. the 2nd PC (NADH) of the untreated (solid circles) and treated (solid squares) cancerous breast cells. The most salient feature of Fig. 2(b) is that all data points for the untreated cells are located on the upper side over the data points for the treated cells, indicating that the relative contribution of tryptophan is higher in the untreated cancerous cells in comparison with the treated. Fig. 2(c) shows again that the relative fluorescence contribution of tryptophan is higher in the untreated cancerous cells in comparison with the treated. Fig. 2(d) shows that most data points for the untreated cells are located in the up-right side in comparison with the data points for the treated cells, indicating that the relative contents of NADH and flavin are higher in the untreated cancerous cells in comparison with the treated.

The following biomedical studies may help to understand these changes. Brown *et al* studied chemotherapy effects for breast cancer [3]. After chemotherapy, the decreased plasma amounts of tryptophan in plasma were observed [3] since increased tryptophan levels are somehow related to increased tumor cell proliferation [3]. NADH is one of the most important coenzyme for the production of Adenosine-Tri-Phosphate (ATP) [4]. The results of decrease of NADH in the RA-treated cancerous cells may reflect a reduction in the production of ATP in these treated cells. Since the decrease of tryptophan and NADH somehow reflect the less activity of cells [3, 4], it can be hypothesized that the RA-treatment results in cancerous cell death or reduction of the activity of cancer cells.

Emission spectra of nine pairs of the RA-treated and untreated breast cancer cell samples were measured with the excitation of 340 nm. The average fluorescence spectral profiles of the untreated (solid line) and treated (dash line) cells are displayed in Figs. 3(a), which shows that the emission profiles of the untreated and treated cells were mainly contributed from NADH corresponding to a peak at ~ 459nm, and flavin corresponding to a peak of ~ 530nm. The major difference of the profiles between the untreated and treated cells is that the shoulder peak at ~ 530 nm for the treated cells is little stronger than that for the untreated cells. Fig. 3 (b) displays the relative content of the flavin vs. NADH of the untreated (solid circle) and treated (solid square) cancerous breast cells analyzed using the NMF analysis. The obvious feature of Fig. 3(b) is that the relative contribution of NADH is higher in the untreated cancerous cells in comparison with the treated, which also reflects the decrease of the relative content of NADH in the treated cancerous breast cells in comparison with the untreated cells.

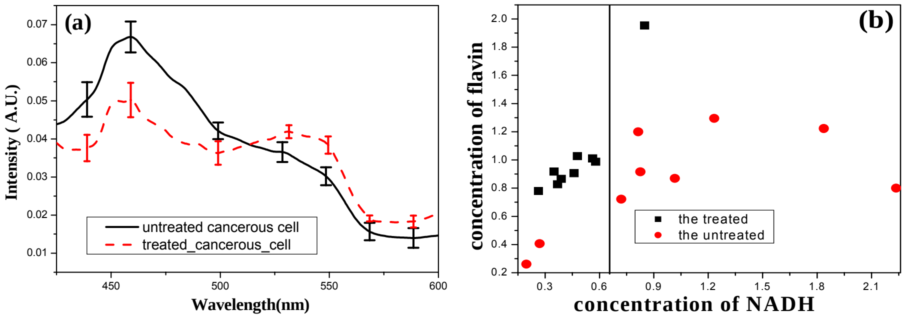

Fig. 3 (a) Average fluorescence spectra of the untreated (solid) and RA-treated (dash) cancerous breast cells obtained with the excitation wavelength of 340 nm.(b) Relative content of the NADH vs. flavin, obtained from the measured fluorescence spectroscopy of the breast cells with 340 nm excitation using the NMF analysis.

4. Conclusions

This study reports on detecting the chemotherapeutic effects on malignant breast cells by measuring the nature fluorescence spectra of cells and extracting the fluorescence spectral features of principal components using an NMF method. The presence and contents of the detectable fluorophores in breast malignant cells such as tryptophan, NADH and flavin were analyzed as the Principal Components for the NMF. We demonstrated that fluorescence intensities of tryptophan, NADH and flavin decreased in the RA-treated cells in comparison with those in the untreated cells. This work shows the change of relative contents of tryptophan, NADH and flavin studied using native fluorescence spectroscopy with the NMF analysis may present potential criteria for evaluation of chemotherapeutic effects on malignant breast cells.

5. Acknowledgement

This research is supported in part by the U. S. Army Medical Research and Material Command grants of W81XWH-08-1-0717 (CUNY RF 47170-00-01) and W81XWH-11-1-0335 (CUNY RF # 47204-00-01).

6. References

[1]R. R. Alfano, D. Tata, J. Cordero, P. Tomashefsky, F. Longo and M. Alfano, “Laser induced fluorescence spectroscopy from native cancerous and normal tissue”, *IEEE J. Quantum Electron*, 20, 1507-1511 (1984);

[2] Y. Pu, W.B. Wang, G. C. Tang and R. R. Alfano, “Changes of collagen and NADH in human cancerous and normal prostate tissues studied using fluorescence spectroscopy with selective excitation wavelength”, *J. Biomed. Opt.*, 15, 047008-1-5 (2010);

[3] Raymond R. Brown, Caroll M. Lee, Peter C. Kohler, Jaquelyn A. Hank, Barry E. Storer and Paul M. Sondel, “Altered tryptophan and neopterin metabolism in cancer patients treated with Recombinant Interleukin 2”, *Cancer Res.*, 49, 4941 - 4944 (1989).

[4] George D. Birkmayer, M.D., Ph.D. “The role of NADH in cancer therapy”, http://www.iatmo.org/abstract/birkmayer.pdf

Appendix6

A paper entitled “Picosecond polarization spectroscopy of fluorescein attached to different molecular volume polymer influenced by rotational motion” by Y. Pu, W. B. Wang, R. B. Dorshow, R. R. Alfano, published in *Organic Photonic Materials and Devices XIV*, edited by Christopher Tabor, François Kajzar, Toshikuni Kaino, Yasuhiro Koike, Proceedings of SPIE Vol. 8258-18 (SPIE, Bellingham, WA 2012).

Picosecond polarization spectroscopy of fluorescein attached to different molecular volume polymer influenced by rotational motion

Yang Pu[a], Wubao Wang[a], R. B. Dorshow[b], and R. R. Alfano[*a]
[a]Institute for Ultrafast Spectroscopy and Lasers, Department of Physics at The City College of the City University of New York, 160 Convent Avenue, New York, NY 10031
[b]Mallinckrodt Inc., 675 McDonnell Boulevard, P. O. Box 5840, St. Louis, MO 63134

ABSTRACT

Time-resolved fluorescence polarization spectroscopy of various molecular volume fluorescein dye-labeled polymers influenced by the molecular rotation motion was investigated by picosecond dynamics measurements. The time-resolved picosecond polarization spectroscopy was modeled using a system of first-order linear differential equations containing two main parameters: the decay rate of emission and the rate of one orthogonal emission component transferring to another. Both experimental observation and theoretical calculation indicate that the fluorescent molecular rotation is the cause of the depolarization. The dipole's rotational time was extracted and shows increasing with the molecular volume obeying the Einstein-Stokes relation.

Keywords: Time-resolved, picosecond spectroscopy, fluorescence depolarization, fluorescence anisotropy, molecular orientation and rotation, fluorescence lifetime, rotation time

1. INTRODUCTION

The depolarization of fluorescent molecule in solution was first realized by A. Jablonski [1]. This fluorescence depolarization technique can be used as a probe in chemistry and biology to determine the rotational rate of molecules by measuring the decay of the different polarized components [2, 3].

In this study, time-resolved fluorescence spectroscopy of fluorescein dye-labeled polymer chains with molecular volume ranged from ~410 angstrom^3 to ~5000 angstrom^3 at two polarization directions, parallel and perpendicular to that of the linearly polarized exciting light, were measured. It was observed in all measurements that the decay rate of the fluorescence component polarized parallel to the exciting beam is faster than that of the fluorescence component perpendicular to the excitation. A theoretical fluorescence depolarization model developed by G. Weber [4] was extended from micro-second to pico-second regimes to investigate and demonstrate the origin of the different decay rate of the two fluorescence components. This model describe the time-resolved fluorescence dynamics of fluorescein-polymer using a set of the linear differential equations containing two main parameters: the decay rate of emission and the rate of one orthogonal emission component transferring to another. Experimental tests of this theory were verified by measuring the time-resolved parallel and perpendicular components of the fluorescence using a streak camera system. Both experimental observation and theoretical calculation indicate that the fluorescent molecular rotation is the cause of the depolarization. The dipole's rotational time was extracted and shows increasing with the molecular volume obeying the Einstein-Stokes relation.

2. EXPERIMENTAL METHOD

2.1 Samples and setup

The dyes used in the time-resolved fluorescence polarization measurements are fluorescein and fluorescein conjugated dextrans with different molecular volume. Fluorescein is a synthetic organic compound available as a dark orange/red powder soluble in water and alcohol. It is widely used as a fluorescent tracer for many applications including biochemical research and health care applications. The chemical structure of Fluorescein is shown in Fig.1. The fluorescence of this molecule is very high, and excitation occurs at 494 nm and emission at 521 nm. In this study,

---

[*] alfano@sci.ccny.cuny.edu; phone: (212) 650-5531; fax: (212) 650-5530

Organic Photonic Materials and Devices XIV,
Edited by Christopher Tabor, François Kajzar, Toshikuni Kaino, Yasuhiro Koike,
Proc. of SPIE Vol. 8258, 825818 · © 2012 SPIE · CCC code: 0277-786X/12/$18 · doi: 10.1117/12.904692

fluoresceins were provided by Malinkrodt Inc (St. Louis, MO). The dimensions of fluorescein molecules were estimated as oblate with semi-axes of 7 angstrom and 2 angstrom for bond length and van der Waals radii [5], respectively. They were also conjugated to different dextrans with molecular size range from 1K angstrom to 700K angstrom by Malinkrodt Inc. The molecular weight and length per unit dextran is ~162 dalton and ~3 angstrom, respectively [5, 6]. The concentration of aqueous solution used for the fluorescence depolarization measurements was in the range of~50μM for fluorescein derivatives at room temperature.

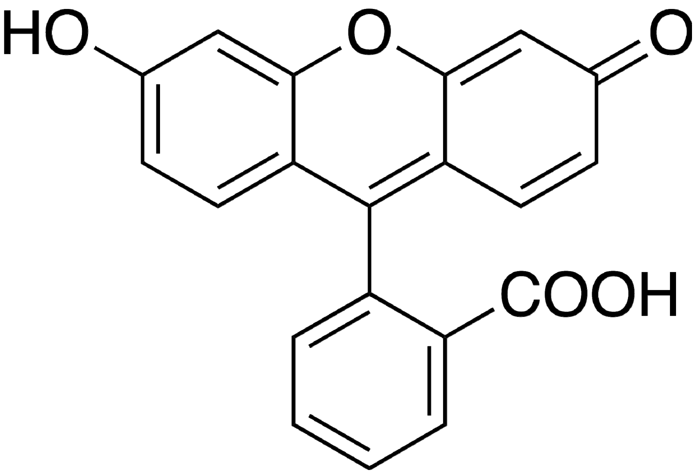

Fig. 1. Molecular structure of fluorescein. The dimensions of fluorescein molecules were estimated as oblate with semi-axes as 7 angstrom and 2 angstrom from bond length and van der Waals radii by its structure.

The experimental arrangement of time-resolved fluorescence polarization measurements has been given elsewhere [7]. Pulses of 100 fs at 400 nm obtained from the second harmonic of a Ti:Sapphire laser were used to pump samples. The temporal profiles of emission from the dye-polymer conjugates of $I_{||}(t)$ and $I_{\perp}(t)$ corresponding to the linearly polarized excitation light were recorded by a synchroscan streak camera. The fluorescence was collected by a large diameter lens (L_2) with a focal length of 5 cm and directed onto a synchroscan streak camera with temporal resolution of 10 ps. A long pass filter (LP) was used to block the illuminating light so that only the emission from the samples was detected. Polarizer P_1 was used to ensure the linear polarization of the input laser pulses and P_2 was used as an analyzer. The polarization of P_1 was rotated between 0^o and 90^o with respect to that of P_2 to record the intensity profiles of the parallel and perpendicular polarization components of the fluorescence. The temporal profiles recorded by a silicon intensified target (SIT) of the streak camera were analyzed to obtain temporal and polarization information.

2.2 Analysis model

The time-resolved fluorescence depolarization technique is widely used as a probe for re-orientation motion of molecules in solution since 1970's [2-4]. A theory developed by G. Weber *et al* described the equalization of the polarized intensity among the directions in the nanosecond scale [4] under specified conditions of temperature, viscosity and ordinary rate constants. We extend this model to the pico-second regimes to explore the effects of the molecular rotation to the fluorescence polarization spectroscopy.

For a single type of fluorephore, temporal profiles of the parallel and perpendicular components: $I_{\perp}(t)$ and $I_{||}(t)$ can be expressed as [8]:

$$I_{||}(t) = \frac{I_0}{3}\exp(-\frac{t}{\tau_f})\left(1+2r_0\exp(-\frac{t}{\tau_{rot}})\right) \qquad I_{\perp}(t) = \frac{I_0}{3}\exp(-\frac{t}{\tau_f})\left(1-r_0\exp(-\frac{t}{\tau_{rot}})\right) \qquad (1)$$

where I_0 is the initial emission intensity, τ_f is the fluorephore's lifetime, r_0 is anisotropy value at t=0 indicating the initial distribution of the excited polarized dipoles, and τ_{rot} is re-orientation time indicating the depolarization rate of the excited polarized molecules, which is determined by the microenvironments of the medium. In a simple case where the fluorephore molecule undergoes Brownian rotation as an Einstein sphere, the re-orientation time τ_{rot} can be expressed in terms of the medium viscosity (η), the absolute temperature of medium (T) and the molecular volume (V) by [2, 3]:

$$\tau_{rot} = \frac{\eta V}{kT} \qquad (2)$$

where k is the Boltzmann constant. It can be seen from Eequation (1) that measured temporal profiles of the parallel and perpendicular components of emission should include the information of the fluorephore's decay time (τ_f) and the re-orientation (rotational) time (τ_{rot}). To investigate the emission intensity and life time of fluorephore τ_f, the total temporal emission intensity can be calculated using an equation:

$$I_{total}(t) = I_{\|}(t) + 2I_{\perp}(t) = I_0 \exp(-\frac{t}{\tau_f}) \quad (3)$$

Equation (3) indicates that the life time τ_f of the excited fluorephores can be obtained from a temporal profile of the total emission ($I_{total}(t)$).

The time-resolved polarization anisotropy of emission is defined as [2, 3]:

$$r(t) = \frac{I_{\|}(t) - I_{\perp}(t)}{I_{\|}(t) + 2I_{\perp}(t)} = r_0 \exp(-\frac{t}{\tau_{rot}}) \quad (4)$$

where $I_{\|}(t)$ and $I_{\perp}(t)$ are measured intensities of the parallel and perpendicular polarization components of the time-resolved fluorescence, respectively. Equation (4) indicates that the re-orientation time (τ_{rot}) can be extracted from the time-resolved polarization anisotropy (r(t)) of the emission.

Using equations (3) and (4), we can separately study the life time and rotational time of the emission of the fluorephores from the time-resolved total emission and polarization anisotropy, respectively.

3. EXPERIMENTAL RESULTS AND DISCUSSION

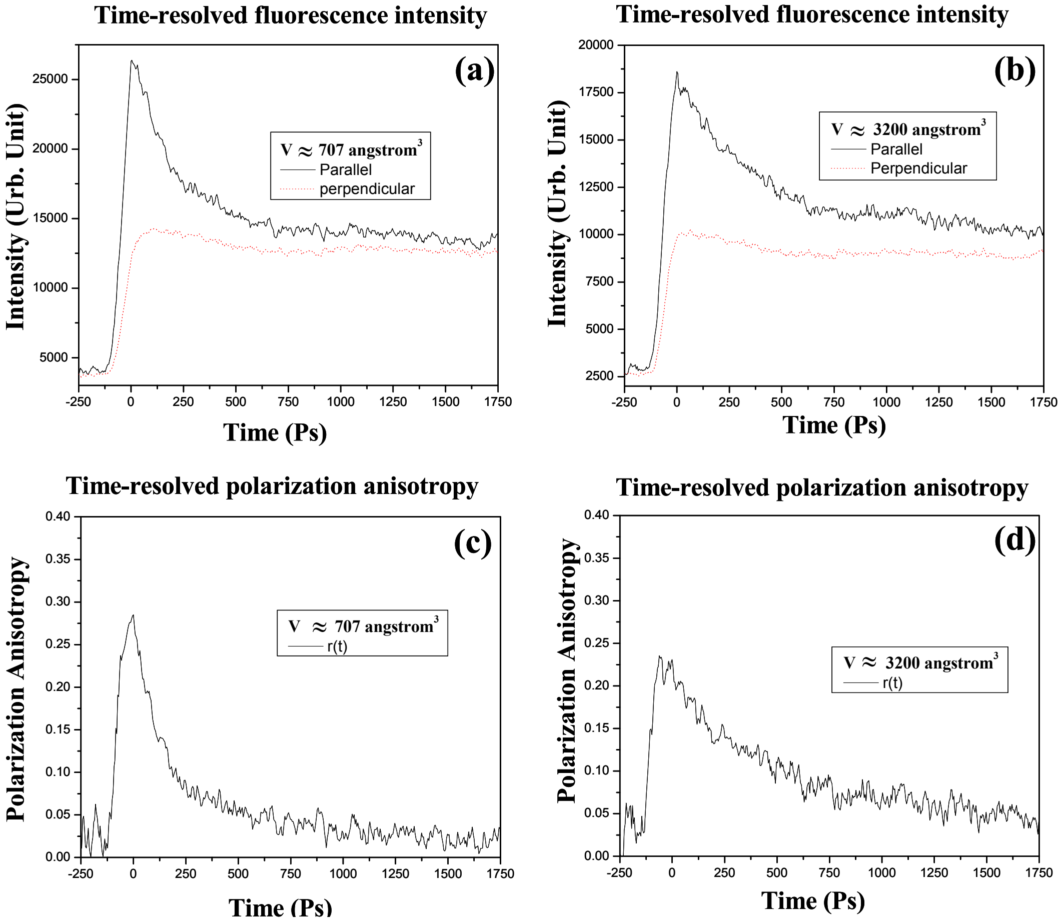

Fig. 2. The time dependent fluorescence intensity profiles of parallel (solid line) and perpendicular (dot line) components of emission from conjugated fluorescein-polymer of MV at (a) ~707 and (b) ~3,200 angstrom^3. The temporal profiles of the polarization anisotropy of conjugated fluorescein-polymer of MV at (c) ~707 and (d) ~3,200 angstrom^3.

The time-resolved fluorescence polarization profiles were recorded for fluorescein dye, and the fluorescein dye-labeled dextrans with different Molecular Volume (MV) from 400 to 5,000 angstrom^3. The dimensions of fluorescein were estimated as oblate with semi-axes of 7 and 2 angstrom [5]. As an example, Figs. 2 (a) and 2 (b) show the measured temporal profiles of parallel and perpendicular components of the emission from the conjugated dye-polymer with different MV of ~707 and ~3,200 angstrom^3, respectively. The solid line profiles show the parallel component, and the dot lines show the perpendicular one. Fig. 2 (a) and 2 (b) show that $I_{||}(t)$ is greater than $I_{\perp}(t)$ at all of the decay times indicating that this dye-polymer keeps property of the polarization preservation. The time-resolved polarization anisotropy r(t) can be obtained by substituting the data of $I_{||}(t)$ and $I_{\perp}(t)$ shown in Figs. 2 (a) and 2 (b) into the time dependent equation (4). The calculated results are shown in Figs. 2 (c) and 2 (d) displaying the temporal profiles of polarization anisotropy for Fluorescein-polymer with different MV of ~707 and ~3,200 angstrom^3, respectively.

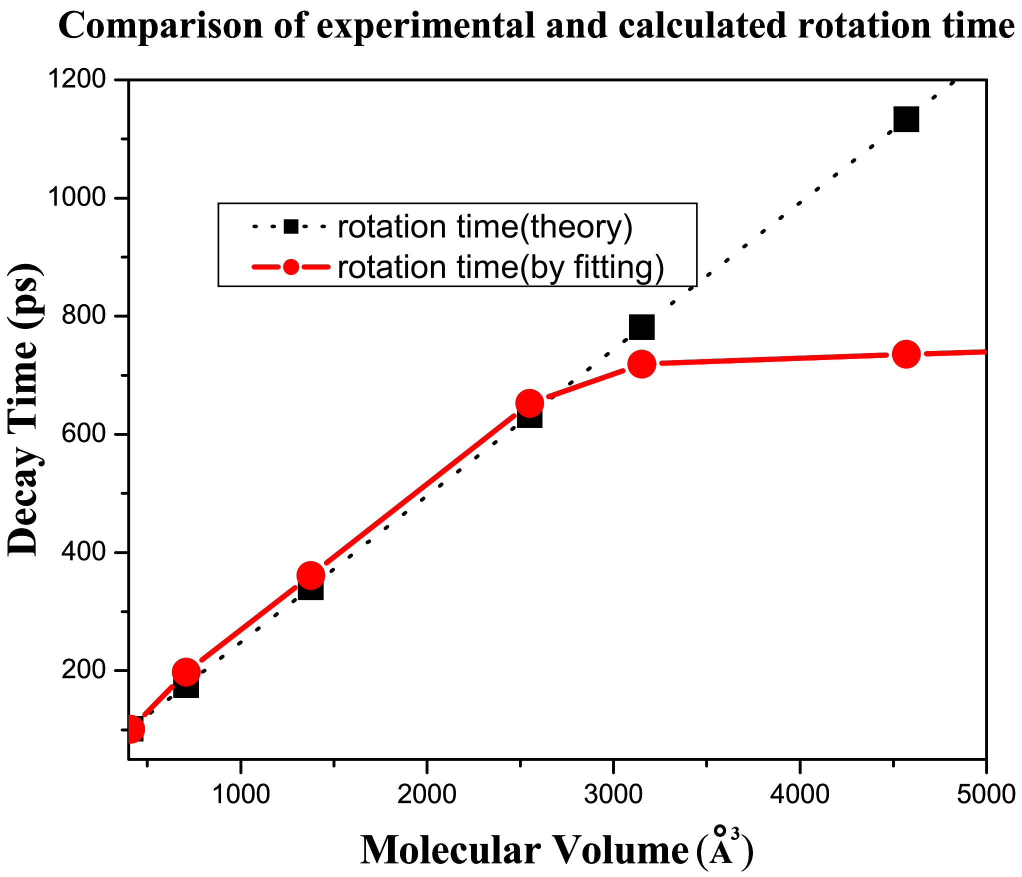

Fig. 3. (a) The rotation time obtained by theoretical calculation (dot line) and by fitting the experimental data (solid line) of the fluorescein dye-polymer conjugate as a function of molecular volume.

The salient features are: (1) the temporal polarization anisotropy shown in Fig. 2 (c) exhibits a faster decay than the profile shown in Fig. 2 (d), indicating that smaller molecular volume gives faster Brownian rotation as described by Equation (2); (2) The initial anisotropy r_0 shown in Fig. 2 (c) is greater than that shown in Fig. 2 (d). In order to study rotation time changes with the molecule volume, the experiments were performed for a set of Fluorescein-polymer conjugates with attached chain having the volume varying from ~400 to 5,000 angstrom^3. The rotation times can be obtained by fitting the experimental data of r(t) with Equation (4) and the results are displayed as solid lines in Fig. 3. The theoretical values of the rotation times with different attached polymer length were calculated using Equation (2) and compared with the experimental values, shown as the dot-line profile in Fig. 3. Since the fluorescein dye appears as approximated oblate symmetric rotors [5], the volume were calculated to be ~ 410 angstrom^3 as oblate ellipsoid with semi-axes 7 and 2 angstrom while no polymer attached.

The salient features of Fig. 3 are: (1) the rotation times raise with the volume of the attached polymer chain, which are in good agreement with experimental values and exhibit a linear dependence on the volume of molecules as predicted by Equation (2) when the volume of conjugated Fluorescein-polymers is less than 3,200 angstrom^3. This can be understood because the Brownian rotational motion for larger volume conjugated dye-polymer is slower given rise to a longer rotation time; (2) The rotation time becomes flat when the volume of the dye-polymer increases beyond ~3,000 angstrom^3. This indicates that for large size molecules, where the volume exceeds a critical value, the rotation time changes very slow with volume of the fluorescent molecules. The incorrect prediction of Equation (2) may be because the Fluorescein-polymer can no longer be estimated as a simple dimension as a sphere or an oblate since it is difficult to control the polymer chain extending direction. The irregular shapes of molecules result in the different rotation rate of D_{ij} [2-4], and therefore the depolarization will not show simple exponential decay as described by time-resolved polarization anisotropy r(t) in form of Equation (3). In addition, the rapid internal motions originated by flexible structure of the conjugated fluorescein-polymers cause the "extra" depolarization other than rotation of the molecule [2].

4. CONCLUSION

We have experimentally and theoretically investigated that when an isotropic fluorescent molecular system is excited with a linearly polarized light beam, the intensity decay of their fluorescence component polarized parallel to the exciting beam is faster than that of the fluorescence component perpendicular to the exciting beam. This phenomenon can be explained with the time-resolve fluorescence depolarization caused by the Brownian rotation of the dipoles. For a simple and stable molecule, the effect of Brownian rotation is the main cause of the depolarization. Time-resolved depolarization measurements were used to obtain the rotation time and initial polarization anisotropy. We have also shown that over a the range of the molecular volume of dye-polymer when $r(t)$ exhibit the single exponential decay, the accuracy of the theoretical calculation is quite comparable with value obtained by fitting the experimental value.

5. ACKNOWLEDGEMENT

This research is supported by U. S. Army Medical Research and Material Command (USAMRMC) under the grant number of DAMD17-01-1-0084 (CUNY RF 47462-00-01), W81XWH-08-1-0717(CUNY RF # 47170-00-01), and W81XWH-11-1-0335 (CUNY RF # 47204-00-01).

REFERENCES

[1] A. Jablonski, "Uber die Abklingungsvorgange polarisierter Photolumineszenz", *Zeitschrift fur Naturforschung*, 16a, 1-4 (1961).

[2] G. R. Fleming, J. M. Morris and G. W. Robinson, "Direct observation of rotational diffusion by pico-second spectroscopy", *Chem. Phys.*, 17, 91-100 (1976).

[3] G. Porter, P. J. Sadkowski and C. J. Tredwell, "Pico-second rotational diffusion in kinetic and steady state fluorescence spectroscopy", *Chem. Phys. Lett.*, 49, 416-420 (1977).

[4] [4] R. D. Spencer and G. Weber, "Influence of Brownian rotations and energy transfer upon the measurements of fluorescence lifetime". *J. Chem. Phys*. 52, 1654-1663 (1970).

[5] Scout Hell, "Size Matters: How big are molecules", http://www.bbc.co.uk/dna/h2g2/A791246

[6] W. B. Wang, J. H. Ali, R. B. Dorshow, M. A. McLoughlin and R. R. Alfano, "Time-resolved fluorescence polarization dynamics and imaging of fluorescein dye attached to different molecular weight chains", SPIE-Proceedings of Biomedical Imaging: Reporters, Dyes, and Instrumentation, 3600, 227-229 (1999).

[7] Y. Pu, W. B. Wang, B. B. Das, S. Achilefu, and R. R. Alfano, "Time-resolved fluorescence polarization dynamics and optical Imaging of Cytate: a prostate cancer receptor-targeted contrast agent", *Appl. Opt.*, 47, 2281-2289 (2008).

[8] Y. Pu, W. B. Wang, and R. R. Alfano, "Time-resolved fluorescence spectroscopy of contrast agent, ICG, influenced by rotational motion," in *Frontiers in Optics (FiO)/Laser Science (LS)* (Optical Society of America, Washington, DC, 2010), JTuA19.

Attachment 1

Certificate of *RARC Orientation* training in MSKCC

WEILL CORNELL MEDICAL COLLEGE · CORNELL UNIVERSITY

Certificate of Completion

Yang Pu

Successfully completed

RARC New Investigator Orientation

June2, 2011

Education & Quality Assurance Specialist
Memorial Sloan Kettering Cancer Center

RARC
RESEARCH ANIMAL RESOURCE CENTER

Attachment 2

Certificate of *RARC Basic Mouse* training in MSKCC

WEILL CORNELL MEDICAL COLLEGE · CORNELL UNIVERSITY

Certificate of Completion

Yang Pu

Successfully completed

Basic Mouse Hands-On

July 7, 2011

Education & Quality Assurance Specialist
Memorial Sloan Kettering Cancer Center

RESEARCH ANIMAL RESOURCE CENTER

Attachment 3

Certificate of *RARC Rodent Survival Surgery* training in MSKCC

Certificate of Completion

Yang Pu

Successfully completed
Rodent Surgery Lecture
July 18, 2011

Education & Quality Assurance Specialist
Memorial Sloan Kettering Cancer Center

RESEARCH ANIMAL RESOURCE CENTER